Doctorate Dissertation

博士論文

Dark matter search with high-energy gamma-ray observations

(高エネルギーガンマ線による暗黒物質探査)

A Dissertation Submitted for Degree of Doctor of Philosophy
Decermber 2018

平成30年12月博士(理学)申請

Department of Physics, Graduate School of Science,
The University of Tokyo

東京大学大学院理学系研究科物理学専攻

Nagisa Hiroshima

廣島　渚

Dark matter search with high-energy gamma-ray observations

Nagisa Hiroshima

Department of Physics, Faculty of Science,
University of Tokyo, Bunkyo-ku, Tokyo 113-0033, Japan

Abstract

We can access dark matter of mass $m_{\rm DM} \gtrsim O(1)$ TeV by measuring high-energy emissions from the Universe. For the dark matter of $m_{\rm DM} \sim O(1) - O(100)$ GeV, the annihilation cross-sections into the standard model particles are tightly constrained by observing γ-ray signals in dwarf spheroidal galaxies with *Fermi* satellite. In this thesis, we consider the search for the heavier dark matter of $m_{\rm DM} \gtrsim O(1)$ TeV in dwarf spheroidal galaxies with Cherenkov Telescope Array (CTA), which is a next-generation very-high-energy γ-ray project. With the improved angular resolution of the CTA facilities, dark matter density profiles of dwarf spheroidal galaxies are well-resolved. We investigate how the spatial extension of the dwarf spheroidal galaxies affect the sensitivity. For this purpose, we simulate a 500-hour observation of Draco dSph with CTA and perform likelihood analyses assuming 16 different profiles. We show that the spatial extension of the dwarf spheroidal galaxy affects the feasibility of detecting dark matter in a different way from that of the J-factor. The accessible region of the annihilation cross-section can differ by a factor of ~ 10 if we assume different profiles with the same J-factor. CTA is capable of testing some well-motivated models expecting resonant annihilations of dark matter particles even with the most conservative assumptions. We also examine the uncertainty coming from the subhalo boost. If dwarf spheroidal galaxies contain subhalos inside them, the dark matter annihilation signals are boosted. We develop a new analytical formalism to calculate the contributions from the subhalos down to the minimum halo-mass scales and at arbitrary redshifts. Our analytical results for the tidal mass-loss rate, the subhalo mass function, and the subhalo mass fraction are consistent with those obtained in N-body simulations of corresponding mass ranges and redshifts. Based on the analytically calculated subhalo evolutions, we show that the subhalo boost is negligible for halos of the dwarf spheroidal galaxy scale. This indicates that no subhalo contributions as well as astrophysical γ-ray emissions are expected in dwarf spheroidal galaxies. Hence they are well-motivated targets for CTA to obtain robust constraints on the dark matter properties.

Contents

List of Figures

List of Tables

Chapter 1

Introduction

Dark matter (DM) is a massive and invisible component in the Universe [1–3]. There is strong evidence for the existence of dark matter, such as the matter distribution in the Universe from the gravitational lensing [4], the rotation curves of galaxies [5,6], the mass of the galaxy clusters [7,8], the bullet cluster observations [9,10] and so on. All of them indicate that the visible galaxies are embedded in huge invisible *halos*. A further strong motivation for dark matter is coming from the theory of the cosmological structure formation [11–13]. In the standard cosmology, the seed of the current structure is the density fluctuation generated during the inflation. The Universe after the inflation is filled with radiations and starts to expand. The evolution of the seed fluctuation is determined by the competition between the gravitational force and the radiation pressure. It is suppressed at the beginning due to the high radiation pressure. In the later epoch after the matter-radiation equality at redshift $z \sim 3000$, the density fluctuation can start to grow. The evolution of the baryon fluctuation starts when it decouples from the radiation. However, if the baryon is the unique matter component in the Universe, initial fluctuations corresponding to the scale of the galaxy are erased out before the baryon-photon decoupling due to the collisional damping [14]. We can solve this problem by introducing another matter component which starts to evolve just after the matter-radiation equality. Such a matter component different from the baryon is called *dark matter*. The total amount of the dark matter in the current Universe is determined from cosmological observations in various scales [12,13]. It occupies about a quarter of the total energy density of the Universe [13,15–17]. This is about 5 times larger than that of the baryon.

Cosmological observations which determine the total energy density of dark matter give some indications about the properties of dark matter. Dark matter should be *cold*, i.e., the velocity dispersion is low enough not to erase the seed fluctuation of the baryonic structures. They should be stable. They should be almost neutral to be decoupled from photons. They should feel the gravity. Astrophysical observations also give hints about the structure of

dark matter in the current Universe. Dark matter forms gravitationally bounded objects called *halos*. The mass of the largest halo reaches $M \sim 10^{16} M_{\odot}$. Halo structures are highly hierarchical. Other properties are not well-understood yet. We do not know whether dark matter is a new particle or not. It is also still uncertain that whether they can feel forces other than the gravity. Varieties of models are proposed from the theoretical side. One possibility is that dark matter is a new particle: weakly interacting massive particles (e.g. [18, 19]), gravitinos (e.g. [20, 21]), strongly interacting massive particles (e.g. [22, 23]), axions or axion-like particles (e.g. [24–26]), and sterile neutrinos (e.g. [27–30]) are parts of examples. Non-particle solutions such as primordial black holes (e.g. [31–35]) are also considered. In this thesis, we focus on the search of the dark matter categorized as weakly interacting massive particles (WIMPs) in the Universe.

WIMP is one of the best-studied candidates for dark matter which realizes the observed dark matter density [13, 16] with the so-called freeze-out mechanism. An example of the particle model for the WIMP is the neutralino which appears in the supersymmetric extensions of the standard model (e.g. [36, 37]). The freeze-out of the WIMP dark matter is described with the annihilation cross-section into the standard model particles and does not depend on the details of the particle WIMP models. In the early Universe, the interaction between the standard model particles and WIMPs is frequent enough to sustain a thermal equilibrium. As the Universe expands, the particles become non-relativistic and their number density decreases. The interaction rate of the annihilation process of the WIMP into the standard model particles is written as the number density times the cross-section $\langle \sigma v \rangle$. The annihilation stops when the interaction rate drops below to the expansion rate of the Universe. The total number of the WIMP is fixed at this stage. If the annihilation cross-section is $\langle \sigma v \rangle \sim 3 \times 10^{-26}$ cm^3/s [38], the relic abundance is achieved by the freeze-out when the temperature of the Universe is around $O(1)$ GeV - $O(1)$ TeV. This value of the annihilation cross-section is referred to as the canonical cross-section. The annihilation cross-section is also written with the mass of the WIMP $m_{\rm DM}$ and the coupling constant g as $\langle \sigma v \rangle = g^4 / m_{\rm DM}^2$. When the coupling is the weak-scale of $g \sim O(0.1)$ and the mass is $m_{\rm DM} \sim O(1)$ GeV - $O(1)$ TeV, the canonical cross-section is realized. The correspondence with the "weak scale" of $\sim O$ (1) TeV [20, 39] indicates that the interaction is mediated by particles of this energy scale.

If dark matter is a new particle which has small but finite interaction with the standard model particles, like the case of the WIMP, it becomes detectable. Three kinds of strategies are pursued: productions of the dark matter particles from the standard model particles with colliders (e.g. [40, 41]), measurements of the scattering between dark matter particles and nuclei (or electrons) called direct detection experiments (e.g. [42–44]), and the search for the standard model particles produced by dark matter interactions in the Universe called indirect detection experiments. There has been no confirmed detection of the dark matter yet. For WIMP of $m_{\rm DM} \sim O(1 - 10)$ GeV, its annihilation cross-section into the standard

model particles is already constrained to be lower than the canonical value [45]. Lighter dark matter candidates of $m_{\rm DM} \lesssim O(100)$ MeV are constrained from the structure formation because they keep relatively larger velocities at a later epoch and erase the fluctuations through the free-streaming (e.g [46–49]). The heavier ones of $m_{\rm DM} \gtrsim O(1)$ TeV have been less investigated. Various projects are on-going and planned to search dark matter in this less proved regions.

Indirect detection experiments have advantages in dark matter searches at higher energy scales of $E \gtrsim O(1)$ TeV, which are beyond the scope of laboratory experiments. A plethora of projects searching for dark matter signals in the Universe with charged cosmic-rays (e.g. [50–53]), neutrinos (e.g. [54, 55]) and γ-rays are under operations. The limitation of this method comes from the difficulties in astrophysical modelings. There are many competing sources for dark matter signals in the Universe. The first task in the indirect search of dark matter is to remove the astrophysical emissions. The spectrum and the emission morphology are used to identify sources. After removing the astrophysical emissions, one must consider the environment of the annihilation site. The amount of the dark matter responsible for the observed standard model particles must be known or modeled. Furthermore, the propagation process between the annihilation site and the observer should be considered in some cases. For example, charged cosmic-rays do not propagate straightly from the source because they are scattered by magnetic fields. We could not trace back the charged cosmic-rays of $E \sim O(1)$ GeV - $O(1)$ TeV, which are produced in our Galaxy, to the source. Also, the interaction with the background photons (e.g. the cosmic microwave background radiations or stellar emissions at infrared wavelength) could modify the spectra of γ-rays and cosmic rays from those at the source.

We can search dark matter in an efficient way with γ-ray observations [3]. γ-rays take straight paths from the annihilation site to the Earth. Propagation of the γ-rays within our Galaxy does not affect their spectrum. Hence we are free from the uncertainties in the modeling of the propagation. Furthermore, it is sensitive to any of the final states in dark matter annihilations. Final states are determined by the models. However, γ-ray emissions are always expected in the successive process whenever the standard model particles are produced. The γ-ray flux from the dark matter annihilation is written as

$$\phi_\gamma = \frac{1}{4\pi} \frac{\langle \sigma v \rangle}{2m_{\rm DM}^2} \int_{E_{\rm th}}^{m_{\rm DM}} dE \frac{dN_\gamma}{dE} \cdot J \tag{1.0.1}$$

where

$$J = \int d\Omega \frac{dJ}{d\Omega} = \int d\Omega \int ds\, \rho_{\rm DM}^2. \tag{1.0.2}$$

$E_{\rm th}$ in Eq. (1.0.1) is the threshold energy which depends on the observing facilities. In Eq. (1.0.1), all the quantities except for J are determined by the particle physics. The part shown as J in Eq. (1.0.2) is referred to as the "(astrophysical) J-factor". Since the J-factor

is the line-of-sight integral over the squared dark matter density $\rho^2_{\rm DM}$, information about the dark matter distribution in our regions of interests should be known. Because of its $\rho^2_{\rm DM}$ dependence, the J-factor and the expected flux from the dark matter annihilation are very sensitive to its density distribution. A higher flux of dark matter annihilation signal is expected in a denser region of dark matter.

Dwarf spheroidal galaxies (dSphs) are good targets to search for dark matter. They are satellite galaxies of the Milky Way of which masses are dominated by dark matter. The J-factor of dSphs reaches $O(10^{17} - 10^{19})$ GeV^{2}cm^{-5}. They do not contain astrophysical γ-ray sources such as pulsars. For the dark matter of $m_{\rm DM} \sim O$(1-10) GeV, observations of dSphs with *Fermi* satellite have constrained the annihilation cross-section down to the canonical value. To search dark matter in higher mass regions of $m_{\rm DM} \sim O(1)$ TeV, we need imaging atmospheric Cherenkov telescopes such as H.E.S.S., MAGIC, or VERITAS. They detect γ-ray signals by imaging the Cherenkov shower produced by very-high-energy photons entering the Earth's atmosphere. In the very near future, Cherenkov Telescope Array (CTA) starts its operation. The designed sensitivity of CTA facilities at $E_\gamma \sim O(0.1 - 100)$ TeV is about 10 times better than those of the current ones. The best sensitivity is achieved at $E_\gamma \sim O(1)$TeV. The angular resolution is also improved to ~ 0.04 degrees in this energy range. It should be the best facility to search the dark matter of $m_{\rm DM} \gtrsim O(1)$ TeV. In this thesis, we consider dark matter search in dSphs with CTA.

The typical angular size of the dSphs is $\Delta\theta \lesssim O(1)$ degrees. This is much larger than the angular resolution of the CTA, i.e., CTA can resolve them as extended sources. The dark matter density distribution at the center of the dSphs should be discriminated. However, dark matter density profiles of dSphs are under discussion. In this thesis, we quantify how the density profile of target dSphs affect the feasibility of detecting dark matter with CTA. For this purpose, we sample the profiles of Draco dSph from the literature and perform likelihood analyses of a simulated data for a 500-hour observation with CTA. We show for the first time that the detectability of dark matter with CTA depends on the density profile of the targets in addition to the well-known dependence on the J-factor. We also show that parts of the well-motivated WIMP models can be tested by observing dSphs with CTA in spite of the uncertainties in density profiles.

We also examine the possibilities of additional uncertainties coming from the subhalos in dSphs. The existence of small-scale halos of $M \sim O(10^{-12}$-$10^{-3})M_\odot$ are naturally expected in WIMP dark matter scenarios [56–59]. The minimum mass of the dark matter halo depends on the elastic scattering process of dark matter during the era between chemical and kinetic decoupling [60]. If subhalos lie on our lines-of-site, they should boost the dark matter annihilation signals. Previous estimates about the subhalo boost contain huge uncertainties because one has to extrapolate the numerical expectations at a certain mass and redshift range to much wider (e.g. [61, 62]). We solve this problem by developing a new analytical formalism to follow the evolutions of subhalos in arbitrary mass and redshift ranges. Based

on the analytical calculations, we show that the subhalo boost is negligible for halos of the dSph scale. This indicates that dSphs are well-motivated targets to search for dark matter with CTA of which uncertainties such as contributions from astrophysical sources or subhalos are small compared to those of other proposed targets.

The structure of this thesis is as follows. Chapter 2 summarizes parts of the dark matter candidates and the constraints obtained by indirect detection experiments. The advantage of the γ-ray search is explained in Chapter 3. In Chapter 4, we quantify the dependence of the detectability of WIMP on the density profile of dSph considering the search with CTA. In Chapter 5, we explain our analytical formalism to calculate the subhalo boost. We show in this chapter that the subhalo boost is negligible for dSphs. The conclusion of the thesis is in Chapter 6. In the appendices, we include the brief cosmological history (Appendix B), the current constraints on WIMP by collider and direct detection experiments (Appendix C), the principle to detect high-energy γ-rays (Appendix D), and the up-to-date list of dSphs (Appendix E).

Chapter 2

Properties of dark matter

2.1 general properties

By definition, dark matter (DM) is a non-relativistic, non-baryonic component which occupies a quarter of the total energy of the universe. The dark matter density today, referred to as the *relic density* is

$$\Omega_{\rm DM}h^2 = 0.1206 \pm 0.0021(68\%\ \text{C. L.}) \tag{2.1.1}$$

where $h = H_0/100\text{km/s} = 0.6688 \pm 0.092$. A flat Λ-CDM cosmology is assumed [17]. $\Omega_{\rm DM} = \rho_{\rm DM}/\rho_0$ is a cosmological parameter with the critical density $\rho_0 = 1.054\times10^{-5}h^2\ \text{GeV}c^{-2}\ \text{cm}^{-3}$. The baseline properties of dark matter are determined from the cosmological structure formation. Because of the one-to-one correspondence between the temperature fluctuation and the density fluctuation, the cosmic microwave background (CMB) anisotropy is an important observable to determine the relic density [13,63–65]. Measurements of the baryon acoustic oscillations are another quantity to be used [66–68]. Other cosmological observations put additional constraints on the properties of dark matter. For example, the consistency between the observations of the light element abundance and the theoretical predictions from the Big Bang nucleosynthesis should be satisfied [69,70]. As general conditions, dark matter should be:

- stable
- different from baryons
- non-relativistic
- almost invisible
- almost neutral

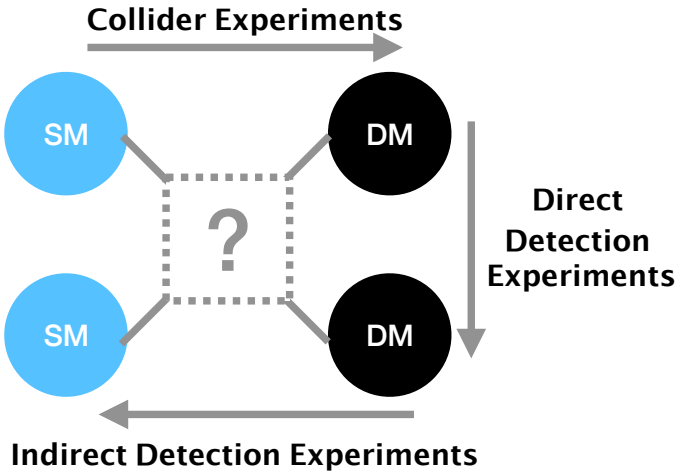

Figure 2.1: Schematic picture of three strategies for the search of dark matter. We focus on the *indirect detection experiments* in this thesis.

The large scale structure of the Universe also requires that dark matter should not be *hot*, i.e., its kinetic energy should be small compared to the mass. If dark matter is hot, the baryon density fluctuations relevant for the structure larger than the Lyman-α cloud are erased. The energy density of dark matter is proportional to the inverse of the volume, which is a *matter*-like behavior same as that of baryons. Then one possibility is that dark matter is a new particle. Non-particle solutions such as primordial black holes are also possible. In association with other problems in the standard model, varieties of models are proposed.

If there exist any kinds of interactions between dark matter and the standard model particles which are different from the gravity, dark matter becomes detectable. Three kinds of strategies are considered:

1. Collider experiments
2. Direct detection experiments
3. Indirect detection experiments

Each of the dark matter candidates is tested combining the results from these experiments. Fig. 2.1 schematically explains the strategies. In collider experiments, dark matter is searched in the products of the standard model particle collisions. The missing energy, the displacement of the interaction vertex, new resonances are examples of the observables. This strategy is superior to the others in terms of the systematic uncertainties. All of the inputs are known

and experiments can be repeated in principle. However, the accessible parameter regions are limited by the maximum accelerator energy. Also, the analyses are highly model-dependent. The second strategy is the direct detection experiment which measures the scattering between dark matter particles and nuclei (or electrons) at underground detectors. The explorable parameter regions extend as time goes once the detector is set. The spatial and velocity distribution of dark matter around the Earth should be derived from astrophysical observations. The rejection of the background particles like muons or neutrinos is also important. The last one, the indirect detection experiment, is a strategy to search dark matter through the measurement of the standard model particles in the Universe produced by dark matter. There are no limitations in the accessible energy scale. Techniques to detect high-energy emissions up to $E \sim 10^{20}$ eV are already developed (e.g. [71, 72]). γ-rays, cosmic rays, neutrinos, and gravitational waves can be messengers. Models are tested with multimessenger observations. The ability of this method is limited by systematic uncertainties. There are numbers of astrophysical sources and processes that could contaminate dark matter signals. In this thesis, we focus on the indirect search with γ-ray observations.

2.2 Candidates

Varieties of dark matter candidates are proposed in the literature. In this thesis, we focus on dark matter categorized as weakly interacting massive particles (WIMPs). In this section, we review some of the candidates and constraints from indirect detection experiments.

2.2.1 Weakly Interacting Massive Particles (WIMPs)

properties

Weakly interacting massive particles (WIMPs) are one of the best studied dark matter candidates. The *neutralinos* in the supersymmetric (SUSY) theory are famous examples. They are new particles in the SUSY extensions of the standard model (e.g. [36]). By introducing the symmetry between bosons and fermions, some problems in the standard model such as the *hierarchy problem* can be solved. The *gauge unification* could also be achieved by introducing the SUSY. In the minimal SUSY extension of the standard model, the followings are introduced:

- fermionic partners of each gauge field in the standard model (*gauginos*)
- scalar partners of the fermions (*squarks* and *sleptons*)
- one additional Higgs field, and the superpartners of each Higgs field (two *Higgsinos*)

The gauginos are *gluino*, *wino*, and *bino*. They are partners of the gluon, $W^{\pm}$ boson, and the B boson in the standard model sector. B boson is a mixed state of the photon and the Z boson. A new symmetry referred to as the R-parity is conserved in the minimal SUSY extension of the standard model. R-parity is a symmetry between the standard model particles (R=+1) and their superpartners (R=-1). From the conservation of the R-parity, one superparticle should decay into an odd number of superparticles and the standard model particles. The lightest one, which is denoted as LSP, should be stable and become a dark matter candidate. The species of the LSP is determined by fixing the way of the SUSY breaking. When the LSP is the neutral wino, higgsino, or bino (referred to as the *neutralino*), they are strong dark matter candidates [73]. If their thermally-averaged annihilation cross-section into the standard model particles is

$$\langle \sigma v \rangle \simeq 3 \times 10^{-26}\ \mathrm{cm}^3/s, \tag{2.2.1}$$

they meet the relic abundance in Eq. (2.1.1) by the freeze-out mechanism. The freeze-out occurs when the annihilation rate becomes smaller than the expansion rate of the Universe. A detailed discussion about the derivation of the canonical cross-section in Eq. (2.2.1) is summarized in Appendix B.2.

Note that the velocity dependence of the annihilation process is neglected in Eq. (2.2.1). In some scenarios, the annihilation cross-section σv depends on the collision velocity v. When the annihilation occurs in a resonant process, we can expect a higher value for averaged annihilation cross-section $\langle \sigma v \rangle$ for the thermal relic dark matter [74]. The enhancement of the WIMP annihilation cross-section also occurs in other mechanisms such as the higher-order correction [75].

cosntraints

Since WIMP is one of the strongest candidates for dark matter, its properties are rigorously studied in numbers of experiments. We review the constraints obtained with indirect detection experiments in the next section (Sec. 3.2). Those obtained with collider and direct detection experiments are in Appendix C. For comparison between the different strategies, we show Fig. 2.2 taken from [76]. In Fig. 2.2, the annihilation cross-section is assumed to be independent of the collision velocity of the particles. The strongest constraints are obtained by γ-ray observations. For WIMP of $m_{\mathrm{DM}} \lesssim 100\mathrm{GeV}$ annihilating into $\bar{b}b$ pairs, the upper limits on the annihilation cross-section obtained by collider and γ-ray experiments already reach the canonical value in [38].

Cosmic microwave background observations and the Big-Bang nucleosynthesis also put independent constraints [77]. The constraints are weaker than that of the γ-rays but applicable for more general case that the annihilation cross-section depends on the collision velocity.

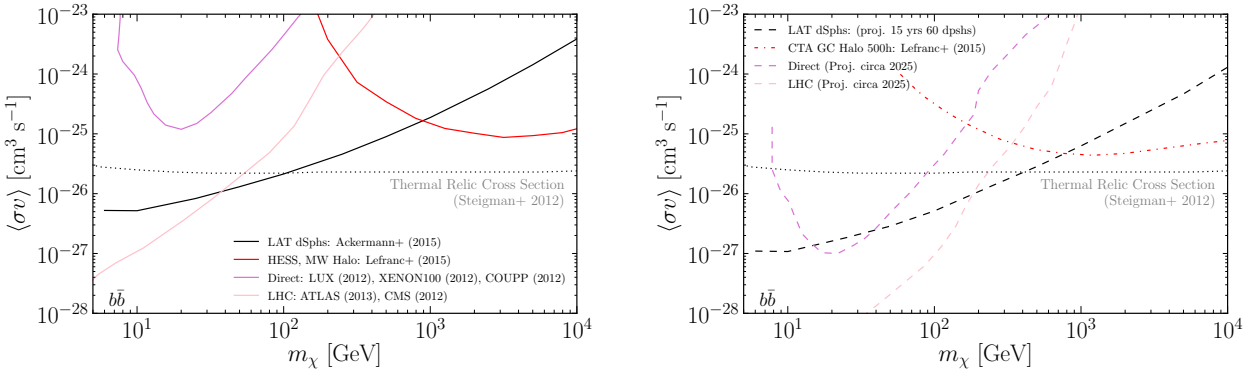

Figure 2.2: The obtained (*left*) and expected (*right*) upper limits on the annihilation cross-section of WIMP in [76].

2.2.2 Strongly Interacting Massive Particles (SIMPs)

properties

Strongly interacting dark matter (SIMP) is a recently proposed model that introduces a relatively strong self-interaction between dark matter particles [23]. Compared to the WIMP which achieves the relic abundance by the freeze-out of the 2-to-2 annihilation process, SIMP in [23] achieves by the 3-to-2 process. The freeze-out condition for the 3-to-2 process is

$$n_{\rm DM}^2 \left\langle \sigma_{3\to 2} v^2 \right\rangle = 0.44 (g_{*,\text{freeze-out}})^{1/2} \frac{T_{\text{freeze-out}}^2}{M_{\rm pl}} \tag{2.2.2}$$

where T and v is the temperature and the velocity of the particle, respectively. Compared to the 2-to-2 freeze-out case, an additional v appears due to the 3-body interaction. They are referred to as the SIMP because

$$\left\langle \sigma v^2 \right\rangle_{3\to 2} = \frac{\alpha_{\rm eff}^3}{m_{\rm DM}^5} \tag{2.2.3}$$

with $\alpha_{\rm eff} = 1$ at $m_{\rm DM} \sim 40$MeV is required to achieve the relic abundance. The coupling $\alpha_{\rm eff} = 1$ is strong compared to the weakly interacting case of $\alpha_{\rm eff} \sim O(0.01)$, i.e., the dark matter particles are *strongly-interacting*.

Note that this is a special class of the model in a much wider category of the self-interacting dark matter. By introducing self-interactions of dark matter particles, some of the problems with cold dark matter scenarios such as WIMPs can be solved. There are claims about the cold dark matter scenarios are in tension with the observed structures of the Universe (e.g. [78]). For example, the density profiles of the cold dark matter halo in cosmological simulations

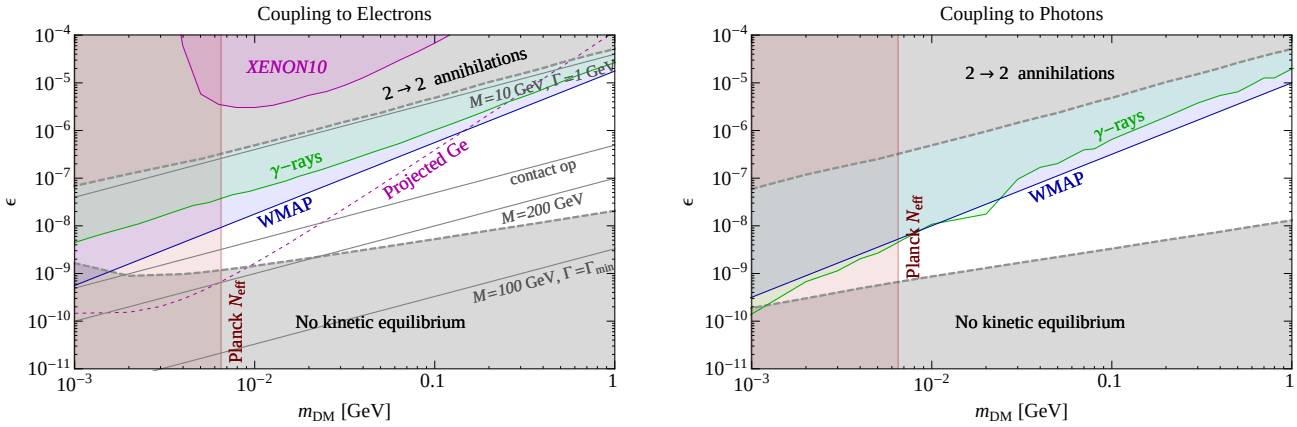

Figure 2.3: An example of the constraints on the interaction strength between self-interacting dark matter and the standard model particles [23]. The model needs to be specified for these kinds of discussions.

are cuspy at the center while the observations of small-scale galaxies (e.g. dwarf spheroidal galaxies) indicate the existence of the density core. This is called as the *core-cusp problem* [79, 80]. Self-interaction of dark matter can erase the cusp at the center of the galaxy then produce the core. Another problem is a so-called *too-big-to-fail* problem. In the simulations of the Milky-Way sized galaxies, we can expect more massive subhalos than the observed satellite galaxies in our Galaxy [81]. When the density core is formed by the dark matter self-interaction, this problem can also be solved [82, 83]. Many self-interacting dark matter models are proposed.

constraints

Observation of the galaxy clusters put constraints on the strength of the self-interaction strength of dark matter particles [84–87]. The offset of the mass center of the stellar components and the dark matter halo works as the indicator. Gravitational lensings are also used. In addition, the distribution of the satellite galaxy in numerical simulations is also sensitive to the strength of the self-interaction. Most of the constraints are derived in model dependent ways. We show an example case for strongly-interacting dark matter in [23]. Fig. 2.3 shows the bounds on the interaction cross-section between SIMP and the standard model particles assuming the coupling to the electron (*left*) or photon (*right*). In this case, CMB and γ-ray observations constrain the interaction strength between SIMP and the standard model particles.

2.2.3 sterile neutrinos

properties

Sterile neutrino is a right-handed neutrino which mixes with the standard model neutrinos through the oscillation. The idea is originally proposed to explain the neutrino oscillation. Another motivation is to explain the baryon asymmetry of the Universe (e.g. [88, 89]). The sterile neutrino can be either of the warm, hot, or cold dark matter depending on the production mechanism [27]. Two production mechanisms are widely discussed: non-resonant oscillations with the standard model neutrinos in the early Universe [27, 90] or resonant oscillations [28, 91]. Other mechanisms are also possible. Constraints on the sterile neutrino dark matter are dependent on the production mechanism. After the production, they behave as dark matter since they are neutral and massive. The typical mass of the sterile neutrino is $m_N \sim O(0.1)$ - $O(100)$ keV. We use the character N to denote the sterile neutrino in this section.

constraints

The most important process of the interaction between sterile neutrinos and the standard model particles in the indirect search is the radiative decay [92–94]. Sterile neutrinos produce photons in two patterns of decay modes:

$$N \to 3\,\nu \tag{2.2.4}$$

and

$$N \to \nu\gamma \tag{2.2.5}$$

denoting a standard model neutrino with ν. The typical lifetime for the 3-body decay mode is [95]

$$\Gamma(N \to 3\nu) \sim \frac{1}{1.5 \times 10^{14}\mathrm{s}} \left(\frac{m_N}{10\mathrm{keV}}\right)^5 \sum_\alpha |\theta_\alpha|^2 \tag{2.2.6}$$

where the $\sum_\alpha |\theta_\alpha|^2$ is the total mixing angle. They should be stable in the cosmic time of $\sim 4.4 \times 10^{17}$s. Then the upper limits on the mixing angle is obtained as

$$\sum_\alpha |\theta_\alpha|^2 < 3.3 \times 10^{-4} \left(\frac{m_N}{10\mathrm{keV}}\right)^{-5}. \tag{2.2.7}$$

The lifetime of the other radiative decay mode is

$$\Gamma(N \to \nu\gamma) \sim \frac{1}{1.8 \times 10^{26}\mathrm{s}} \left(\frac{m_N}{10\mathrm{keV}}.\right)^5 \sum_\alpha |\theta_\alpha|^2. \tag{2.2.8}$$

A photon of which energy $E_\gamma \sim 0.5 m_N$ is produced in this process. The branching ratio between the two decay modes is

$$\frac{\Gamma(N \to \nu\gamma)}{\Gamma(N \to 3\nu)} = \frac{1}{128}. \tag{2.2.9}$$

Assuming that the sterile neutrino is the dominant component of dark matter, we can probe the model parameter space of the sterile neutrino. Since the sterile neutrino mass is at around $O(1)$ keV, X-ray observations are important. There are claims for the detection of the X-ray line from the decay of sterile neutrinos [96, 97]. However, these observations are inconsistent with other X-ray observations [98, 99] which only give upper limits on the X-ray flux. The possibilities to explain the X-ray observation with emission lines of ions are also discussed [100, 101].

2.2.4 axions and axion-like particles (ALPs)

properties

The original motivation for axion is different from that of dark matter. It is proposed as the solution to the strong CP problem [104–107]. Axion appears when a global chiral $U(1)_{\rm PQ}$ symmetry is spontaneously broken. The favored mass ranges to solve the strong CP problem is around $m_{\rm a} \sim O(10^{-6})$ eV. We use m_a to denote the axion mass. Recently, axions are extended to a more general class of models referred to as the *axion-like particles (ALPs)*. ALPs are oscillating light-scalar fields which behave like dark matter as we explain in below. The mass range of the consideration extends down to $O(10^{-22})$ eV (e.g. [108]).

The reason that axion behave as dark matter is as follows. Since axion is a scalar field, its potential is written as

$$V(\varphi) = \frac{1}{2} m_a^2 \varphi^2 \tag{2.2.10}$$

where φ is the axion field. In the expanding Universe with a Robertson-Walker metric, the equation of motion is

$$\ddot{\varphi} + 3H(t)\dot{\varphi} + m_a^2(t)\varphi = 0. \tag{2.2.11}$$

In the early Universe when the Hubble parameter is large enough, $H \gg m_a$, the potential term is negligible. Then the energy of the field decreases as $\varphi \propto a^{-3}$. At a later epoch of $m_a \gg H(t)$, φ has an oscillating solution. Using WKB approximation, the solution is

$$\varphi(t) \simeq \varphi_1 \left(\frac{a(t_1)}{a(t)}\right)^{3/2} \cos\left[\int_0^t m_a(t)dt + \text{const.}\right] \tag{2.2.12}$$

The energy density of the axion decreases as $\propto a^{-3}$ by taking average over the oscillation period of Eq. (2.2.12). This satisfies the property required to be dark matter.

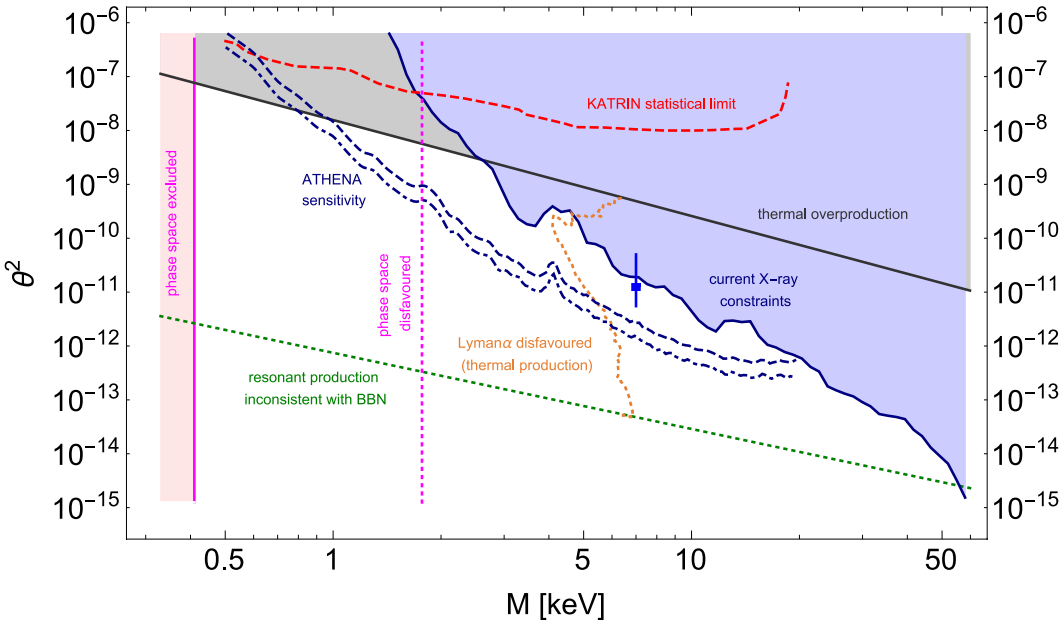

Figure 2.4: Constraints on the sterile neutrino dark matter in [95]. Constraints shown with solid lines are derived in model independent ways. The region above the black solid line is excluded not to overproduce the dark matter. The blue shaded region corresponds to the constraint from X-ray observations. See Eqs.(2.2.6) and (2.2.8) for the relation between the X-ray flux and the mixing parameter θ^2. The magenta line at the left edge is derived from Pauli's exclusion principle. Resonantly-produced sterile neutrinos lighter than ∼5keV (dashed orange line) are disfavored from the structure formation [102]. The same region is also excluded by the phase-space density of the dwarf spheroidal galaxy [103]. The dotted magenta line at $m_N \sim 2\,\mathrm{keV}$ is obtained by including a thermal distribution for non-resonantly produced sterile neutrinos.

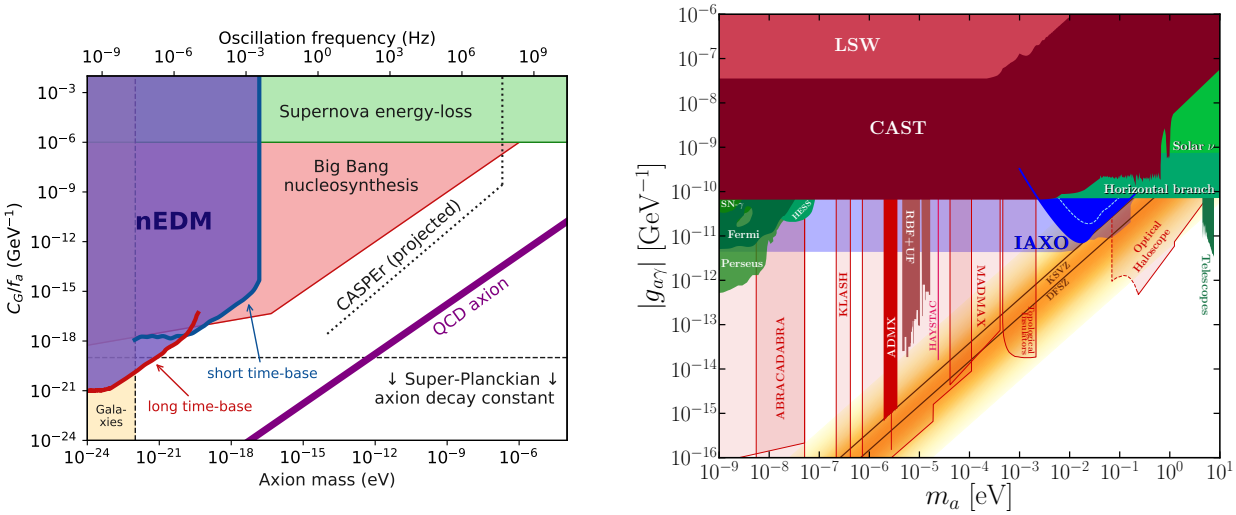

Figure 2.5: Constraints on the axion-like particles plotted in the plain of the ALP mass m_a and the coupling strength $g_{a\gamma}$. The *left* panel is for ALP of 10^{-24}eV $< m_a < 10^{-6}$ eV [112]. The *right* panel is for ALP of 10^{-9}eV $< m_a < 10^{1}$ eV [113]. The vertical axis is different between the panels since two works [112, 113] adopt different conventions. The purple line in the *left*panel (the orange region in the *right* panel) corresponds to the QCD axion.

constraints

Axion and axion-like particles are searched through their interaction with photons. The relevant term in the $U(1)_{\rm PQ}$ symmetric Lagrangian is

$$L_{a\gamma\gamma} = \frac{g_{a\gamma\gamma}}{4} F_{\mu\nu}\tilde{F}^{\mu\nu} a = -g_{a\gamma\gamma} \boldsymbol{E}\cdot\boldsymbol{B} a. \tag{2.2.13}$$

Astrophysical observations [109] and laboratory experiments give complemental constraints on axions and ALPs. Some of the constraints are applicable to the case that axions or ALPs are different from dark matter. Fig. 2.5 shows the excluded region of ALPs. For constraint on the ALP dark matter, see [110, 111] for examples.

2.2.5 primordial black holes (PBHs)

properties

Primordial black hole (PBH) is a non-particle candidate for dark matter. They are formed from the curvature perturbations in the early Universe [31–34, 114, 115]. Their formation

occurs at or before the radiation dominated era, which is well-before the matter-radiation equality. They work as pre-existing gravitational potentials at the baryon-photon decoupling. Then the baryon fluctuations can evolve to form the current structure of the Universe. PBH mass is determined by the time of its formation as

$$m_{\rm PBH} \sim M_{\rm pl}^2 t_{\rm form} \sim \frac{M_{\rm pl}}{T_{\rm form}^2} \sim 10^{15} \left(\frac{T_{\rm form}}{3\times 10^8 {\rm GeV}}\right)^{-2} \ {\rm g}. \tag{2.2.14}$$

$M_{\rm pl}$ is the Planck mass defined as $M_{\rm pl} = \sqrt{\hbar c/G}$. The energy density of the PBH is parametrized as

$$\beta(M_{\rm PBH}) = \frac{\rho_{\rm PHB}(t_{\rm form})}{\rho_{\rm form}} = \frac{m_{\rm PBH}(t_{\rm form})}{\rho(t_{\rm form})} \sim 7.98\times 10^{-29} \gamma^{-1/2} \left(\frac{g_{*,\rm form}}{106.75}\right)^{1/4} \left(\frac{m_{\rm PBH}}{M_\odot}\right)^{3/2} \left(\frac{n_{\rm PBH}(t_0)}{\rm Gpc^{-3}}\right) \tag{2.2.15}$$

or

$$\beta'(m_{\rm PBH}) = \gamma^{1/2} \left(\frac{g_{*,\rm form}}{106.75}\right)^{-1/4} \beta(m_{\rm PBH}) \tag{2.2.16}$$

assuming a monochromatic mass spectrum. t_0 corresponds to the current universe ($z = 0$) and $g_{*,\rm form}$ is the effective degree of freedom at the formation epoch. The numerical factor $\gamma \sim 3^{-1/5}$ is determined depending on the details of the gravitational collapse. The parameter β corresponds to the cosmological parameter for PBH, $\Omega_{\rm PBH}$, as

$$\Omega_{\rm PBH} = \frac{m_{\rm PBH} n_{\rm PBH}}{\rho_{\rm c,0}} \sim \left(\frac{\beta(m_{\rm PBH})}{1.15\times 10^{-8}}\right) \left(\frac{h}{0.72}\right)^{-2} \gamma^{1/2} \left(\frac{g_{*,\rm form}}{106.75}\right)^{-1/4} \left(\frac{m_{\rm PBH}}{M_\odot}\right)^{-1/2}. \tag{2.2.17}$$

Quantum particle creation from the PBH through the Hawking radiation leads to its evaporation [116, 117]. They evaporate in the lifetime of

$$\tau_{\rm PBH} \sim \frac{m_{\rm PBH}^3}{M_{\rm pl}^4} \sim 4\times 10^{17} \left(\frac{m_{\rm PBH}}{10^{15}{\rm g}}\right)^3 \ {\rm s}. \tag{2.2.18}$$

Heavier PBHs live longer because the evaporation timescale for the Hawking radiation become longer. At the evaporation, their particle creation is regarded as the black-body radiation of temperature

$$T_{\rm PBH} \sim \frac{M_{\rm pl}^2}{m_{\rm PBH}} \sim 0.1 \left(\frac{m_{\rm PBH}}{10^{15}{\rm g}}.\right)^{-1} \ {\rm MeV}. \tag{2.2.19}$$

One can constrain the PBH fraction in the total dark matter content, $f = \Omega_{\rm PBH}/\Omega_{\rm DM}$ by observing photons produced in this mechanism.

constraints

PBH fraction in the dark matter is constrained in two ways: (i) through gravitational interactions and (ii) through Hawking radiations. Combining various observations, PBH fraction $f = 1$ could not be achieved if the mass function of the PBH is monochromatic.

- constraints from gravitational interactions
  Firstly, they are constrained from the measurements of the gravitational lensing. PBH of $m_{\rm DM} = 10^{17} - 10^{20}$ g is constrained by the femtolensing of the γ-ray burst [118]. PBH of $m_{\rm PBH} = 10^{22} - 10^{24}$ g is constrained by the microlensing of quasars [119, 120] and $m_{\rm PBH} = 10^{16} - 10^{35}$ g is by the stellar microlensing in Large Magellanic Cloud and Small Magellanic Cloud [121, 122], respectively. Quasar microlensing is also applicable for this mass range [123]. Strong lensing of the radio source gives limits in $m_{\rm PBH} = 10^{39} - 10^{41}$ g [124]. Secondly, dynamical heating and the survival of the binary system also give limits. PBHs of mass $m_{\rm PBH} = 10^{18} - 10^{24}$ g are captured by the neutron star, then take them up. So the observed abundance of the neutron star gives upper limits on the fraction f [125]. Heating of the white dwarf by transiting also constrains the PBH of $m_{\rm PBH} = 10^{20} - 10^{23}$ g since they trigger the supernova explosions [126]. Observations of the stellar cluster in the Eridanus II dwarf spheroidal galaxy constrains the PBH of $m_{\rm PHB} = 10^{34} - 10^{37}$ g, because heating by the PBH should dissociate the cluster [127]. The existence of wide binaries also assures the absence of the PBH of $m_{\rm PBH} = 10^{36} - 10^{41}$ g [128]. Further discussions about various dynamical constraints are given in [129]. The same constraints also hold for the so-called MAssive Compact Halo Object (MACHO).

- constraints from Hawking radiation
  Hawking radiation of the PBH also put upper limits on their abundance. The observation of the isotropic γ-ray background gives constraints in $m_{\rm PBH} = 10^{13} - 10^{17}$ g [33, 115]. These include extragalactic and galactic contributions. Smaller PBHs are also constrained since emitted particles affect the big bang nucleosynthesis. PBH evaporating before the big bang nucleosynthesis change the abundance of the light elements by injecting hadrons [130], while those after the nucleosynthesis also modify the abundance by photo-dissociations. Spectrum distortion of the CMB caused by the injection of photons put constraints on the PBH of $m_{\rm PBH} = 10^{9} - 10^{13}$ g [131].

- other constraints
  When baryons accrete onto PBHs, the energy of the accreting matter is converted to the radiation. Accreting PBHs should be detected as X-ray sources then the number count of the galactic X-ray sources constrains the PBH of $m_{\rm PBH} = 10^{33} - 10^{40}$ g [132]. Also in the early Universe, photons from accreting PBHs heat up the background plasma. This leads to the distortion of the CMB spectrum. Note that the photons

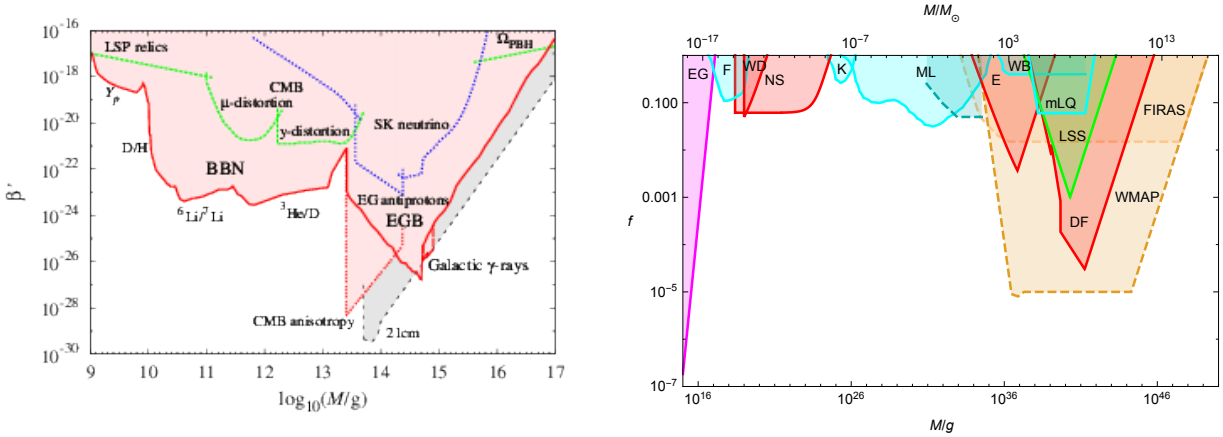

Figure 2.6: Constraints on the PBH fraction in total dark matter density. *Left* panel is for PBHs lighter than $m_{\rm PBH} = 10^{17}$ g [115] and *right* panel is for those heavier than 10^{17} g (*right*) [32]. In the *left* panel, the PBH fraction to the dark matter is represented with the parameter β' in Eq. (2.2.16). Shaded regions are excluded.

are injected in a different way from that of the Hawking radiation. The constraints using CMB distortions are dependent on the models of the accretion. However, they are independent of the above-mentioned constraints and cover a wide mass range of $m_{\rm PBH} = 10^{32}$ - 10^{45} g [25, 133–136].

Combining various observations, PBH fraction in the dark matter is already limited to be smaller than $f = 1$ for wide ranges of PBH masses. Constraints in Fig. 2.6 are obtained assuming monochromatic mass functions. Note that some of the constraints are still uncertain (e.g. [125, 137] and the discussion in [138]). The possibilities to explain all the dark matter by PBH with extended mass function are also considered [34].

Chapter 3

Dark matter search with γ-ray observations

Indirect detection experiments are a strategy to search standard model particles produced by the annihilation or decay of dark matter in the Universe. This is a unique strategy to access the heavier dark matter of $m_{\rm DM} > O(1)$ TeV, which is beyond the scope of the laboratory experiments. γ-ray, cosmic ray, and neutrino can work as probes. The combination of the multiparticle data is also an important topic in this field. The limitations of the indirect search come from the difficulties in astrophysical modelings. Careful treatments about the discrimination of the dark matter signal from astrophysical emissions, the spatial distribution of dark matter, and the modelings of the propagation after the production are required. In this section, we review the indirect search of dark matter focusing on γ-ray observations. Advantages and up-to-date constraints from observations of other species, neutrinos and cosmic rays, are also included in Sec. 3.3.

3.1 γ-rays from dark matter annihilations

In this thesis, we consider to search annihilation signal of WIMP dark matter. Any of the standard model particles can be expected in the final state depending on the details of the model. For example, expressing a dark matter particle with χ,

$$\chi + \chi \rightarrow \gamma\,\gamma \tag{3.1.1}$$
$$\chi + \chi \rightarrow q\,\bar{q} \rightarrow \pi^0 + \cdots \rightarrow 2\gamma + \ldots \tag{3.1.2}$$
$$\chi + \chi \rightarrow l^+\,l^- \rightarrow \gamma l^+ l^- \ldots \tag{3.1.3}$$
$$\chi + \chi \rightarrow W^+\,W^- \rightarrow e^+\,\nu_e, \bar{\nu_e} + \ldots,\ q\bar{q} + \ldots \rightarrow \ldots \tag{3.1.4}$$

and combinations of these annihilation channels are also possible. As a general expression, the flux of the species α of the standard model particle produced in the annihilation of dark matter is

$$\phi_\alpha = \frac{1}{2}\frac{1}{4\pi}\frac{\langle\sigma v\rangle}{m_{\rm DM}^2}\int^{m_{\rm DM}}\sum_i b_i\frac{dN_{\alpha,i}}{dE_\alpha}dE_\alpha\cdot\int_{\Delta\Omega}d\Omega\int_{l.o.s}ds\rho_{\rm DM}^2 \tag{3.1.5}$$

where b_i is the branching ratio and $dN_{\alpha,i}/dE_\alpha$ is the spectrum of the final state particle α produced in the annihilation channel i. The latter parts in the Eq. (3.1.5) is referred to as the (astrophysical) J-factor:

$$J = \int_{\Delta\Omega}d\Omega\int_{l.o.s}ds\rho_{\rm DM}^2. \tag{3.1.6}$$

We can expect a higher flux from dark matter annihilations if we look at a denser region. As expressed in the Eqs. (3.1.1)- (3.1.4), γ-ray emissions are always expected in the successive processes. Therefore it is reasonable and effective to search dark matter with γ-rays. In the following part of this thesis, we fix α to the γ-ray.

There are additional advantages to search dark matter through γ-ray observations. Firstly, γ-rays (and also neutrinos) arrive at the Earth straightly from the source. It is different from the case of charged cosmic-rays. Cosmic rays are reflected by the magnetic field permeating their propagation paths. Then, it is almost impossible to trace back them to the source. Also, parts of the produced cosmic-ray could not reach to the Earth because of the dissipation and diffusion. The transport of the cosmic ray is an actively-debated topic in astrophysics. Secondly, for γ-ray of $E_\gamma \lesssim O(1)$ TeV coming from the $z \lesssim 0.1$ sphere, the attenuations are negligible. High-energy γ-ray photons produce electron-positron pairs when they hit low-energy photons in the background. The interaction with the CMB photons occurs elsewhere. Electrons and positrons produced in this process emit lower energy γ-rays through inverse Compton emissions. The process is repeated until the energy of the γ-ray photon decreases down to the rest-mass energy of the electron. The cross-section of the γ-ray photon and a background photon relevant for the pair creation is [139].

$$\sigma_{\gamma\gamma}(E_\gamma,\epsilon,\theta) = \frac{3}{16}\sigma_T\left(1-\beta^2\right)\left[2\beta(\beta^2-2)+(3-\beta^4)\ln\left(\frac{1+\beta}{1-\beta}\right)\right] \tag{3.1.7}$$

where E_γ and ϵ is the γ-ray and background photon energy, respectively. σ_T is the Thomson scattering cross-section. The definition of the parameter β depends on the angle of the collision θ as

$$\beta = \sqrt{\frac{1-4m_e^2c^4}{2E_\gamma(1-\cos\theta)}}. \tag{3.1.8}$$

The absorption of the γ-ray photon in this process is most significant with

$$\epsilon_{\rm max} \sim \frac{(2m_e c^2)^2}{E_\gamma} \sim 0.5 \left(\frac{E_\gamma}{\rm TeV} \right)^{-1} \ {\rm eV}. \tag{3.1.9}$$

Introducing the number density of the target low-energy photon $n_\gamma(z)$ at redshift z, the optical depth for γ-ray photon emitted at redshift z is

$$\tau(E_\gamma, z) = c \int^z dz \frac{dt}{dz} \int_0^2 dx \frac{x}{2} \int_{2m_e^2 c^4/(E_\gamma \epsilon x(1+z))}^\infty d\epsilon \frac{dn_\gamma(\epsilon, z)}{d\epsilon} \sigma_{\gamma\gamma}(\beta). \tag{3.1.10}$$

The redshift and energy dependence of the optical depth $\tau(E_\gamma, z)$ is shown in Fig. 7 of [139]. For γ-ray photons of $E_\gamma \sim 1$ TeV, the optical depth $\tau \sim 1$ corresponds to the redshift $z \sim 0.1$. Hence the absorption of high-energy γ-rays during their propagation is negligible for observations of high-energy γ-rays from galactic sources such as the Galactic Center or dwarf spheroidal galaxies.

3.2 Strategies for dark matter search with γ-ray observations

Considering the γ-ray flux from dark matter annihilations in Eq. (3.1.5) and Eq. (3.1.6), the simplest strategy is to observe a high J-factor region in the Universe. However, such a region usually contains astrophysical γ-ray emitters. Astrophysical γ-ray signals are always higher than those expected for dark matter annihilations. We need elaborated strategies. For example, one could success by masking the known γ-ray sources in high J-factor regions. The search in different regions of no astrophysical sources and relatively high J-factors is another strategy. Several targets have been considered as targets for γ-ray search of dark matter:

1. isotropic γ-ray background
2. galaxy clusters
3. the Galactic Center
4. Milky Way halo
5. satellite galaxies
   Large Magellanic Cloud, dwarf spheroidal galaxies, dwarf irregular galaxies

Their properties and the current status of the search are explained in below.

3.2.1 isotropic γ-ray background

Full-sky observations of the *Fermi* satellite reveal the existence of the isotropic γ-ray background (IGRB) emissions. The flux of the IGRB at $O(10)$ GeV is about six orders-of-magnitude smaller than that of the CMB [140]. The flux of the IGRB is derived after subtracting the galactic diffuse emission in the foreground. The γ-rays from the inverse Compton emission of electrons or positrons and those from the decay of the π^0 produced by protons are responsible for the foreground. Three models in [141] are conventionally used to determine the diffuse foreground. The galactic models of [141] differs in the modeling of the spatial distribution of the cosmic-ray source. The extragalactic components after the foreground subtractions are believed to be dominated by the γ-ray from active galactic nuclei at large distances [142–144]. Each active galactic nucleus could not be resolved as a point source. The remaining γ-ray flux, i.e., the flux after subtracting the galactic emissions and the extragalactic astrophysical emissions, are allowed for dark matter annihilations or decays. Statistical methods are adopted to search dark matter signals in IGRB. Analyses of the anisotropy [145, 146] as well as the isotropic total intensity [147–149] give constraints on the dark matter annihilation cross-section. By adopting the cross-correlations with other observables like galaxy catalogues (e.g. [150–154]), much wider regions of the dark matter parameter space can be probed. Dark matter search in the galactic isotropic γ-ray emission is also proposed [155]. IGRB observations are also powerful in constraining the decaying dark matter [142, 156]. Current constraints from IGRB observations are shown in Fig. 3.1.

3.2.2 galaxy clusters

The cluster of galaxies is the most massive structure in the Universe of which mass reaches to $M \sim O(10^{16})M_\odot$. They are the largest gravitationally bounded objects and contain a lot of dark matter substructures. As is discussed in [62], the J-factor of the galaxy cluster varies between $J \sim O(10^{15}) - O(10^{19})$ GeV^{2}cm^{-5} depending on the models of the substructure. Numerical simulations are powerful tools to study hierarchical structures of galaxy clusters. We need to cover wide ranges of mass and redshift to evaluate the contributions from substructures. The huge uncertainty in the J-factor is introduced when one extrapolates the estimates obtained by numerical simulations in limited mass and redshift ranges to much wider regions.

They are massive and diffuse. This is one reason that the constraints on the dark matter annihilation cross-section obtained by observations of galaxy clusters are milder than those of dwarf spheroidal galaxies [157]. It might not be the best targets for searching dark matter annihilation signals [61, 62]. However, their diffuse property does not affect the search of decaying dark matter signals. In this case, they can be good targets [158, 159] once the substructure contributions are precisely understood. Current constraints are shown in Fig. 3.2.

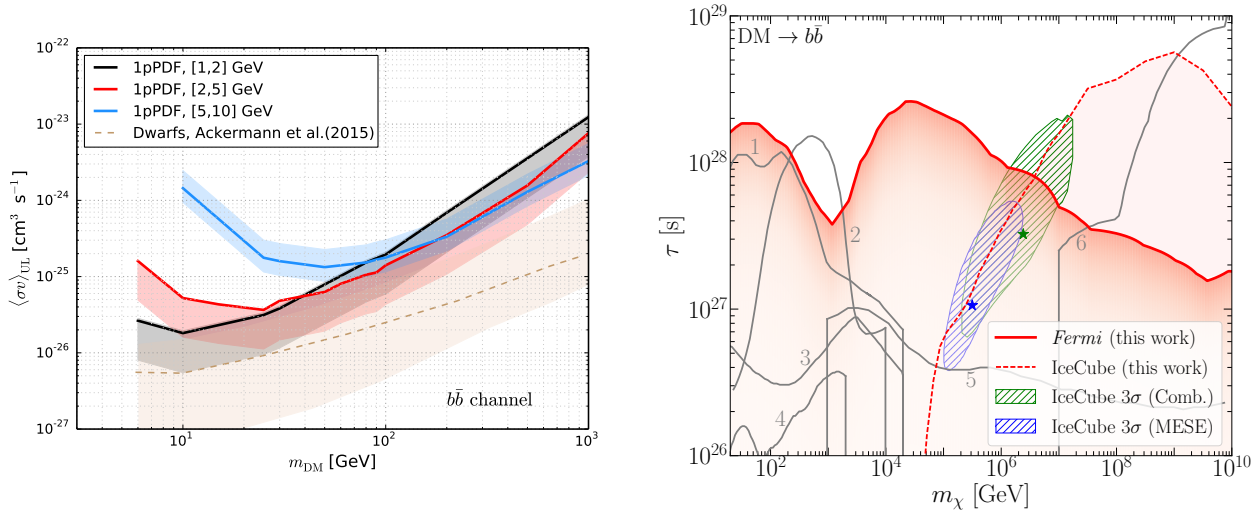

Figure 3.1: Constraints on the WIMP annihilation cross-section [149] (*left*) and decay lifetime [156] (*right*) obtained by isotropic γ-ray background observations. The annihilation or decay to a $\bar{b}b$ final state is assumed. In the *left* panel, the one-point pixel count statistics method is applied to obtain the constraint. Different lines correspond to the different datasets they have used. Shaded regions below each line are the uncertainty coming from the galactic diffuse models [141]. The dashed line corresponds to the upper limit by the observations of dwarf spheroidal galaxies. In the *right* panel, constraints by γ-ray observations are shown with the red solid line. Lower limits of the lifetime obtained by neutrino observations are also shown with the dotted line. Blue and green hashed regions correspond to the best-fit parameters to explain the excess in the IceCube data with decaying dark matter.

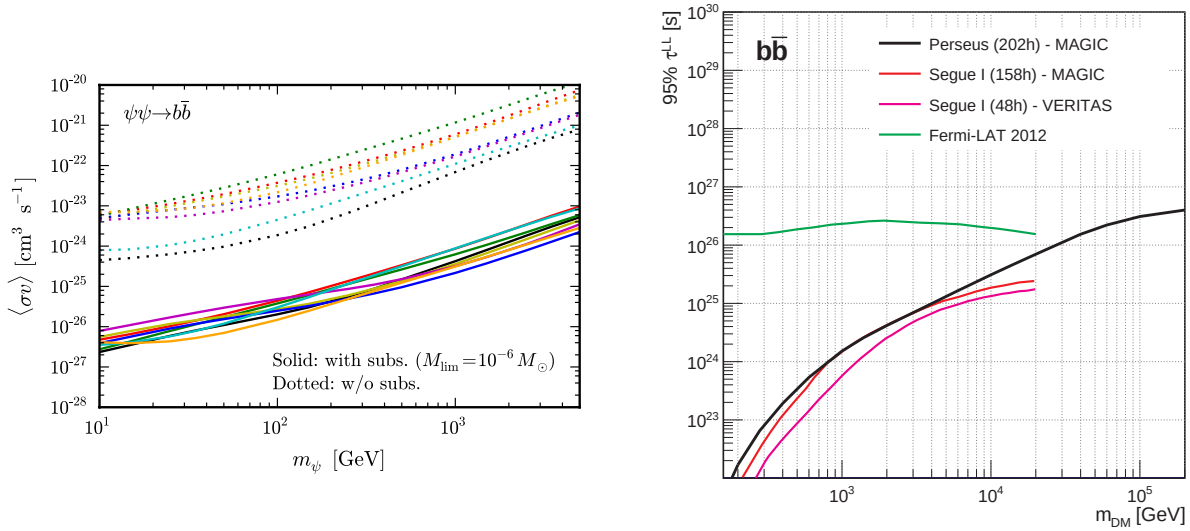

Figure 3.2: Constraints on the WIMP annihilation cross-section [158] (*left*) and decay lifetime [156] (*right*) obtained by observations of galaxy clusters. The annihilation or decay into a $\bar{b}b$ final state is assumed. Results from the analyses of eight clusters [158] are shown in the *left* panel. Solid (dotted) lines in the *left* panel correspond to the case with (without) contributions from substructures. They assume an optimistic model for the substructure boost expecting a more than 500-times enhancement of the annihilation signal. We discuss the boost factor in Chapter 5 and show that such a large value could not be achieved. In the *right* panel, the black line is the lower limit obtained by observations of the Perseus cluster. Red and magenta lines are limits obtained by observing Segue 1 dwarf spheroidal galaxy, while the green line is a limit obtained by the Galactic Center observations with *Fermi* satellite [160].

3.2.3 the Galactic Center

The Galactic Center (G.C) is the central part of the Milky Way galaxy of which J-factor is estimated to be as high as $J \sim O(10^{21})$ GeV^{2}cm^{-5} (e.g. [161, 162]). We can expect a higher flux of dark matter annihilation signal compared to the case of other targets. However, the spatial distribution of dark matter at its center is not well-determined [163–166]. If we assume a different density profile, the J-factor could be much smaller. Another problem is that astrophysical objects are densely distributed in this region. Then it is critically important to remove the "foreground" astrophysical emissions in order to detect the dark matter signal [167, 168]. The region of interest of the observations must be carefully selected.

There are claims for detections of the dark matter signature at the Galactic Center [169–171]. Excesses of GeV γ-ray emissions at the Galactic Center are found in the *Fermi* data, which can be interpreted with dark matter annihilations. The excess is referred to as the "(Galactic Center) GeV-excess". The interpretation of the GeV excess is still under discussion [172–174]. Astrophysical objects such as pulsars can also explain the GeV excess [175, 176]. Both of the astrophysical and dark matter models still contain considerable uncertainties. Recent analyses about the morphology of the GeV excess favor the astrophysical scenario since the excess is elongated along the galactic disk [177, 178] which should trace the stellar population. If the excess is produced by the dark matter annihilations, it should have a spherical emission morphology.

3.2.4 Milky Way halo

The Milky Way halo is a part of the central region of our galaxy which is slightly above the disk. Astrophysical γ-ray emitters are concentrated on the disk, then it is expected that one can significantly reduce the astrophysical contributions keeping a high J-factor. If dark matter forms a density core at the center of our Galaxy, this strategy is very efficient [182]. Strategies for dark matter search in the halo region are actively debated. Some of the latest constraints with atmospheric Cherenkov telescopes are obtained by observing this region [180, 183, 184]. Fig. 3.3 shows the current limits obtained with H.E.S.S.

3.2.5 satellite galaxies

Dark matter halos take hierarchal structures. In fact, our Galaxy associates numbers of satellite galaxies. Some of them are proposed as good targets for dark matter search. Large Magellanic Cloud (LMC) and dwarf spheroidal galaxies (dSphs) are examples. LMC is the largest satellite candidate of our Galaxy and its J-factor may reach to $J \sim O(10^{20})$ GeV^{2}cm^{-5}. Upper limits on the annihilation cross-section with observations of LMC depend on the assumption of the dark matter density profile and the models of the astrophysical contri-

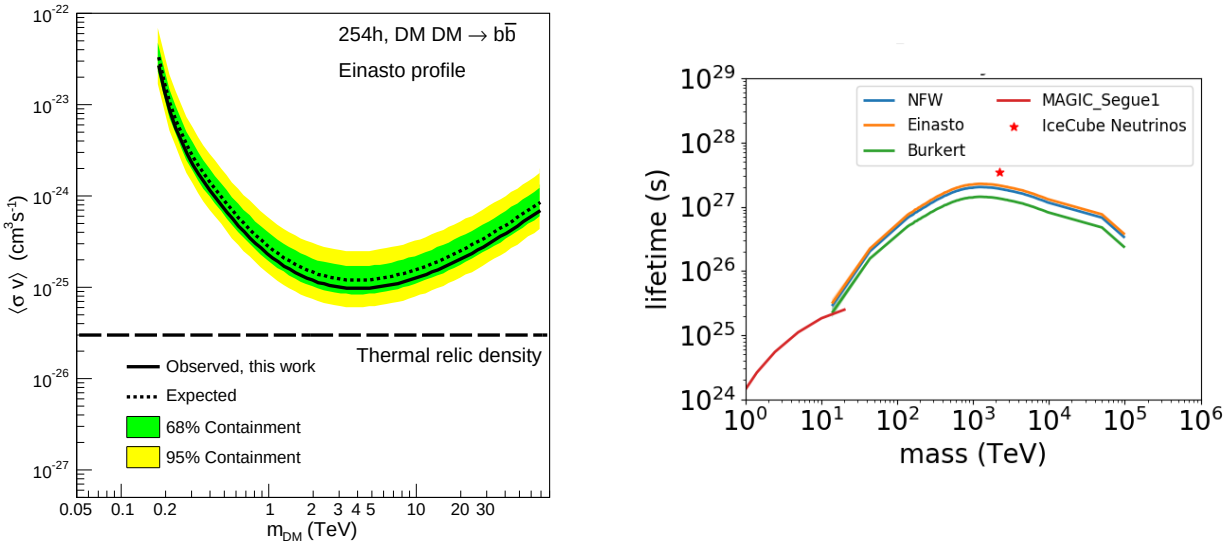

Figure 3.3: Constraints on the WIMP annihilation cross-section [179] (*left*) and decay lifetime [180] (*right*) obtained by observations of the Milky Way halo. The annihilation or decay into a $\bar{b}b$ final state is assumed. The constraints of the *left* panel [179] is obtained by 254 hours of observations. An Einasto profile of $\rho_{\rm DM} \propto \exp\left[-2\left((r/r_s)^{0.17}-1\right)/0.17\right]$ is assumed in the analysis (see [181] for detail). If the model of the profile is changed, the constraint gets ~10 times weaker. In the *right* panel, the solid lines correspond to the lower limits obtained by 15 months of observations by HAWC. Each solid line corresponds to a different model of the profile. The dependence on the dark matter density profile is weaker than the case of annihilations.

butions [185, 186]. LMC is a large enough object to host astrophysical γ-ray sources [187]. On the contrary, dSphs are relatively small and contain no astrophysical sources to emit high-energy γ-rays. The kinematics of stars in dSphs indicate that they are rich in dark matter. Their mass-to-luminosity ratio is about $M/L \sim 10^3 M_\odot/L_\odot$ [188–190]. The typical value of the J-factor is $J \sim O(10^{17} - 10^{19})$ GeV^{2}cm^{-5}. The J-factors of large enough dSphs are directly derived by fitting stellar motions (e.g. [191]). The J-factors of small and faint dSphs are estimated using a scaling law [192]. There are discussions about the dark matter density profile of each dSph. *Fermi* searches dark matter signals adopting stacking analyses of several dSphs [193–196]. Imaging atmospheric Cherenkov telescopes on the ground (MAGIC, H.E.S.S., and VERITAS) search signals by conducting deep observations on specific dSphs with high J-factors [197–201]. Those telescopes are sensitive to the signals higher than $E_\gamma \gtrsim O(1)$TeV from the heavier dark matter. The target dSphs have to be specified when we search dark matter with pointing telescopes. Dark matter signals are also searched in smaller satellites or structures of lower J-factor with HAWC experiments. They have conducted a search in dwarf irregular galaxies [202] and dark matter subclumps [203] as well as dSphs.

3.3 Indirect searches with other species

Indirect searches are also conducted with neutrino and cosmic-ray observations. The modeling at the production sites is same among species. However, the physics of their propagation and the competing astrophysical emissions are different. By combining the results of multi-messenger observations, we can obtain robust constraints on dark matter properties. In this section, we briefly explain the constraints on the WIMP dark matter annihilation cross-section obtained by observations of neutrinos and cosmic rays.

3.3.1 neutrino

Neutrinos take straight ways from the source to the Earth. So we do not have to consider the reflection. Absorptions are also negligible because they only feel the weak force [204]. The uncertainty coming from the models of the propagation is only little. However, they are less constraining compared to the γ-rays or cosmic rays [205]. Also at the lower energy regions of $E_\nu \lesssim O(10)$ GeV, the flux of the atmospheric neutrino is higher than that of the astrophysical or cosmogenic neutrino. Neutrinos from the Universe are hard to be discriminated in this energy regions. The neutrino search of dark matter is only sensitive at higher energy regions of $E \gg O(100)$ GeV. An example of the constraints on WIMP dark matter with neutrino observations is shown in Fig. 3.4. Much milder constraints than those by the γ-rays [54, 206–209] are obtained.

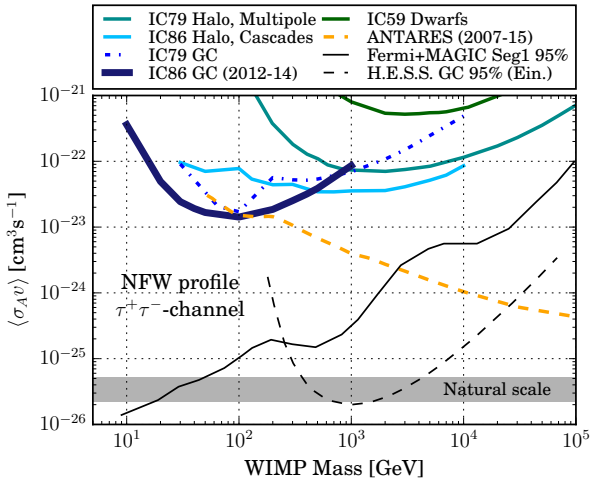

Figure 3.4: Upper limits on the WIMP annihilation cross-section into a $\tau^+\tau^-$ final state [54]. Black-thin lines correspond to the constraints by γ-ray observations. All others are those obtained by neutrino observations. In this figure, the NFW profile is assumed for Milky Way halo. If the assumption about the halo profile is changed from the NFW to the Burkert, then the constraints get milder.

3.3.2 cosmic ray

Different from neutrinos or γ-rays, charged cosmic-rays cannot arrive at the Earth straightly from the source. They are reflected by magnetic fields and diffused out during their propagations. One has to consider the propagation process carefully. Magnetic fields confine them in finite propagation regions. The size of the propagation region depends on the particle energy. To search WIMP dark matter of $m_{\rm DM} \sim O(1)$ GeV - $O(1)$TeV with cosmic-ray observations, those generated in our Galaxy are considered. A cylindrically-symmetric propagation region centered on the Galactic disk is assumed in the simplest treatment. In this case, the propagation of the cosmic ray is described with the following diffusion-propagation equation (e.g. [210–212]):

$$\frac{\partial f_i}{\partial t} - K(T)\cdot\nabla^2 f_i + \frac{\partial}{\partial z}(\mathrm{sign}(z) f V_{\rm conv}) = Q_{{\rm inj},i} - 2h\delta(z)\Gamma_{{\rm ann},i} f_i \tag{3.3.1}$$

where f_i is the flux of the cosmic-ray species i. $Q_{{\rm inj},i}$ and $\Gamma_{{\rm ann},i}$ corresponds to the injection and annihilation rate of that species, respectively. In this expression, we parametrize the vertical distance from the injection site, the disk of our Galaxy, with z. The parameters describing the propagation region are the half-halo thickness h in the z direction, the convection velocity $V_{\rm conv}$, and those in the diffusion coefficient $K(T)$. $K(T)$ is a function of the kinetic energy

T of the propagating particle and defined as

$$K(T) = K_0 \beta \left(\frac{p}{\mathrm{GeV}} \right)^{\delta}. \tag{3.3.2}$$

The relation between the parameter T and β (or p) is given by

$$\beta = \sqrt{1 - \frac{m^2}{(T+M)^2}} \tag{3.3.3}$$

$$p = \sqrt{T^2 + 2mT}. \tag{3.3.4}$$

Hence one needs to determine propagation parameters K_0, δ, h, and V_{conv}. As a boundary condition, the radius of the propagation region is conventionally taken as 20kpc. Parameters are derived by fitting the cosmic-ray data (e.g. [51, 212–217]). Once these parameters are fixed, the propagation of each species can be written with an analytical solution. Numerical tools for cosmic-ray propagations are also available in public (e.g. [218]).

One advantage of the cosmic-ray observation is that we can use several species to search for dark matter [219, 220]. For example, propagation properties of the electron (positron) and the proton (antiproton) are different. They can be regarded as different observables. However, the feasibility for detecting dark matter signatures with cosmic-ray observations are highly sensitive to the choice of the propagation parameters. The constraints obtained in some of the recent works are comparable to or stronger than those of γ-ray observations [221–225].

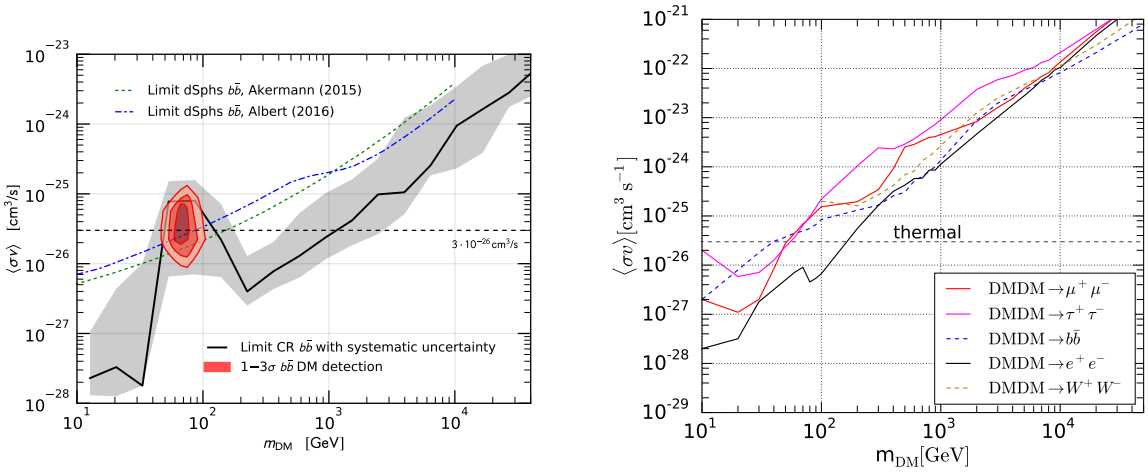

Figure 3.5: Upper limits on the WIMP annihilation cross-section obtained with observations of anti-protons (*left*) [224] and positrons (*right*) [223]. In the *left* panel, the dark matter annihilation into $\bar{b}b$ is considered. Blue and green lines are constraints from γ-ray observations. The red region is a best-fit point for the possible excess of the signal. In the *right* panel, a comparison between different annihilation channels are shown.

Chapter 4

Dark matter annihilation signals in dwarf spheroidal galaxies with CTA

In the previous chapter, we show the importance of γ-ray observations to search for dark matter. Elaborated strategies are needed to derive the property of dark matter. In the near future, Cherenkov Telescope Array (CTA) starts its operations and are expected to update the current understandings of dark matter significantly. CTA is the best facility to search dark matter of $m_{\rm DM} \gtrsim O(1)$ TeV with γ-ray observations. Its sensitivity is better than the current facilities by a factor of $\sim$10 for γ-rays of $E_\gamma \sim O(1)$ TeV. The angular resolution is finer than $\Delta\theta \sim$0.05 degrees in that energy range. The spatial structure of the target is especially important for observations with CTA. We consider dark matter searches in dwarf spheroidal galaxies (dSphs), which are used to search WIMP dark matter with *Fermi* satellite, with CTA. In this work, we show that the dark matter density profile of dSphs should affect the feasibility of detecting dark matter. This effect is different from that originates from the well-known dependence on the J-factor. We derive quantitative estimates about the dependence of the detectability of dark matter on the density profiles in target dSphs.

This work is based on the paper [226] which is being reviewed under the Speaker's and Publication Office of CTA. The author of the thesis is responsible for the whole contents of this chapter. In Sec. 4.1 we summarize the properties of the CTA and its strategies. Sec. 4.2 explains our targets, dSphs. Our method is explained in Sec. 4.3. The results are shown in Sec. 4.4. After discussing the energy dependence in Sec. 4.5, we summarize in Sec. 4.6.

4.1 Cherenkov Telescope Array (CTA)

4.1.1 general properties

Cherenkov Telescope Array (CTA) is a next-generation project of very-high-energy γ-ray observations [227–230]. It is sensitive to the γ-rays of $E_\gamma \sim$ 20GeV to ~300TeV. Very-high-energy photons from the universe initiate cascade showers of electron-positron pairs and photons when they enter the Earth's atmosphere. Cascading particles emit Cherenkov photons in UV to optical wavelength. CTA detects the very-high-energy γ-rays by collecting these Cherenkov photons with telescope array on the ground. The details of the detection principle are explained in Appendix D. In order to cover the whole sky, two telescope arrays are being constructed in two sites: La Palma, Spain (CTA North) and Paranal, Chili (CTA South). At each site, Large-Sized telescopes (LSTs), Medium-Sized Telescopes (MSTs) and Small-Sized Telescopes (SSTs) work in combinations. La Palma site holds 4 LSTs and 15 MSTs while Paranal site holds 4LSTs, 25 MSTs, and 70 SSTs. Because of the different array configurations, the sensitivity is different between two sites. The configuration of the array is shown in Fig. 4.1.

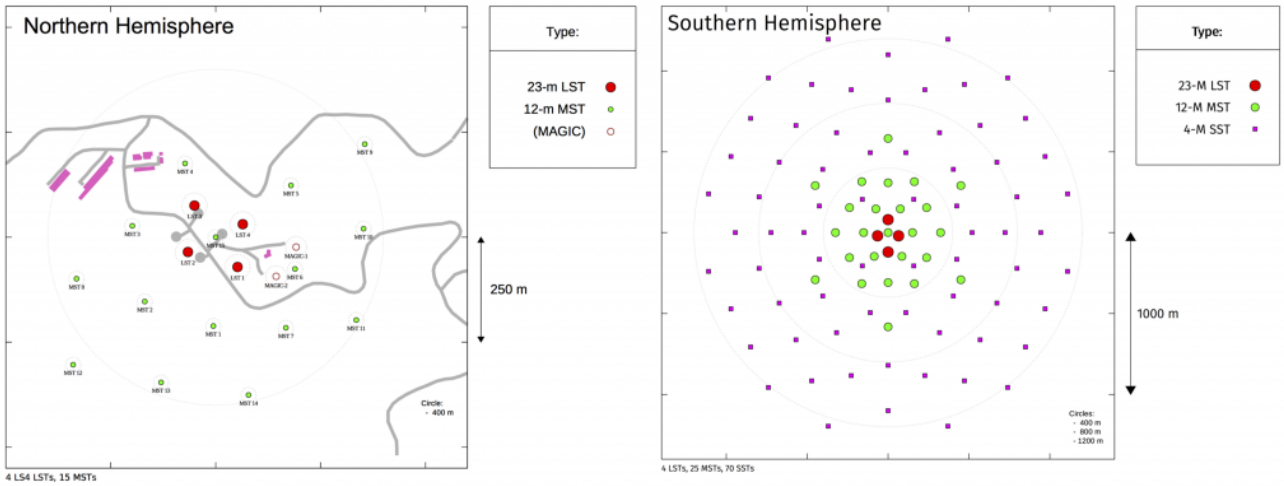

Figure 4.1: Configurations of the telescopes at the Northern (*left*) and the Southern (*right*) site. The Northern site does not have SSTs [231]. This result in the better sensitivity of the Southern sight at the higher energy region of $\gtrsim O(10)$ TeV. The array extends to a $\sim 800m \times 800m$ region in the Northern site and a $\sim 2.5km \times 2.5km$ region in the Southern site.

The designed sensitivity for γ-rays of $E_\gamma \sim O(1)$ TeV is better than by a factor of ∼10 compared to the current facilities. In Fig. 4.2, we show the differential sensitivity to detect a point source. CTA requires three conditions for the detection of a source [232].

- The statistical significance of the source $S \geq 5$
- The number of γ-ray event $N_\gamma \geq 10$
- The ratio of the γ-ray and the background event $N_\gamma/N_{\rm bkg} \geq 0.05$

The significance is determined using Eq.(17) of [233]. At lower energies, background event by cosmic-rays determine the sensitivity then the first condition works. At higher energies where the background events by cosmic-rays are rare enough, the sensitivity is limited by the statistics and is determined by the second and the third condition. The three conditions above implicitly assume that the observation time on the source region is 5 times smaller than that of the off-source region. Also, the sensitivity curve in Fig. 4.2 assumes an on-axis observation, i.e, an observation of a source locating at the center of the field of view of the telescope. At lower energy regions, the sensitivity decreases for off-axis observations while it does not at higher energy regions. This is shown in Fig. 4.3.

Other important properties of the CTA instrument are the angular and energy resolution. Both resolutions are significantly improved. Fig. 4.4 shows the angular resolution. CTA can resolve the angular scale down to $\Delta\theta \sim 0.04$ degrees at $E_\gamma \gtrsim O(1)$ TeV. The angular resolution of the CTA is finer than those of any other telescopes at $E_\gamma \gtrsim 200$ GeV [231]. About the energy resolution, $\Delta E/E \sim 0.1$ is achieved as shown in Fig. 4.5. The energy resolution of CTA is better than the other atmospheric Cherenkov telescopes by factors [234] and comparable to that of the *Fermi* satellite [235].

4.1.2 dark matter search with CTA

There remains an unexplored region for WIMP dark matter of $m_{\rm DM} \gtrsim O(1)$ TeV as explained in Sec. 2.2.1. CTA is the best facility to search the region. The importance of the dark matter search is approved and the program is picked up in the *Key Science Project (KSP)* of CTA [230]. Among the listed targets for the γ-ray search of dark matter in Sec. 3.1, four targets are selected in the *KSP*: the Galactic Center (G.C.), dwarf spheroidal galaxies (dSphs), Large Magellanic Cloud (LMC), and galaxy clusters. In this thesis, we focus on the dark matter search in dSphs. Different from the other targets listed in the *KSP*, dSphs do not contain astrophysical sources of the high-energy γ-ray emissions. This is one reason that *Fermi* constrains the annihilation cross-section for WIMP dark matter of $m_{\rm DM} \lesssim O(100)$ GeV in an efficient way. In the next section (Sec. 4.2), we review the property of the dSph.

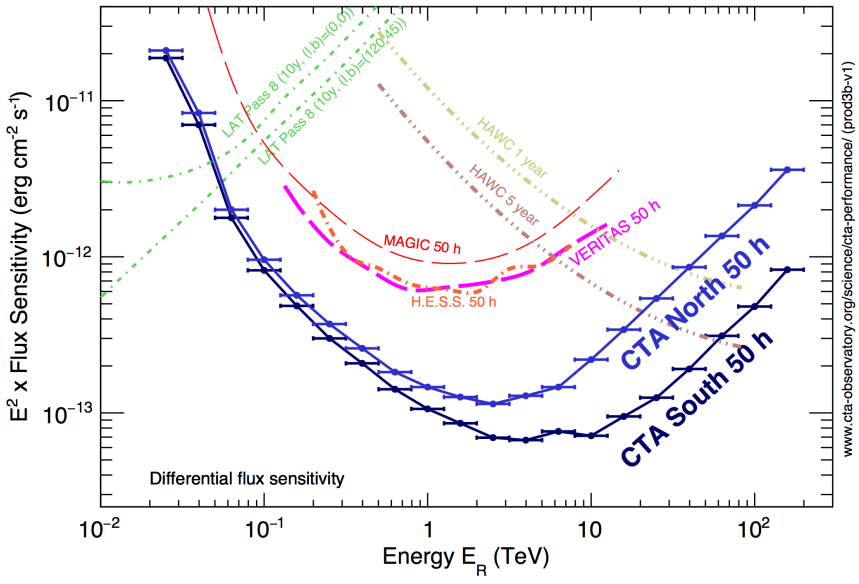

Figure 4.2: Designed sensitivities of the full-speck CTA array [231] is shown with two blue lines. Observation of a point source with the zenith angle of 20 degrees is assumed. Sensitivities of the other facilities are also shown for comparison. Note that for *Fermi* and *HAWC*, the sensitivities are evaluated using the time from the beginning of the projects. They are continuously monitoring the sky.

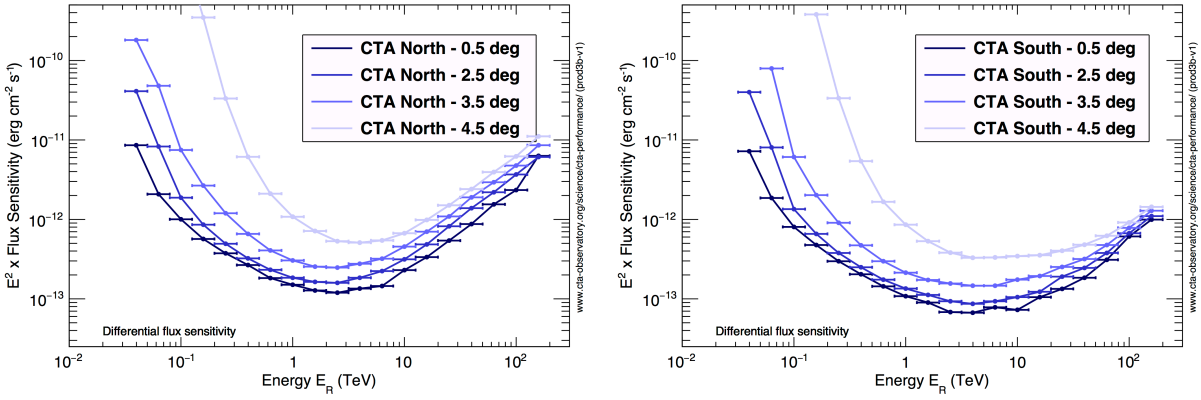

Figure 4.3: Off-axis sensitivity at each site [231]. *Left* and *right* panel corresponds to the Northern and Southern site, respectively. At higher energy regions, the sensitivity does not decrease because it is determined by the detection number of events rather than the statistical significance.

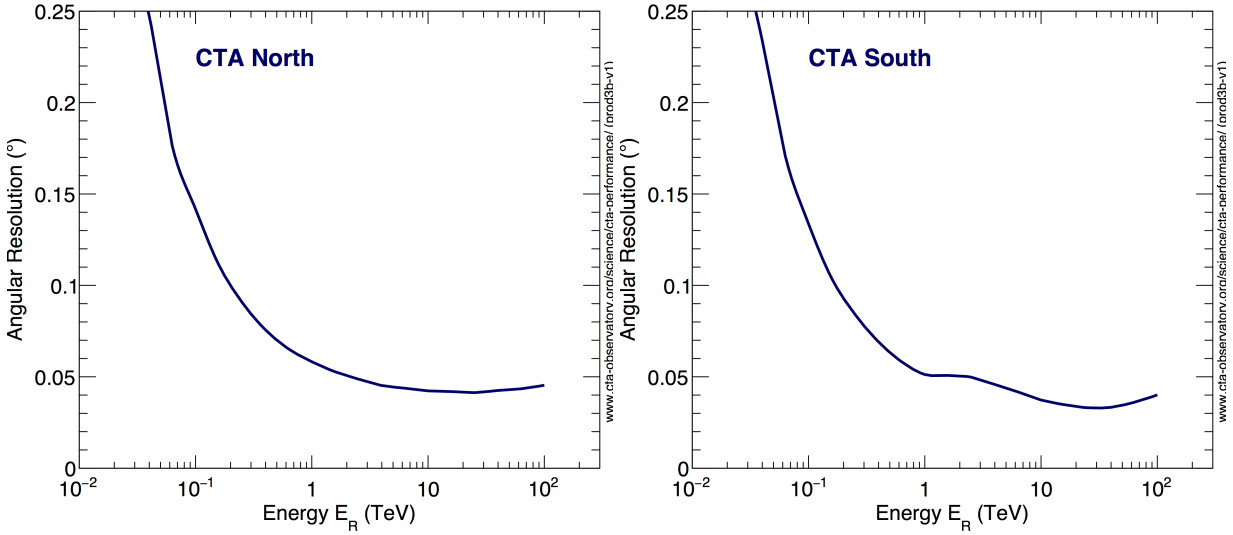

Figure 4.4: The angular resolution at each site [231]. *Left* (*right*) panel corresponds to the Northern (Southern) site. For comparison, *Fermi* has $\Delta\theta \lesssim 0.1^\circ$ at $O(100)$ GeV, and HAWC has $\Delta\theta \gtrsim 0.1^\circ$ at $E_\gamma \lesssim O(100)$GeV. No other facilities can resolve the angular scale smaller than $\sim 0.07^\circ$ at 100GeV-100TeV [235, 236].

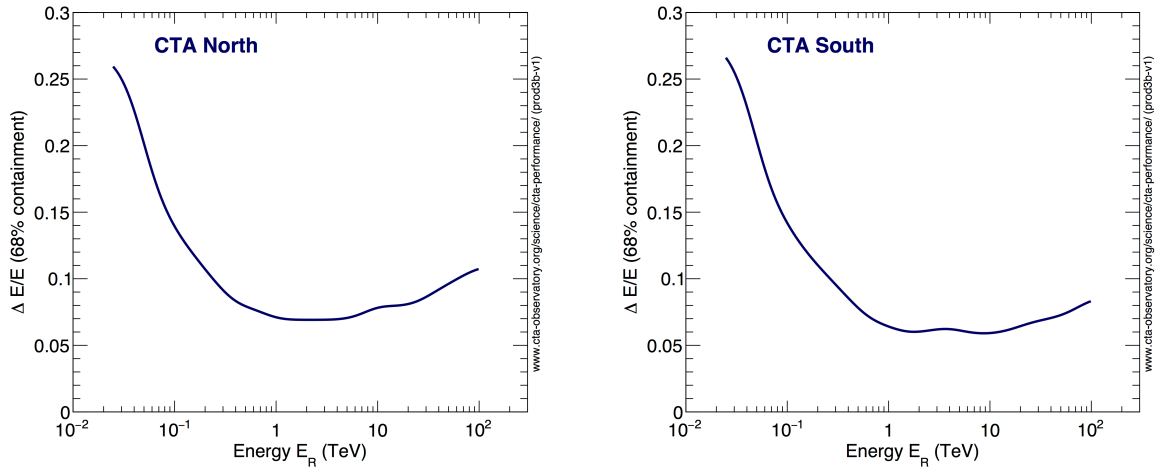

Figure 4.5: The energy resolution at each site [231]. *Left* (*right*) panel corresponds to the Northern (Southern) site. The array configuration of each site is the reason of the difference between the resolutions.

4.2 Dwarf spheroidal galaxies (dSphs)

The importance of dSphs in dark matter search is first pointed out in [237] and later in [238]. They are satellite galaxies of our Galaxy and spatially extended objects of $\Delta\theta \lesssim O(1)$ degrees. Several tens of dSphs are already identified with available stellar kinematics data. The number of the confirmed dSph is continuously increasing [239–248]. The up-to-date list of dSphs including candidates are shown in Appendix E. Most of them are located in high latitude regions of our Galaxy. The motions of the stars in dSphs indicate that they are dense with dark matter [249–251]. The mass-to-luminosity ratios of dSphs reaches to $M/L \sim 10^3 M_\odot/L_\odot$ [188–190, 192, 252]. The total mass is estimated to be $M \sim O(10^6 - 10^8) M_\odot$. No astrophysical objects which can emit γ-rays are detected in dSphs. Exceptions are the possible detection of the γ-ray signal from unknown sources [45, 253].

As explained in Sec. 3, observations of dSphs with *Fermi* satellite put the strongest constraints on the annihilation cross-section for WIMP dark matter of $m_{\rm DM} \sim O(1) - O(100)$ GeV. Since *Fermi* is a survey-type telescope, a stacking analysis using data of several dSphs is one good strategy [45, 76, 254–257]. Observations of dSphs with atmospheric Cherenkov telescopes give upper limits on the annihilation cross-section for heavier dark matter of $m_{\rm DM} \gtrsim O(1)$ TeV. The strategy with atmospheric Cherenkov telescopes is different from that of the *Fermi* satellite. The target dSphs in which we search for dark matter must be specified in advance. The signatures of dark matter are searched through deep observations of selected dSphs [193–195, 197, 198, 198, 199, 258–265]. Target dSphs have been selected by their J-factors.

The J-factor is calculated from the density profile of dark matter $\rho_{\rm DM}(r)$ as

$$J = \int d\Omega \int_{l.o.s} ds \rho_{\rm DM}(r)^2 \tag{4.2.1}$$

$$= 2\pi \int^{\theta} d\theta \sin\theta \int_{-\infty}^{\infty} db\ \rho_{\rm DM}(\sqrt{b^2 + d^2 \sin^2\theta}) \tag{4.2.2}$$

where d is the distance from the Earth to the center of the dSph, r is the distance measured from the center of the dSph, and θ is the viewing angle. The parameter b corresponds to the line element. See Fig. 4.6 for the definition of the parameters in Eq. (4.2.1). In general case, the density profile $\rho_{\rm DM}(r)$ is characterized with several parameters. The profile parameters are determined by fitting stellar motions in the target dSph. The number of available stars for the fitting ranges from $O(1)$ to $O(100)$. When the available stellar data is not enough, the density profile is not well-determined (see Appendix of [250] for example). In such cases, the error regions of J-factors extend in several orders-of-magnitude. Furthermore, there are patterns of models for density profiles. Hence the J-factor, which is calculated from the density profile, has a large uncertainty. Fig. 4.7 shows an example. J-factors of 24 dSphs obtained with different models of profiles are shown. For seven dSphs labeled

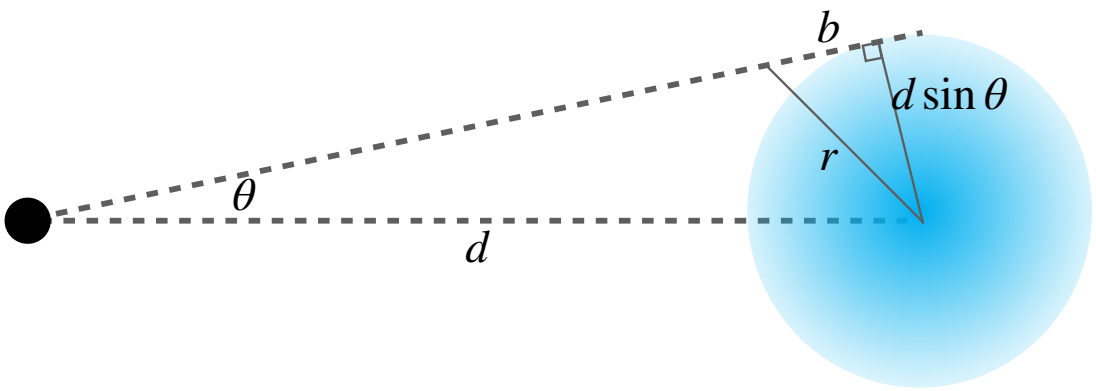

Figure 4.6: The definition of parameters to calculate the J-factor.

as "Car (Carina)", "For (Fornax)", "Scu (Sculptor)", "Sex (Sextans)", "Dra (Draco)", "Leo1", and "Leo2" in Fig. 4.7, the J-factor derived with different models agrees in the same order-of-magnitude. The quality of the stellar data is sufficient for these dSphs. They are so-called "classical dwarfs" which are already known in [252].

Considering the dark matter search in dSphs with CTA, the understanding of the dark matter density profile, $\rho_{\rm DM}(r)$, is more important than cases of current observations. When the angular resolution of the facility is larger compared to the spatial extension of the target dSph, the details of the density profile do not affect the sensitivity (see the Supplement of [257] for example). In such a situation, the J-factor is the only criterion to determine the "goodness of the target". However, the angular resolution of the CTA facility is much finer than the spatial extensions of typical dSphs. As shown Fig. 4.4, the angular resolution of the CTA is $\Delta\theta \sim 0.1$ degrees at E_γ ~100GeV and $\Delta\theta \sim 0.04$ degrees at $E_\gamma \gtrsim 1$ TeV, while dSphs extend to $\Delta\theta \lesssim O(1)$ degrees. Dark matter distributions at the center of dSphs are resolved with CTA. The importance of the density profile was already pointed out in earlier works (e.g. [250, 267]). The situation is realized with the CTA for the first time. The importance of the spatial extensions of dSphs for atmospheric Cherenkov telescopes are recognized very recently and included in the latest analyses [195, 197, 268]. The upper limits on the dark matter annihilation cross-section tend to get milder compared to the case assuming point sources.

In this thesis, we study how the density profile of dark matter in dSph affect the feasibility of detecting dark matter with CTA. For this purpose, we select Draco dSph for our target. As shown in Fig. 4.7, the J-factor of Draco dSph is almost fixed to $\log_{10} J \sim 19$. The J-factor is measured in the unit of [GeV^{2}cm^{-5}] throughout this thesis. The J-factor of Draco dSph is the highest among the classical dwarfs. Also, numbers of models with several parameters are

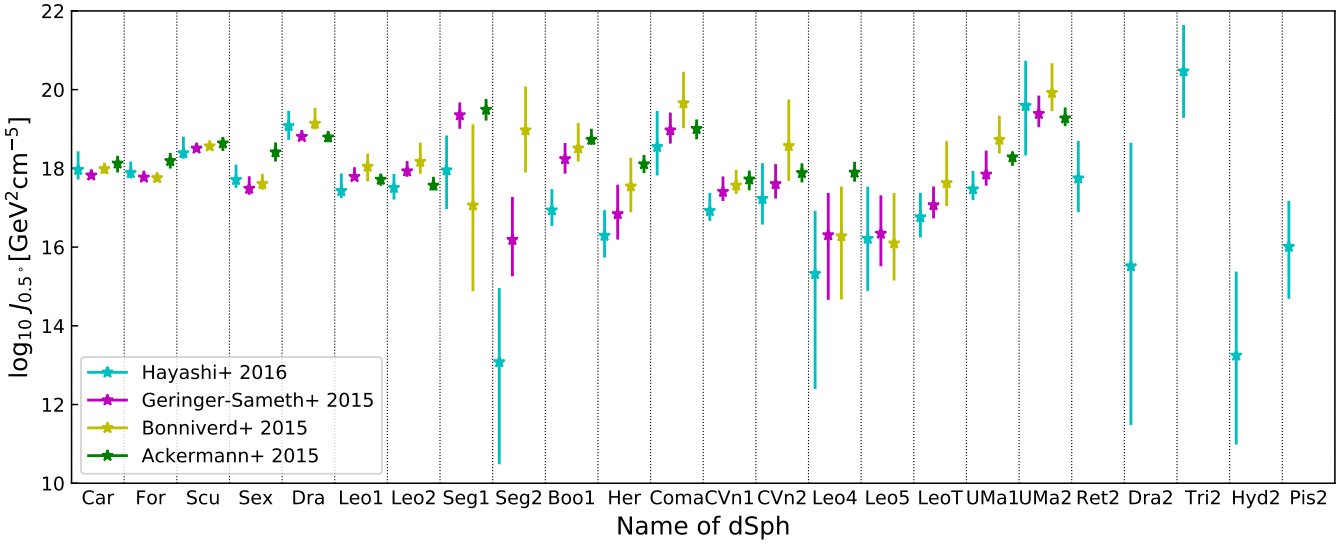

Figure 4.7: The J-factor of dSphs calculated with several models [191, 251, 257, 266]. The y-axis of the figure is $\log_{10} J_{0.5^\circ}$ where $J_{0.5^\circ}$ is defined as the J-factor integrated to the solid angle of 0.5 degrees. Data points are taken from [251]. Cyan points are J-factor derived by fitting dSphs with axisymmetric density profiles. Spherical profiles are assumed to derive other points.

available for this dSph [191,249,263,269–272] which enables us to investigate the dependence on the dark matter density profile. We simulate the observation of Draco dSph with CTA and derive the sensitivity for dark matter assuming different density profiles. We show that the difference in the shape of the density profile affects the sensitivity in a different way from that of the J-factor calculated from the profile $\rho_{\rm DM}(r)$. We quantify the dependence on the profile for the first time. For simulations of the observations with CTA and the data analyses, we use `ctools` [273]. We explain our analyses in the next section (Sec. 4.3),

4.3 Method

4.3.1 analysis with `ctools`

We use `ctools` [273] to evaluate the feasibility of detecting dark matter in several profiles of dSphs. `ctools` is an open source software provided for the scientific study using γ-ray data. Packages to simulate eventdata for each observing facility (e.g. CTA) as well as to analyze real data are included. Observing facilities are specified with the calibration database and instrumental response functions (IRFs). Those files are given separately from `ctools`. We simulate the data of CTA observations using a calibration database `prod3b` provided by CTA consortium [274]. Following the procedures of the real data analysis, we select and bin the event then conduct likelihood analyses.

Several IRFs with different zenith angles and duration of the observations are provided in the `prod3b` calibration database [274]. This is the latest version available in public. Each IRF adopts a different cut on backgrounds to optimize the flux sensitivity. Two types of backgrounds exist for observations with CTA. The first one is the *night sky background*, which is the noise by optical or UV photons competing with the Cherenkov photons. A dark sky condition, observations of a clear sky without moonlight at a remote site, is assumed for the night sky backgrounds. The contributions from the background UV photons are negligible when the duration of the observation is long enough. The other background originates from particles different from photons that produce similar Cherenkov shower images. Atmospheric muons, nuclei, protons, and electrons (positrons) have to be removed. Atmospheric muons can be eliminated effectively by observing with multiple telescopes. Nuclei heavier than helium are discriminated by the shower morphology. Those particles are not simulated in any of the provided IRFs. Protons and electrons (positrons) are remaining backgrounds. Depending on the zenith angle and the duration of the observation, different cuts are adopted. The cuts are based on the Monte-Carlo simulations of the air shower using [275]. The input spectra of the cosmic-rays are fitted to observations [276–278]. The residual charged cosmic-rays after cuts are the backgrounds simulated in each IRF. We select the IRF `North_z20_average_50h` for our calculations. This IRF is an appropriate one for a

long-time observation of Draco dSph in the Northern sky with CTA.

Assuming a 500-hour observation of Draco dSph with CTA, we generate a list of event-data. We do not simulate any additional sources in our region of interest hence the eventdata is determined by the IRF. Events correspond to the γ-ray of $E_\gamma = [0.03, 180]$ TeV in $4^\circ \times 4^\circ$ region centered on the Draco are selected and binned to conduct likelihood analyses. The binning is 0.03° in space and 5 bins per decade in logarithmic scale in energy. Likelihood ratio tests are performed with the binned data using Poisson statistics. We derive 2σ confidence-level upper-limits on the γ-ray flux by requiring

$$2\ln L(X_{\rm bkg+src}) - 2\ln L(X_{\rm bkg}) = 4 \tag{4.3.1}$$

where $\ln L(X)$ is a maximum likelihood with the model X. The suffix of the model X, "bkg" and "bkg+src", corresponds to the background only and a (background + dark matter signal) case, respectively. The likelihood function for the Poisson statistics is

$$-\ln L(X) = \sum_k \left[n_{{\rm exp},k}(X) - n_{{\rm obs},k} \ln n_{{\rm exp},k}(X) \right] \tag{4.3.2}$$

where $n_{{\rm obs},k}$ is the observed number of event in the k-th data bin. The predicted number of the events in that bin is expressed as $n_{{\rm exp},k}$. The predicted number of event in the k-th bin is the integral of the probability density in a certain interval of the space, energy and the time

$$n_{{\rm exp},k} = P(\mathbf{x}_k, E_k, t_k|X) \times \Delta\Omega_k \Delta E_k \Delta t_k. \tag{4.3.3}$$

We use $\mathbf{x}_k$ to refer the instrument direction and E_k, t_k to the reconstructed energy and the trigger time. $P(X)$ is $P(X_{\rm bkg})$ for the background, and $P(X_{\rm bkg+src})$=$P(X_{\rm bkg})$ + $P(X_{\rm src})$ when a source is included. The probability density $P(X)$ depends on the IRF as

$$P(\mathbf{x}, E, t|X) = \int d\mathbf{x}' \int dE' \int dt' \ {\rm IRF}(\mathbf{x}, E, t|\mathbf{x}', E', t') \times F(\mathbf{x}', E, t'|X) \tag{4.3.4}$$

where $\mathbf{x}'$, E', and t' are quantities at the source. The model X is characterized with the model function $F(\mathbf{x}', E, t'|X) = F(\mathbf{x}', E, t')$. It can be decomposed into space, energy, and time as

$$F(\mathbf{x}, E, t) = F_{\rm space}(\mathbf{x}|E, t) \times F_{\rm energy}(E|t) \times F_{\rm time}(t). \tag{4.3.5}$$

Functions correspond to models with dark matter signals are given in Sec. 4.3.3 and Sec. 4.3.4. The model function for time $F_{\rm time}$ is assumed to be a constant. In Eq. (4.3.4), the IRF consists of

$${\rm IRF}(\mathbf{x}, {\rm E}, {\rm t}|\mathbf{x}', {\rm E}', {\rm t}') = A_{\rm eff}(\mathbf{x}, E, t) \times {\rm PSF}(\mathbf{x}|\mathbf{x}', E', t') \times E_{\rm disp}(E|\mathbf{x}', E', t'). \tag{4.3.6}$$

The effective area $A_{\rm eff}$, the point spread function PSF, and the energy dispersion $E_{\rm disp}$ depends on the cut. The energy dispersion is included in our analyses.

4.3.2 background

The background energy spectrum in our region of interest is shown in Fig. 4.8. Fig. 4.9 shows the number count of the background events integrated over energy in each pixel. The map corresponds to our region of interest, a $4^\circ \times 4^\circ$ region centered on the Draco, and the value is normalized with the number at the maximum pixel. At the edges of our region of interest, the number of the accepted background events slightly decreases. The residual cosmic-rays after the event cuts are responsible for the spectrum and the count map in Fig. 4.8 and Fig. 4.9. In Figs. 4.8 and 4.9,we shows the quantity per second.

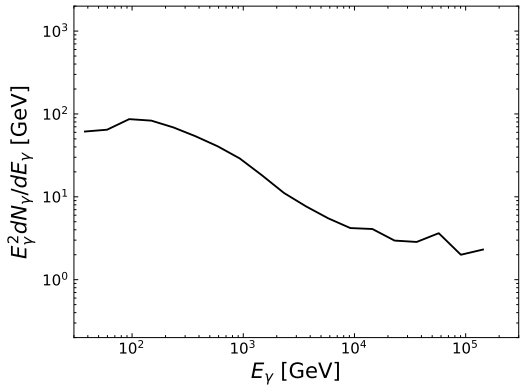

Figure 4.8: Reconstructed energy spectrum of the background event. The x-axis is the reconstructed γ-ray energy and the y-axis is the corresponding flux per second.

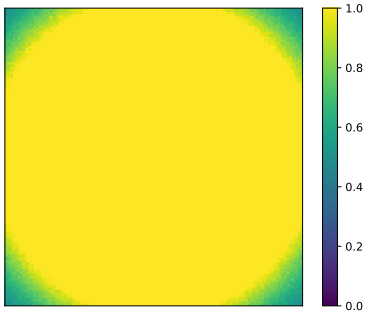

Figure 4.9: The number count of the photons in the range of $E_\gamma = [0.03, 180]$ TeV, normalized with the value at the maximum pixel. A $4^\circ \times 4^\circ$ region centered on the Draco is shown, i.e., the edges of the figure correspond to the edges of our region of interest.

4.3.3 dark matter density profiles of the source

A point source is the simplest model for a target dSph when the angular size of the target is small enough compared to the angular resolution of the observing facilities. Considering observations of dSphs with CTA, target dSphs should be treated as extended sources. Taking Draco dSph as an example, we sample the profile to investigate how the spatial extension of the target dSph affects the accessible region of the dark matter annihilation cross-section. We limit our analyses in spherical profiles for simplicity. Our sample profiles are categorized into three types:

1. generalized NFW (gNFW) profile [279, 280]

$$\rho(r) = \rho_s \left(\frac{r}{r_s}\right)^{-\gamma} \left(1 + \left(\frac{r}{r_s}\right)^{\alpha}\right)^{-\frac{\beta-\gamma}{\alpha}} \tag{4.3.7}$$

   When (α, β, γ)=(1, 3, 1), it corresponds to the original NFW profile in [281].

2. Burkert profile [282]

$$\rho(r) = \rho_s \left(1 + \frac{r}{r_s}\right)^{-1} \left(1 + \left(\frac{r}{r_s}\right)^{2}\right)^{-1} \tag{4.3.8}$$

3. power law (PL) with an exponential cutoff profile

$$\rho(r) = \rho_s \left(\frac{r}{r_s}\right)^{-\alpha} \exp\left[-\frac{r}{r_s}\right] \tag{4.3.9}$$

ρ_s is the normalization of the dark matter density and r_s is the scale radius of the profile measuring the distance r from the center of the target. Fig. 4.10 shows examples. More detailed profiles such as not spherical cases or profiles with substructures are discussed in [251, 283–285].

Table 4.1 summarizes our reference profiles with the explicit expressions of each profile, profile type corresponding to Eqs. (4.3.7), (4.3.7), and(4.3.7), the J-factor integrated over the solid angle of 0.5 degrees ($J_{<0.5^\circ}$), and the J-factor integrated over a $4.0^\circ \times 4.0^\circ$ region ($J_{\rm tot}$) which corresponds to the size of the region of interest for our analyses. $J_{<0.5^\circ}$ is shown just for comparison with previous works and we do not use this quantity in our analyses. The next column, θ_{90} is a new quantity which characterizes the length scale of the profile. θ_{90} is defined as the radius of $J_{<\theta_{90}} = 0.9 J_{\rm tot}$ (see Sec. 4.5). The distance from the Earth (in the unit of kpc) and the reference are shown in the last two columns. We also assign identification numbers in the first column for convenience. Note that we do not introduce a truncation radius in our analyses. The truncation radius is usually determined as the radius of the outermost member star or the virial radius of the dark matter halo. If we take the former for

Table 4.1: Dark matter density profiles for Draco dSphs we use in our analyses. Identification numbers are assigned for convenience and shown in the first column. We adopt the median value for the parameters for each profile.

No.	expression	type	$\log_{10}J_{<0.5^\circ}$ [GeV^2/cm^5]	$\log_{10}J_{\rm tot}$ [GeV^2/cm^5]	θ_{90} [degree]	distance [kpc]	Ref.
1	$\left(\frac{1.7\mathrm{GeV}}{\mathrm{cm}^3}\right)\left(\frac{r}{0.79\mathrm{kpc}}\right)^{-1}\left(1+\frac{r}{0.79\mathrm{kpc}}\right)^{-2}$	NFW	18.40	18.45	0.50	80	[249]
2	$\left(\frac{0.69\mathrm{GeV}}{\mathrm{cm}^3}\right)\left(\frac{r}{3.7\mathrm{kpc}}\right)^{-0.71}\left(1+\left(\frac{r}{3.7\mathrm{kpc}}\right)^{2.01}\right)^{-2.80}$	gNFW	19.00	19.44	1.52	76	[191]
3	$\left(\frac{16.3\mathrm{GeV}}{\mathrm{cm}^3}\right)\left(1+\frac{r}{0.67\mathrm{kpc}}\right)^{-3}$	g NFW	19.08	19.29	1.12		
4	$\left(\frac{1.23\mathrm{GeV}}{\mathrm{cm}^3}\right)\left(\frac{r}{1.30\mathrm{kpc}}\right)^{-1}\left(1+\frac{r}{1.30\mathrm{kpc}}\right)^{-2}$	NFW	18.80	18.91	0.85	72	[269]
5	$\left(\frac{0.18\mathrm{GeV}}{\mathrm{cm}^3}\right)\left(\frac{r}{1.99\mathrm{kpc}}\right)^{-1.5}\left(1+\frac{r}{1.99\mathrm{kpc}}\right)^{-1.5}$	g NFW	18.88	18.90	0.30		
6	$\left(\frac{5.9\mathrm{GeV}}{\mathrm{cm}^3}\right)\left(\frac{r}{0.32\mathrm{kpc}}\right)^{-1}\exp\left[-\frac{r}{0.32\mathrm{kpc}}\right]$	PL + cutoff	18.53	18.53	0.26	80	[270]
7	$\left(\frac{4.76\mathrm{GeV}}{\mathrm{cm}^3}\right)\left(1+\frac{r}{1.41\mathrm{kpc}}\right)^{-1}\left(1+\left(\frac{r}{1.41\mathrm{kpc}}\right)^{2}\right)^{-1}$	Burkert	19.08	19.56	1.53		
8	$\left(\frac{13.4\mathrm{GeV}}{\mathrm{cm}^3}\right)\left(1+\frac{r}{0.35\mathrm{kpc}}\right)^{-1}\left(1+\left(\frac{r}{0.35\mathrm{kpc}}\right)^{2}\right)^{-1}$	Burkert	18.65	18.70	0.50		
9	$\left(\frac{37.8\mathrm{GeV}}{\mathrm{cm}^3}\right)\left(1+\frac{r}{0.18\mathrm{kpc}}\right)^{-1}\left(1+\left(\frac{r}{0.18\mathrm{kpc}}\right)^{2}\right)^{-1}$	Burkert	18.69	18.70	0.28		
10	$\left(\frac{0.60\mathrm{GeV}}{\mathrm{cm}^3}\right)\left(\frac{r}{2.82\mathrm{kpc}}\right)^{-1}\left(1+\frac{r}{2.82\mathrm{kpc}}\right)^{-2}$	NFW	18.95	19.15	1.22	82	[271]
11	$\left(\frac{1.70\mathrm{GeV}}{\mathrm{cm}^3}\right)\left(\frac{r}{1.00\mathrm{kpc}}\right)^{-1}\left(1+\frac{r}{1.00\mathrm{kpc}}\right)^{-2}$	NFW	18.67	18.73	0.62		
12	$\left(\frac{4.76\mathrm{GeV}}{\mathrm{cm}^3}\right)\left(\frac{r}{0.50\mathrm{kpc}}\right)^{-1}\left(1+\frac{r}{0.50\mathrm{kpc}}\right)^{-2}$	NFW	18.70	18.72	0.33		
13	$\left(\frac{13.4\mathrm{GeV}}{\mathrm{cm}^3}\right)\left(\frac{r}{0.25\mathrm{kpc}}\right)^{-1}\left(1+\frac{r}{0.25\mathrm{kpc}}\right)^{-2}$	NFW	18.70	18.70	0.22		
14	$\left(\frac{37.8\mathrm{GeV}}{\mathrm{cm}^3}\right)\left(\frac{r}{0.18\mathrm{kpc}}\right)^{-1}\left(1+\frac{r}{0.18\mathrm{kpc}}\right)^{-2}$	NFW	19.15	19.15	0.14		
15	$\left(\frac{0.95\mathrm{GeV}}{\mathrm{cm}^3}\right)\left(\frac{r}{1.19\mathrm{kpc}}\right)^{-1}\exp\left[-\frac{r}{1.19\mathrm{kpc}}\right]$	PL + cutoff	18.58	18.69	0.80	80	[272]
16	$\left(\frac{12.7\mathrm{GeV}}{\mathrm{cm}^3}\right)\exp\left[-\frac{r}{0.24\mathrm{kpc}}\right]$	PL + cutoff	18.56	18.58	0.41		

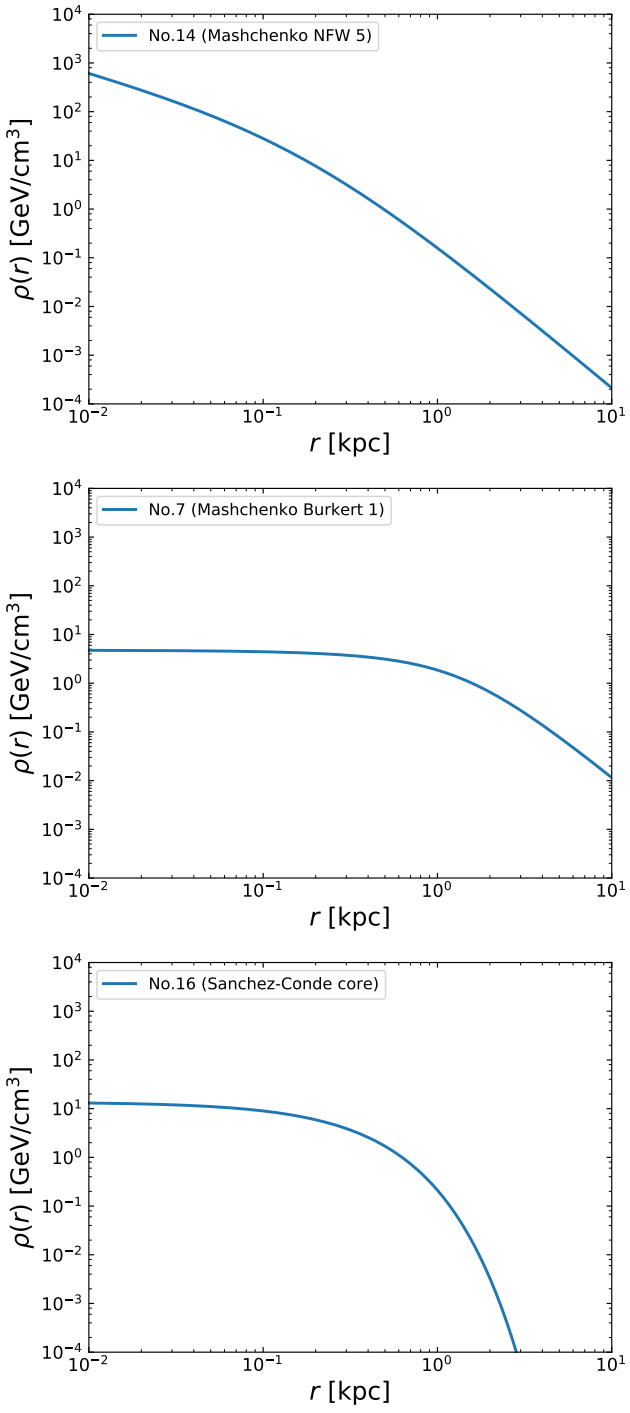

Figure 4.10: Examples of dark matter density profiles in our analyses. *Top*: NFW profile of model 5 in [271]. *Middle*: Burkert profile of model 1 in [271]. *Bottom*: (power-law of index 0) + cutoff profile in [272]. The horizontal axis represents the distance measured from the center of the dSph. Numbers in the legends correspond to those in Table 4.1.

the truncation radius, then it corresponds to 1.3 degrees [191]. On the other hand, the virial radius is highly model-dependent. Actual radial extensions of the target dSph are still under discussion. We chose our region of interest to cover the outermost member star, avoiding the introduction of an additional model parameter. The J-factor integrated over the solid angle of 1.3 degrees and $J_{\rm tot}$ differ by at most ∼10%. The value of the $J_{\rm tot}$ is almost saturated in our region of interest for any of the profiles in Table 4.1.

In Table 4.1, we show the median values of the profile parameter for each profile. Templates of the J-factor centered on the target is generated adopting the values in Table 4.1. The spatial resolution of our template is 0.01degrees. In practice, we produce templates larger than the region of interest then use parts corresponding to the $4^\circ \times 4^\circ$ region centered on the Draco to conduct calculations. Fig. 4.11 shows the relative J-factor corresponding to the density profiles shown in Fig. 4.10. In Fig. 4.11, the J-factor is normalized by the value at the center pixel. These templates correspond to the function $F_{\rm space}$ in Eq. (4.3.5), which is used to characterize the space component of the dark matter signal hypothesis.

4.3.4 spectrum of the dark matter annihilation at the source

Corresponding to the energy component $F_{\rm energy}$ in Eq. (4.3.5), we consider three channels as the final states of the dark matter annihilation. Assumed final states are $\bar{b}b$, W^+W^-, and $\tau^+\tau^-$. Those are representatives of dark matter annihilations into quarks, weak bosons, and leptons. The maximum mass of the dark matter particle in our calculation is set to $m_{\rm DM}$ = 1PeV. The maximum mass of the particle dark matter that meets the relic abundance could not exceed O(1)PeV from the unitarity limit [286]. The minimum is set to $m_{\rm DM}$ = 25GeV for lepton and quark channels and to $m_{\rm DM}$ = 160GeV for the weak boson channel. At lower energies, contributions from the residual cosmic-rays are significant. We set our minimum mass so that to avoid these contaminations.

The spectrum of each annihilation channel is calculated using `pythia8.2` [287–289]. Fig. 4.12 shows the example of the spectra from $m_{\rm DM}$ =100GeV to 1PeV. Spectra in Fig. 4.12 includes final state radiations such as bremsstrahlung of charged leptons, which are higher order effects different from the interactions with external fields. Contributions from the secondary γ-rays produced during propagations of charged leptons are negligible [290–294]. The spectra in Fig. 4.12 could not be directly compared with that of Fig. 4.8 since those are spectra before convolved with the IRF.

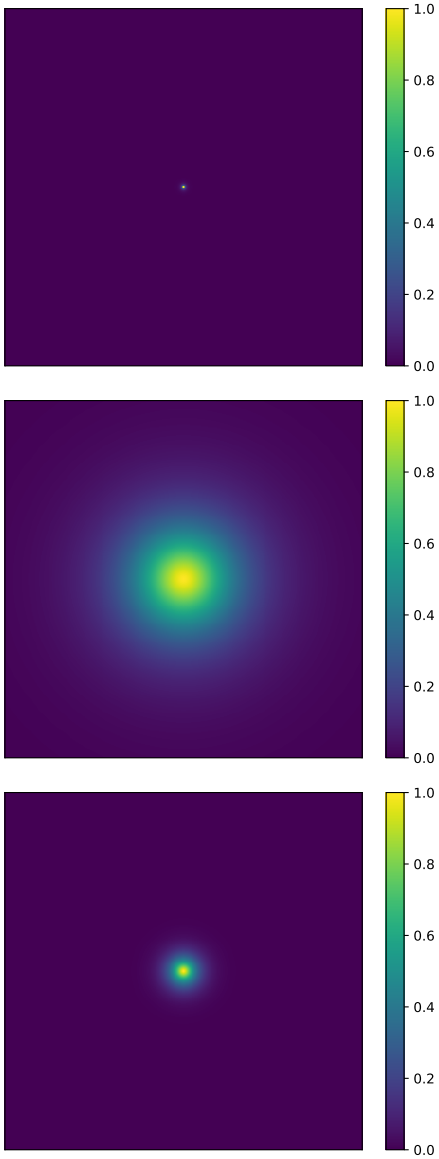

Figure 4.11: Relative J-factor maps correspond to the profile shown in Fig. 4.10. *Top*: NFW profile of model 5 in [271]. *Middle*: Burkert profile of model 1 in [271]. *Bottom*: (power-law of index 0) + cutoff profile in [272]. Each panel shows a $4° \times 4°$ region centered on the Draco. J-factors in each pixel is divided by the J-factor at the center pixel aiming to show the relative differenece.

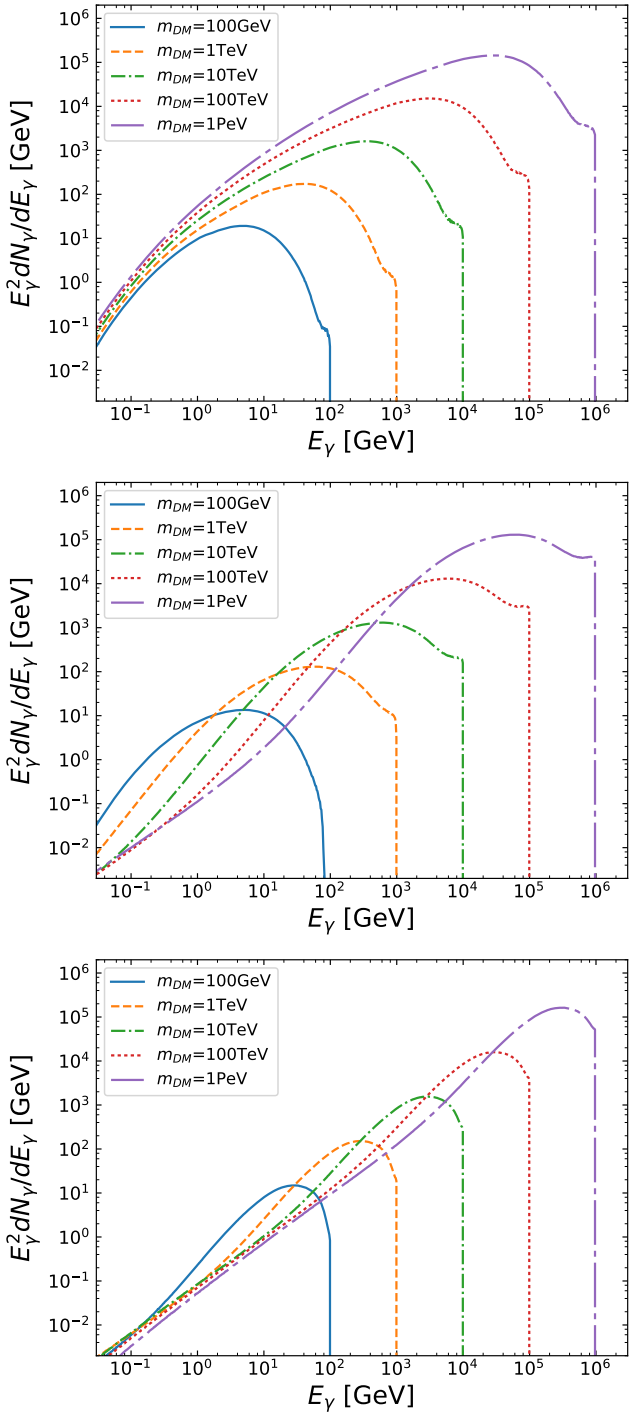

Figure 4.12: γ-ray spectrum for dark matter of mass $m_{\rm DM}$ =100GeV, 1TeV, 10TeV, 100TeV and 1PeV annihilating into $\bar{b}b$ (*top*), W^+W^- (*middle*) and $\tau^+\tau^-$ (*bottom*). Spectrum of $m_{\rm DM}$ = 100GeV annihilating into W^+W^- is shown for comparison and not used in our analyses.

4.4 Feasibility of detecting dark matter in dSphs

We derive 2σ confidence level upper limits on the γ-ray flux in the target dSph assuming a 500-hour observation with CTA. The density profiles listed in Table 4.1 and three annihilation channels, $\bar{b}b$, W^+W^-, and $\tau^+\tau^-$, are considered. Upper limits on the γ-ray flux are derived by binned maximum-likelihood analyses. We vary the normalizations of the model function in Eq. (4.3.5) and the background spectrum in our fitting procedure. Assumed background spectrum is shown in Fig. 4.8. The upper limit on the dark matter annihilation cross-section $\langle\sigma v\rangle$ is obtained by converting the upper limits on the γ-ray flux ϕ using

$$\phi = \frac{1}{4\pi}\frac{\langle\sigma v\rangle}{2m_{\rm DM}^2}\int_{E_{\rm th}}^{m_{\rm DM}} dE\frac{dN_\gamma}{dE}\cdot J \tag{4.4.1}$$

with

$$J = \int d\Omega\frac{dJ}{d\Omega} = \int d\Omega\int ds\,\rho_{\rm DM}^2. \tag{4.4.2}$$

To derive the γ-ray flux upper limits, we use Eq. (4.3.1) which adopts a Gaussian approximation. However, at higher energy regimes of $E_\gamma \gtrsim O(1)$ TeV, the number of the events in an energy bin decreases. If we include the fluctuations of $n_{{\rm obs},k}$ following the Poisson statistics in Eq. (4.3.2), the upper limits on the annihilation cross-section get milder by a few percents for dark matter of $m_{\rm DM} \gtrsim 10$ TeV.

In Fig. 4.13, we show the upper limits obtained by the analyses assuming each profile in Table 4.1. *Top*, *middle*, and *bottom* panel of the figure corresponds to the case of dark matter annihilating into $\bar{b}b$, W^+W^- and $\tau^+\tau^-$, respectively. We adopt the $J_{\rm tot}$ for each profile here. Each line corresponds to the case assuming a profile in Fig. 4.10 or Fig. 4.11. Dashed lines are the upper limits assuming profile No.14 (NFW model 5 of [271]) which is the strongest one in our sample, and solid lines are the case assuming No.16 (PL of index 0 + cutoff model in [272]), the weakest one. Upper limits obtained with other profiles lie in the shaded regions of Fig. 4.13, like dash-dotted lines corresponding to the profile No.7 (Burkert model 1 of [271]). Comparing the results for different annihilation channels, a wider region of the annihilation cross-section $\langle\sigma v\rangle$ can be probed for dark matter annihilating into $\tau^+\tau^-$ than those into $\bar{b}b$ or W^+W^-. A clearer feature in the annihilation spectrum (see *bottom* panel of Fig. 4.12) is the reason for the difference. The tendency is consistent with the latest results in [268], which assumes line+broad spectra of some specific WIMP models. The feature appearing on the sensitivity curves at $m_{\rm DM} = O(10) - O(100)$ TeV for dark matter annihilating into $\tau^+\tau^-$ results from the properties of the facility. In each channel of the dark matter annihilation, the best sensitivity is achieved for the dark matter of $m_{\rm DM}$ =1TeV, 630GeV, and 250GeV for $\bar{b}b$, W^+W^-, and $\tau^+\tau^-$, respectively. These are universal among the profiles.

In Fig. 4.13, the effect coming from the different J-factors and the profile shapes degenerate. As a result, a weaker dependence than the relation $\langle\sigma v\rangle \propto J_{\rm tot}^{-1}$ expected from Eq. (4.4.1) for

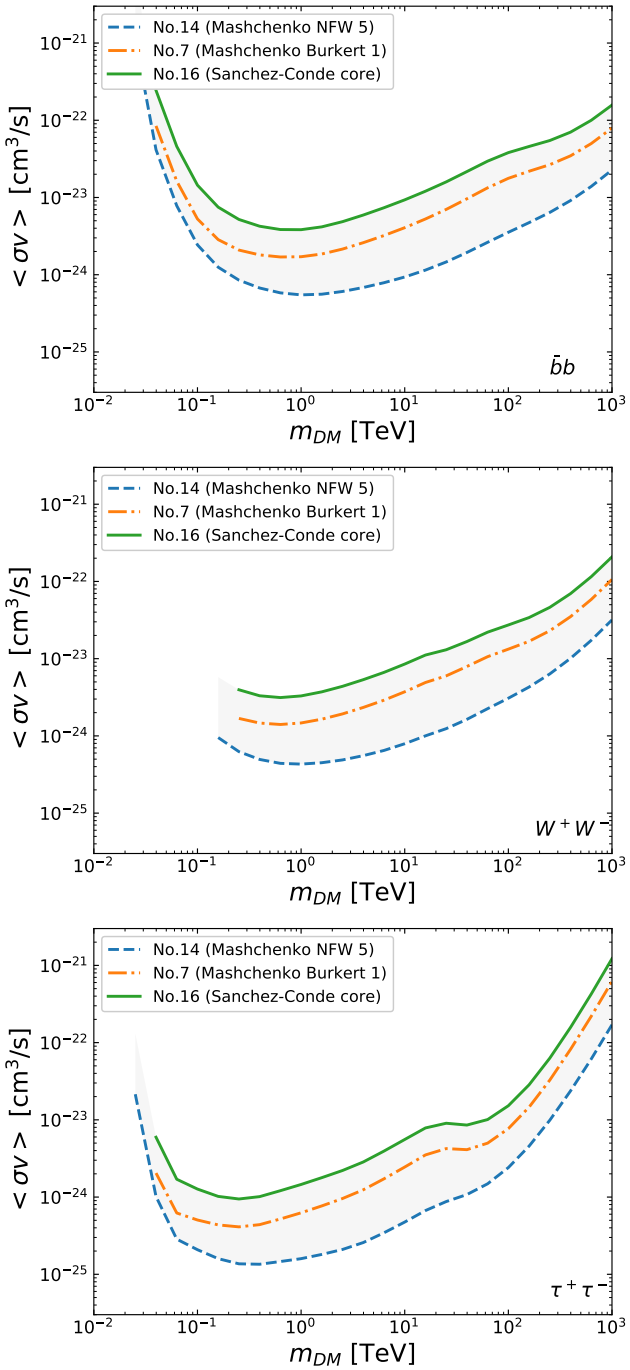

Figure 4.13: The sensitivity calculated with the profiles listed in Table 4.1, assuming a 500-hour observation with CTA. *Top*, *middle* and *bottom* panel corresponds to the upper limits on dark matter annihilation cross-sections into $\bar{b}b$, W^+W^- and $\tau^+\tau^-$, respectively. In each panel, we show the severest upper limits assuming a NFW profile of $J_{\rm tot} = 10^{19.15}$ (*top* panel in Fig. 4.10) with a dashed-line and the weakest one assuming a (PL of index 0)+cutoff profile of $J_{\rm tot} = 10^{18.58}$ (*bottom* in Fig. 4.10) with a solid line. The upper limits obtained with all other profiles are in the shaded region between two lines. The dot-dashed line corresponds to the *middle* panel in Fig. 4.10 of $J_{\rm tot} = 10^{19.56}$ is an example. Numbers in the legend correspond to those in Table 4.1. The difference between the lines is determined by the value of the J-factor and the profile shape.

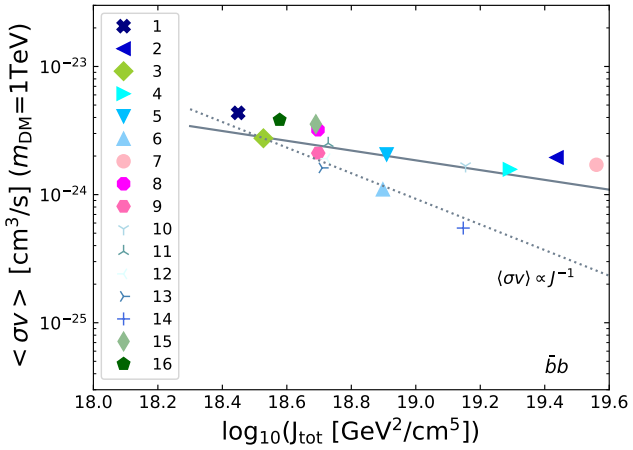

Figure 4.14: The obtained upper limits on the annihilation cross-section $\langle\sigma v\rangle$ as a function of the J-factor ($J_{\rm tot}$). The value of the cross-section is taken as that for $m_{\rm DM}$=1TeV annihilating into $\bar{b}b$. The mass at the best-sensitivity does not depend on the profile. The J-factor dependence fitted for these samples is shown with a solid line. We also show a relation $\langle\sigma v\rangle \propto J^{-1}$ with a dotted line for comparison.

point sources are found. This is shown in Fig. 4.14. In Fig. 4.14, we plot the upper limits on the annihilation cross-section into $\bar{b}b$ at $m_{\rm DM}$ = 1TeV, which is the most constraining point for this annihilation channel, as a function of the J-factor ($J_{\rm tot}$). Each point corresponds to the profile in Table 4.1. The dotted black line shows the relation $\langle\sigma v\rangle \propto J^{-1}$ and this is steeper than our results. A fitted relation with our data is shown with the solid line. The similar behavior is seen for dark matter annihilating into W^+W^- or $\tau^+\tau^-$. By defining the rank of the profiles with the upper limits of the annihilation cross-section at the best constraining points, we examine the relationship between the final state and the profile. There is no change in ranks of profiles between different channels. The profile No.14 in Table 4.1 is the strongest, No.16 is the weakest, and all other profiles lie between them in the same order.

In order to solve the degeneracy between the J-factor and the profile shape in Fig. 4.13, we calculate upper limits assuming the same J-factor for all the profile in Table 4.1. In Fig. 4.15, we show the re-scaled upper limits adopting the most optimistic (left) and conservative (right) J-factor, $\log_{10} J$ = 19.56 and $\log_{10} J$ = 18.45. Upper limits assuming a point source of the same J-factors are also shown with dotted-black lines. If we assume that the target dSph is a point source, the annihilation cross-section is overly constrained. These results that a point source gives a stronger upper limit compared to an extended one are consistent with that obtained in the analytical discussions [267]. The gap width in the sensitivity curve between a point source and an extended source depends on the shape of the profile. For

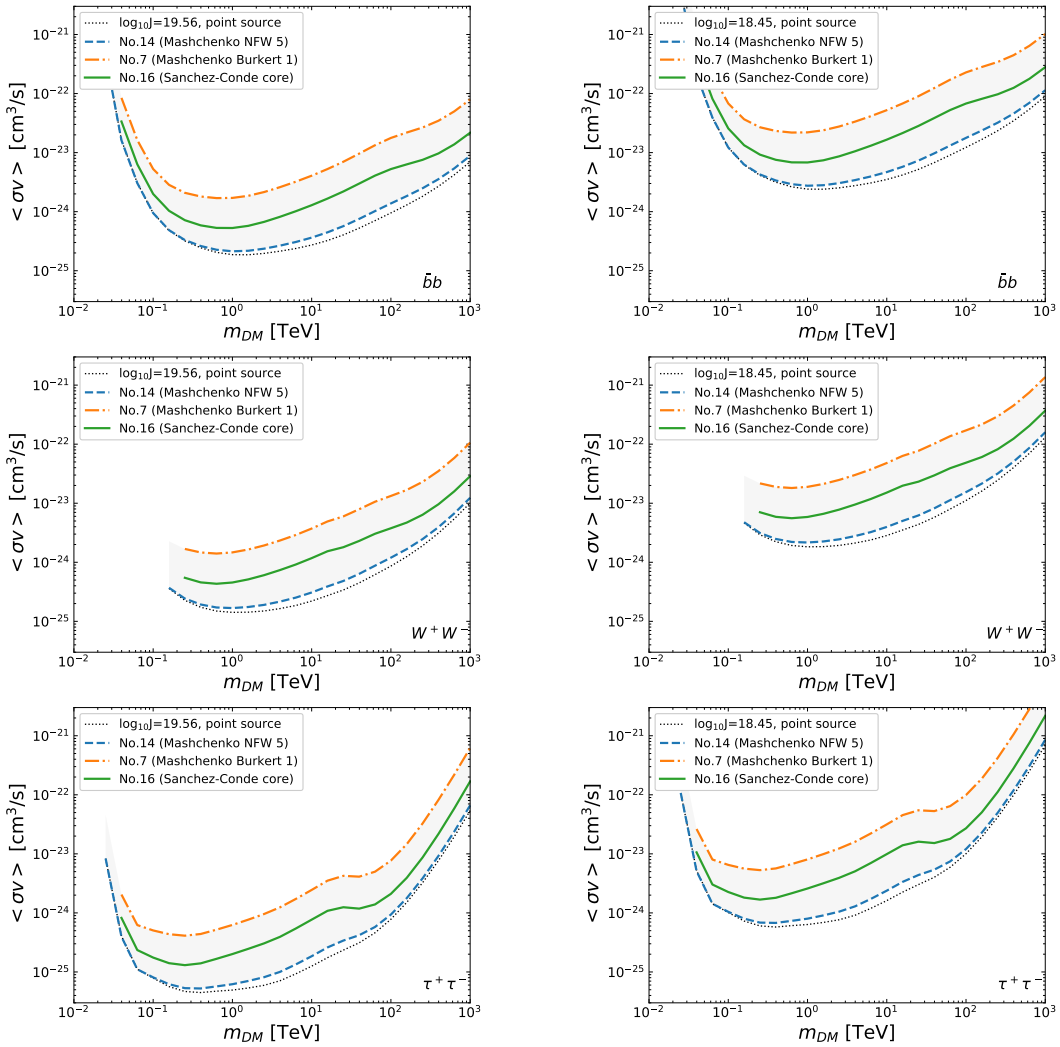

Figure 4.15: The same as Fig. 4.13, but all the upper limits are rescaled with the most optimistic J-factor of $\log_{10} J = 19.56$ (*left*) and the conservative J-factor of $\log_{10} J = 18.45$ (*right*) derived for profiles in Table 4.1. We also add lines assuming a point source of the same J-factor in each panel. By assuming a point source, the annihilation cross-sections are overly constrained. The width of the gap between the limits assuming a point source and an extended source depends on the spatial extension of the profile.

example, the limits obtained with the profile No.7 is milder than that of the profile No.16 when we adopt the same J-factor for these profiles. As shown in Figs. 4.10 and 4.11, they are different in spatial extensions. This is different from the results in Fig. 4.13 which includes the difference of the J-factor. The shape of the target dSph could affect the sensitivity as much as that of the J-factor.

4.5 Discussions

We showed that the accessible parameter region of the dark matter annihilation cross-section depends on the density profile of dSphs. The density profile affects the accessible region in two ways. As is already known, it directly affects the detectability by changing the value of the J-factor. We point out another dependence on the spatial extension of the source. In Fig. 4.15, we show the achievable upper limits on the dark matter annihilation cross-section assuming different profiles of dSphs having the same J-factor. Compared to the limits assuming a point source, it gets milder when we assume extended sources. The difference from the point-source case depends on the profile shape.

We introduce a new quantity θ_{90} to characterize the spatial extension of the source. θ_{90} is defined as the 90% containment radius of the J-factor:

$$J_{\theta_{90}} = 2\pi \int^{\theta_{90}} d\theta \sin\theta \int_{l.o.s} ds \rho^2_{\rm DM} = 0.9 \times J_{\rm tot}. \tag{4.5.1}$$

The value of the θ_{90} is shown in Table 4.1. In Fig. 4.16, we show the ratio of the obtained upper limits assuming an extended source and a point source, $\langle\sigma v\rangle_{\rm extended} / \langle\sigma v\rangle_{\rm point}$, as a function of θ_{90}. We use a different marker for a different mass of dark matter. By taking the ratio, the effect of the J-factor on the upper limit is canceled. The ratio tends to get larger for more extended profiles. In the most extended profile in our sample (No.7), the upper limits are milder than by a factor of ~ 10 compared to the limits assuming a point source of the same J-factor. Scatters in the relation between the ratio $\langle\sigma v\rangle_{\rm extended} / \langle\sigma v\rangle_{\rm point}$ for a given θ_{90} are also seen in Fig. 4.16. The slope of the density profile at the inner region of the dSph, e.g. γ in Eq. (4.3.7), is responsible for this feature. For a shallower slope of dSph, the upper limit gets milder than that have a steeper slope if we compare at the same θ_{90} value.

In Fig. 4.17, we show the ratio of the upper limits obtained by assuming the most- and the least-constraining profiles after removing the J-factor dependence. The effect coming from the different J-factor is removed by taking the ratio of $\langle\sigma v\rangle J$. For each annihilation channel, the ratio is about a factor of ~10 and depends on the dark matter mass. A broad bump of the ratio at around $m_{\rm DM}$ ~1 - 500 TeV is seen in the case of $\bar{b}b$, while a bump at the lower mass of $m_{\rm DM} \lesssim 20$TeV appears in the ratio for $\tau^+\tau^-$. For W^+W^-, a broad bump ranges from $m_{\rm DM} \sim O(1-100)$ TeV. The dark matter mass at around the bump corresponds to the γ-ray

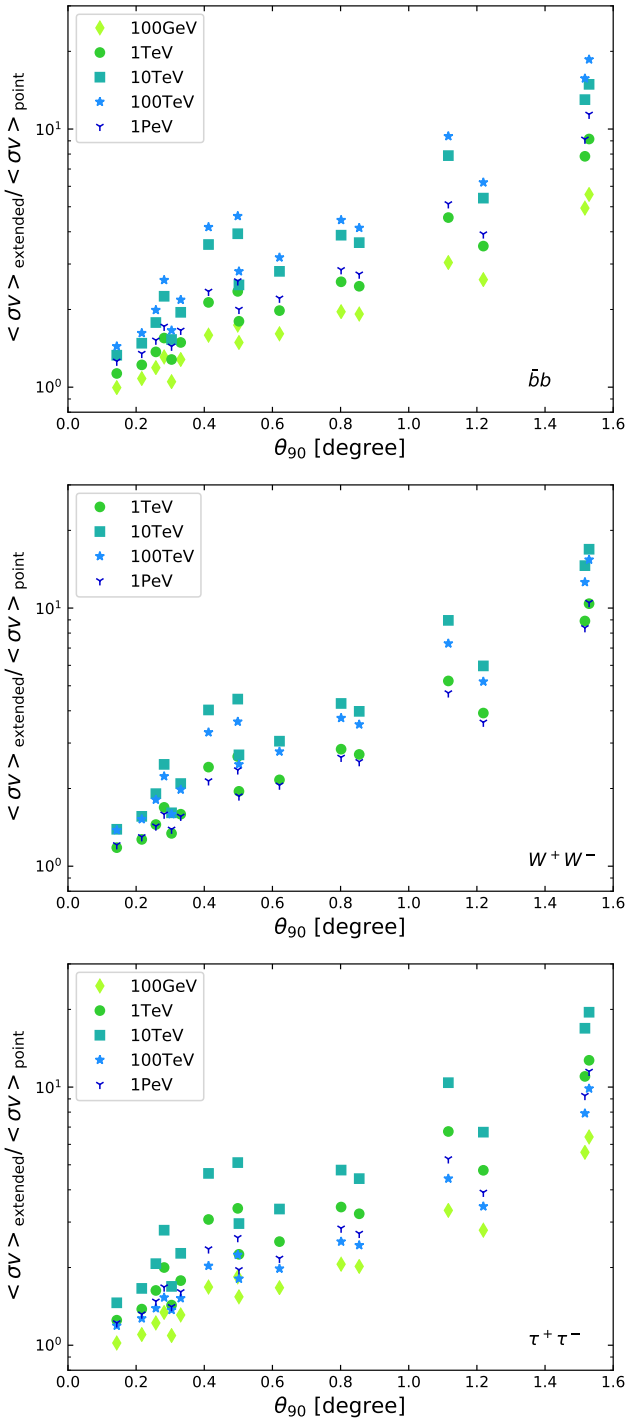

Figure 4.16: The ratio of the upper limits assuming an extended source $\langle \sigma v \rangle_{\text{extended}}$ and a point source $\langle \sigma v \rangle_{\text{point}}$ as a function of the source extension θ_{90}. The value of the θ_{90} is shown in Table 4.1. The limit on the annihilation cross-section $\langle \sigma v \rangle$ is calculated assuming a same J-factor. *Top*, *middle*, and *bottom* panel corresponds to the case of dark matter annihilating into $\bar{b}b$, W^+W^-, and $\tau^+\tau^-$, respectively. In each panel, the difference of the marker corresponds to the difference of the dark matter mass m_{DM}.

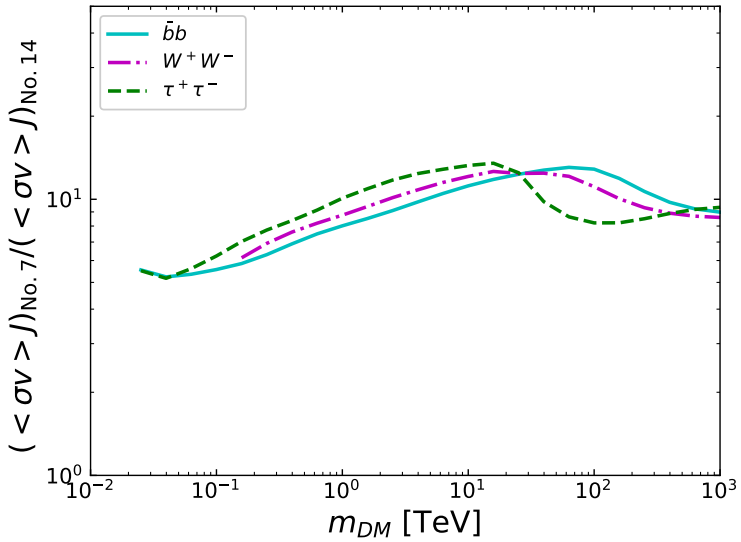

Figure 4.17: The ratios of the upper limits on the annihilation cross-sections obtained with profile No.7 and No.14 in Table 4.1 after removing the effect originates from the J-factor. The horizontal axis is the mass of the dark matter m_{DM} and the vertical axis is the ratio $(\langle\sigma v\rangle J)_{\mathrm{No.7}}/(\langle\sigma v\rangle J)_{\mathrm{No.14}}$. Solid, dot-dashed and dashed lines correspond to the case of the dark matter annihilating into $\bar{b}b$, W^+W^- and $\tau^+\tau^-$, respectively. The mass dependence of the ratio is understood with the characteristics of the facilities.

energy $E_\gamma \sim 10$TeV (see Fig. 4.12). The presence of the bumps can be interpreted as follows. The angular resolution of the CTA facility gets better as the γ-ray energy increases. For example, it corresponds to about $\Delta\theta \sim 0.1$ degrees at $E_\gamma \sim 200$ GeV and improves to about ~0.04 degrees at ~10 TeV [229]. Therefore, the changes in the flux upper limits are more significant at higher energies. On the other hand, at the very-high-energy regime of $E_\gamma > 10$ TeV, almost no residual background events are expected. In such a case, the sensitivity is more determined by the detection number of the signal event rather than the signal-to-noise ratio. It is a so-called "signal-dominant case". In such cases, the angular resolution has fewer contributions to the γ-ray flux upper limits. Then they are less affected by the spatial extensions of sources, and the upper limits with the most-extended profile in our sample, profile No.7, can get close to the expected values for those of point sources. The behaviour of the ratio $(\langle\sigma v\rangle J)_{No.7}/(\langle\sigma v\rangle J)_{No.14}$ is a manifestation of these effects since the profile No.14 almost corresponds to a point source. Combining those two effects, the ratio between the profiles has the bump structures seen in Fig. 4.17.

4.6 Summary

We investigated how the density profile of the target dSphs affect the feasibility of detecting dark matter with CTA. The density profile of dSph is an actively debated topic. Taking Draco dSph as an example, we collected 16 models of the density profile and tested the sensitivity with each profile using a simulated 500-hour data of observations with CTA. The accessible value of the annihilation cross-section differs by a factor of ∼10 and the annihilation cross-section of $\langle\sigma v\rangle \lesssim 10^{-23}\mathrm{cm}^3/s$ can be probed when we simply adopt the profiles from the literature. The change of the J-factor and the profile shape are the sources of the difference in the accessibilities. We performed further analyses assuming different profiles of dSphs with the same J-factor to extract the dependence on the profile shape. Our results revealed that the spatial extension of the target dSph could affect the sensitivity in a different way from that of the J-factor. To quantify the spatial extension of the profile with different modelings, we introduce a new quantity θ_{90} defined to be the 90% containment radius of the J-factor. When θ_{90} is larger than ∼1 degree, the upper limits on the annihilation cross-section shift upwards by a factor of ∼10 compared to the case analyzing a point source of the same J-factor. With either of the most optimistic or conservative assumptions of the density profile, we can detect the dark matter signal of which annihilation cross-section is larger than $\langle\sigma v\rangle \sim O(10^{-25} - 10^{-23})$ cm^3/s hence we can search the unexplored parameter regions for WIMP dark matter of $m_{\mathrm{DM}} \gtrsim O(1)$ TeV. Some of the well-motivated models which expect resonant annihilations (e.g. [75]) can be tested by observing dSphs with CTA. The upper limits expected in this work is still higher than the canonical cross-section. With the latest profiles based on more detailed modelings (e.g. [251, 283–285]), a wider regions of the parameter space could be probed. In such cases, our results can be regarded as conservative benchmarks.

Chapter 5

Subhalo boost of the dark matter annihilation signal

In Chapter 4, we consider the dark matter search in dwarf spheroidal galaxies with Cherenkov Telescope Array. Our results indicate that a factor of ~ 10 uncertainty remains with the current understanding of the dark matter density profile of dwarf spheroidal galaxies. In this chapter, we study about another source of the uncertainty in our targets, the *boost factor*. Dark matter forms gravitationally bounded objects called halos in the Universe with which we search for the dark matter signal. The structure of the halo is hierarchical and smaller structures (*subhalos*) could exist in the target halo. We can parametrize the possible enhancement of the dark matter annihilation signal caused by subhalos on our lines-of-sight with the boost factor.

We have to know the halo structures after their cosmological evolutions to quantify the subhalo boost. The N-body simulation is a traditional way to study the halo structure. Boost factors are well-quantified in the halo mass and the redshift ranges covered by simulations. However, calculations of boost factors require much wider range than those available with N-body calculations, from the minimum halo mass of $\sim 10^{-6} M_\odot$ to the galaxy cluster scale of $\sim 10^{16} M_\odot$ and redshift up to 10. In previous works estimating the boost factor, huge uncertainties are induced when one adopts the extrapolation of the N-body results in the last steps of the calculation for the boost factor. We need wide-coverage calculations to reduce this uncertainty. In this work, we develop a new analytical method to calculate subhalo evolutions covering more than 20 orders in the mass scale and redshift $z = 0$ to ~ 10. Our formulation is physically motivated and the results are consistent with those obtained in corresponding N-body calculations. We show that a factor of ~ 10 enhancement of the annihilation signal is expected in galaxy clusters when we count the contributions from subhalos down to the minimum mass scale. On the other hand, the boost could not be expected in the halos of the dwarf spheroidal galaxy scale.

The contents of this chapter are based a collaboration work with Dr. Shin'ichiro Ando and Dr. Tomoaki Ishiyama [295]. N-body calculations with which we compare our analytical results are conducted by Dr. Ishiyama. Applications of our subhalo boost to the isotropic γ-ray background constraints are provided by Dr. Ando. The author of the thesis is responsible for all the remaining parts and calculations in this chapter. In Sec. 5.1, we introduce the original motivation for subhalo boosts. Our modelings and the calculation methods are explained in Sec. 5.2 and Sec. 5.3. Results and discussions are in Sec. 5.4 and Sec. 5.5. We conclude in Sec. 5.6.

5.1 Subhalo and the boost factor

Dark matter halo (hereafter halo) is a virialized object of dark matter. Study of the dark matter halo provide insights into the properties of dark matter. For example, the minimum mass of the halo encodes the interaction strength to the standard model particles in the early Universe. If they are supersymmetric neutralino, the minimum mass of the halo should be in the range of 10^{-12}–$10^{-3}M_\odot$ [56–59] depending on the details of the models. Also, the density profile of dark matter halo depends on the particle property (e.g. [79, 296]). The seed of the halo in the current Universe is produced by the collapse of the initial density fluctuation. After the formation, they get larger by accretions and mergers. The hierarchical structure of the halos in the current Universe is the outcome of such processes. We focus on the *subhalo*, the smaller halo in larger halos (hereafter *host halos*) in this study. Tidal stripping is an important process to determine the subhalo property. After their accretion onto the hosts, they lose parts of their mass through the gravitational interaction while they are orbiting around their hosts. The structures of subhalos change significantly in this process. Tidal stripping of the subhalo is studied using the analytical [297–299], semi-analytical [300], and numerical [301–306] methods.

The existence of the subhalo is natural in the WIMP scenario and we should consider their contributions the indirect dark matter search [249, 307–311]. In order to quantify their contributions in the present-day halos, one has to model the subhalo properties after tidal stripping. N-body simulations are traditional and powerful tools to study the hierarchal structure including the tidal stripping of subhalos. However, subhalos are so small and could not be fully-resolved in N-body simulations. We need to resolve the minimum-mass halo of $M \sim 10^{-6}M_\odot$ in the galaxy cluster scale halo of $M \sim 10^{16}M_\odot$ to calculate the boost factor. This is beyond the scope of the N-body simulation. Then extrapolations of the results with N-body calculations in a limited mass and redshift ranges have been adopted. Fig. 5.1 shows an example in [312]. The value of the boost factor is sensitive to the slope of the subhalo mass function α, which is defined as $dN_{\rm sh}/dm \propto m^{-\alpha}$. $N_{\rm sh}$ and m are the number and the mass of the subhalo. If we change the slope α from 1.9 to 2.0, the boost factor can differ

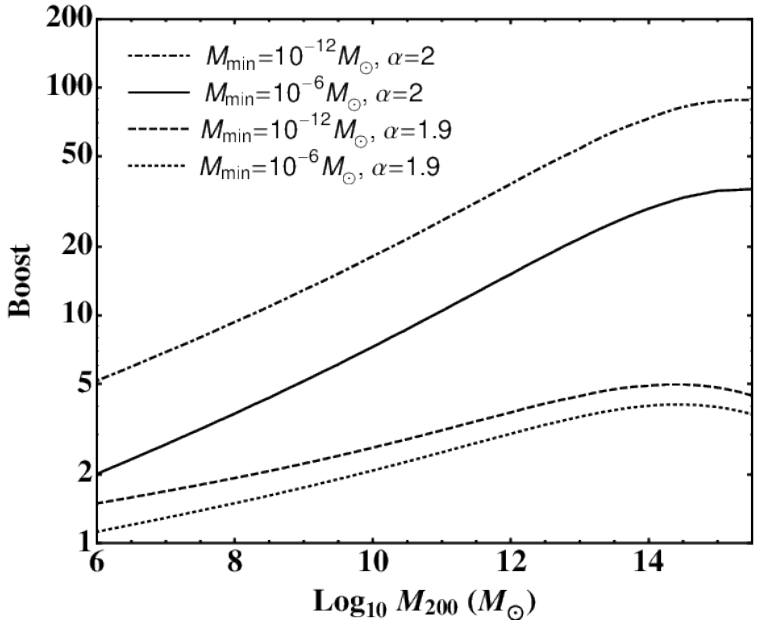

Figure 5.1: An example of the boost factor calculated in [312]. Four lines in the figure are different in the slope of the subhalo mass function α and the minimum halo mass. The value of the boost factor differs by more than one order-of-magnitude depending on the models of extrapolations. In this figure, the boost factor $B(M_{\rm host})$ is defined as $B(M_{\rm host}) = \left[\int_{m_{\rm min}}^{M_{\rm host}} dm(1+B(m))L(m)dN/dm\right]/L(M_{\rm host})$. The luminosity of the dark matter annihilations signal is denoted with L.

by more than one order-of-magnitude.

By adopting analytical approaches, we can avoid the problem caused by extrapolations. We decompose the calculation in three parts to derive the boost factor in an analytical way:

1. Evolution of the host halo including the accretion history of subhalos
2. Tidal stripping of subhalos after accretion
3. Calculations of the boost factor by remaining subhalo structures

We adopt an extended Press-Schechter theory for the evolution of the host halo [313] and also for the subhalo accretion history [314]. For the calculation of the tidal stripping, we follow the prescription in [299]. This is an analytical description of the tidal stripping which simplifies the phenomena based on physical considerations. The tidal mass-loss of the

subhalo is parametrized as [299]

$$\dot{m}(z) = -A\frac{m(z)}{\tau_{\rm dyn}(z)}\left[\frac{m(z)}{M(z)}\right]^{\zeta}, \tag{5.1.1}$$

where $\tau_{\rm dyn}(z)$ is the dynamical timescale. The host mass is denoted as $M(z)$. The evolution of the host is separately determined using the relation in [313] (see Sec. 5.3.1 for details). We update the model in [299] by including the redshift and host-mass dependence of the parameters A and ζ. Then the boost factor is calculated using the derived subhalo properties after tidal stripping. Throughout the calculation in this chapter, we assume that the NFW profile up to the truncation radius for both of the host and subhalo.

5.2 Density profile of suhalos

So-called NFW profile [281] is the simplest profile for dark matter halos characterized with two parameters: the characteristic density ρ_s and the scale radius r_s. In this work, we assume that both of the host and subhalos are described with this profile up to the truncation radius r_t. The expression is

$$\rho(r) = \begin{cases} \rho_s r_s^3/[r(r+r_s)^2], & \text{for} \quad r \le r_t, \\ 0, & \text{for} \quad r > r_t. \end{cases} \tag{5.2.1}$$

For calculations of the boost factor, we need $\rho_{s,0}$, $r_{s,0}$, and $r_{t,0}$ after tidal stripping. In this section, we explain how to determine these parameters starting from the initial halo properties.

First, we determine the initial density profile of the subhalo at the accretion redshift $z_{\rm acc}$ in the following way. Assuming that the progenitor of a subhalo is a field halo (i.e., a halo that is not in the gravitational potential of a larger halo), the virial radius $r_{\rm vir,acc}$ for a given mass of the subhalo $m_{\rm acc}$ at the accretion redshift $z_{\rm acc}$ is determined as

$$m_{\rm acc} = \frac{4\pi}{3}\Delta_c(z_a)\rho_c(z_{\rm acc})r_{\rm vir,acc}^3, \tag{5.2.2}$$

where

$$\Delta_c = 18\pi^2 + 82d - 39d^2 \tag{5.2.3}$$

$$d = \frac{\Omega_m(1+z_{\rm acc})^3}{[\Omega_m(1+z_{\rm acc})^3 + \Omega_\Lambda]} - 1 \tag{5.2.4}$$

[315]. $\rho_c(z_{\rm acc})$ is the critical density at the accretion redshift. The virial radius $r_{\rm vir}$ and the scale radius r_s is related with the concentration parameter $c_{\rm vir}$ as $r_{s,\rm acc} = r_{\rm vir,acc}/c_{\rm vir,acc}$. For the concentration parameter $c_{\rm vir,acc}$, we adopt the mean value of the model in [316]. The

details are explained in Sec. 5.3.1. The concentration parameter is given as c_{200} in [316]which corresponds to the halo mass measured in M_{200}. M_{200} is defined as the enclosed mass in a radius within which the average density is 200 times the critical density. We convert c_{200} to $c_{\rm vir}$ which corresponds to a different definition of the halo mass [317] using the relation $c_{\rm vir,acc} = c_{200,\rm acc} r_{\rm vir,acc}/r_{200,\rm acc}$. In our calculation, we include the scatter of the concentration parameter assuming a log-normal distributions. The root mean square of the log-normal distribution is taken from from [318] that

$$\sigma_{\log c} = 0.13. \tag{5.2.5}$$

Using above quantities, we can derive the characteristic density $\rho_{s,\rm acc}$ of the NFW profile as

$$\rho_{s,\rm acc} = \frac{m_{\rm acc}}{4\pi r_{s,\rm acc}^3 f(c_{\rm vir,acc})}, \tag{5.2.6}$$

where

$$f(c) = \ln(1+c) - \frac{c}{1+c}. \tag{5.2.7}$$

Hence the profile parameter at the accretion redshift is determined once we fix the accretion redshift $z_{\rm acc}$ and the accretion mass $m_{\rm acc}$. The set of the profile parameter $(\rho_{s,\rm acc}, r_{s,\rm acc})$ has one-to-one correspondence to the set of the maximum circular velocity and the corresponding radius, $(V_{\rm max}, r_{\rm max})$. For a halo of NFW profile, the relations are

$$r_{\rm max} = 2.163 r_s \tag{5.2.8}$$

$$V_{\rm max} = r_s \sqrt{\frac{4\pi G \rho_s}{4.625}}. \tag{5.2.9}$$

Next, we derive the profile parameter after tidal stripping using the relation derived in [319]. The relation between the $(V_{\rm max}, r_{\rm max})$ at the accretion redshift $z_{\rm acc}$ and those at the arbitrarily chosen observation redshift z_0 is given as a function of the mass ratio after and before tidal stripping $m_0/m_{\rm acc}$. If the density profile follows the r^{-1} distribution, which corresponds to the NFW profile, the relations are

$$\frac{V_{\rm max,0}}{V_{\rm max,acc}} = \frac{2^{0.4}(m_0/m_{\rm acc})^{0.3}}{(1+m_0/m_{\rm acc})^{0.4}}, \tag{5.2.10}$$

$$\frac{r_{\rm max,0}}{r_{\rm max,acc}} = \frac{2^{-0.3}(m_0/m_{\rm acc})^{0.4}}{(1+m_0/m_{\rm acc})^{-0.3}}. \tag{5.2.11}$$

Using these relations, Eqs. (5.2.8), and (5.2.9), we can describe the profile parameter after tidal stripping with the ratio of the subhalo mass before and after the tidal stripping, $m_0/m_{\rm acc}$. The subhalo mass after tidal stripping m_0 is calculated by solving Eq. (5.1.1).

Finally, the truncation radius $r_{t,0}$ is determined from m_0, $\rho_{s,0}$, and $r_{s,0}$ by solving the equation

$$m_0 = 4\pi\rho_{s,0}r_{s,0}^3 f\left(\frac{r_{t,0}}{r_{s,0}}\right). \tag{5.2.12}$$

We put an additional condition $r_{t,0}/r_{s,0} \geq 0.77$ to remove the disrupted subhalos [320]. There is a claim that the disruption of the subhalo is a numerical artifact [306]. Our treatment is conservative in estimating the boost factor.

5.3 Tidal stripping

The evolution of the subhalo is determined by the tidal force they feel under the potential of their hosts. Then the subhalo mass-loss rate $\dot{m}$ in Eq. (5.1.1) should depend on both the redshift z and the host mass $M(z)$. In this section, we explain our formulations and derive the function $A(M_{\rm host}, z)$ and $\zeta(M_{\rm host}, z)$ following the prescription in [299]. In order to calculate in an analytical way, we assume that the tidal mass-loss of the subhalo occurs in one complete orbital period. We also assume that there are no lags between the subhalo accretion and the tidal stripping. We show the validity of this analytical treatment by comparing the results with those obtained in numerical simulations.

5.3.1 evolution of the host halo

In order to calculate the evolution of the subhalo, we first specify the evolution of the host halo. We adopt the relation about the host mass M_0 at redshift $z = 0$ and the host mass $M(z)$ at an arbitrary redshift z, $M(z|M_0, z = 0)$, derived in [313]. Following relations are assumed in our calculation:

$$M(z|M_0, z = 0) = M_0(1 + z)^\alpha \exp(\beta z), \tag{5.3.1}$$

with

$$\begin{aligned}
\beta &= -g(M_0), && (5.3.2)\\
\alpha &= \left[\frac{1.686\sqrt{2/\pi}}{D^2(z=0)}\left.\frac{dD}{dz}\right|_{z=0} + 1\right] g(M_0), && (5.3.3)\\
g(M_0) &= \left[S(M_0/q) - S(M_0)\right]^{-1/2}, && (5.3.4)\\
q &= 4.137\tilde{z}_f^{-0.9476}, && (5.3.5)\\
\tilde{z}_f &= -0.0064(\log M_0)^2 + 0.0237(\log M_0) \\
&\quad +1.8837, && (5.3.6)
\end{aligned}$$

where $D(z)$ and $S(M) \equiv \sigma^2(M)$ are the growth function and the variance of the matter distribution at the mass scale M and redshift $z = 0$, respectively. We adopt the fitting functions for $D(z)$ and $\sigma(M)$ in [321]. Eq. (5.3.1) is generalized to determine the mass of the halo $M(z|M(z_i), z_i)$ at redshift z, whose mass was $M(z_i)$ at redshift z_i [316]:

$$M(z|M(z_i), z_i) = M(z_i)(1 + z - z_i)^{\alpha} \exp(\beta(z - z_i)), \tag{5.3.7}$$

with replacing M_0 with $M(z_i)$ in Eqs. (5.3.2), (5.3.3), and (5.3.4). These relations enable us to follow back the evolutions of the hosts starting from arbitrary redshifts.

Corresponding to the above-mentioned host evolution, the concentration-mass relation is also derived in [316]. In terms of c_{200} and M_{200}, the relation for the field halo is

$$\log c_{200} = \alpha + \beta \log\left(\frac{M_{200}}{M_\odot}\right)\left[1 + \gamma \log^2\left(\frac{M_{200}}{M_\odot}\right)\right], \tag{5.3.8}$$

where

$$\alpha = 1.7543 - 0.2766(1 + z) + 0.02039(1 + z)^2, \tag{5.3.9}$$

$$\beta = 0.2753 + 0.00351(1 + z) - 0.3038(1 + z)^{0.0269}, \tag{5.3.10}$$

$$\gamma = -0.01537 + 0.02102(1 + z)^{-0.1475}, \tag{5.3.11}$$

for $z \leq 4$. For $z > 4$,

$$\log c_{200} = \alpha + \beta \log\left(\frac{M_{200}}{M_\odot}\right), \tag{5.3.12}$$

with

$$\alpha = 1.3081 - 0.1078(1 + z) + 0.00398(1 + z)^2, \tag{5.3.13}$$

$$\beta = 0.0223 - 0.0944(1 + z)^{-0.3907}. \tag{5.3.14}$$

and $\gamma = 0$. Note that the parameter α, β, γ is different from those used in the previous chapter. We only use these expressions in this subsection. In the derivation of the above values, the Planck cosmology [322] is assumed. The scatter of the concentration in Eq. (5.2.5) is also included in the following calculations. Throughout this thesis, these relations are implicitly assumed.

5.3.2 analytical model

In our analytical formulations, the mass-loss rate $\dot{m}(z)$ of the left-hand side of Eq. (5.1.1), is approximated as

$$\dot{m} = \frac{m - m(r_t)}{T_r}, \tag{5.3.15}$$

where T_r and m are the orbital period and the virial mass of the subhalo just after the accretion. The mass enclosed in the tidal truncation radius r_t of the subhalo is denoted as $m(r_t)$. The orbital period T_r and the truncation radius r_t is determined by classical dynamics once the orbit of the subhalo is fixed. The orbit of the subhalo is characterized with the circularity η and the radius of the circular orbit R_c. These parameters correspond to the total energy E and the angular momentum L of the orbital motion as shown in below. We assume the following distributions for the parameter R_c and η:

$$P(R_c) = \begin{cases} 5/2 & (0.6 \leq R_c/R_{\rm vir} \leq 1.0), \\ 0 & (\text{otherwise}), \end{cases} \tag{5.3.16}$$

$$P(\eta) = C_0(M,z)\eta^{1.05}(1-\eta)^{C_1(M,z)}, \tag{5.3.17}$$

where

$$C_0 = 3.38\left(1 + 0.567\left[\frac{M}{M_*(z)}\right]^{0.152}\right), \tag{5.3.18}$$

$$C_1 = 0.242\left(1 + 2.36\left[\frac{M}{M_*(z)}\right]^{0.107}\right), \tag{5.3.19}$$

$$\log\left[\frac{M_*(z)}{h^{-1}M_\odot}\right] = 12.42 - 1.56z + 0.038z^2. \tag{5.3.20}$$

We note that Eqs. (5.3.17)–(5.3.20) are calibrated with simulations up to the redshift $z = 7$ [323]. The parameters R_c and η relates to the energy E and the angular momentum L of the subhalo orbit as

$$E = \frac{1}{2}V_c^2 + \Phi(R_c), \tag{5.3.21}$$

$$L = \eta R_c V_c. \tag{5.3.22}$$

$V_c = (GM/R_c)^{1/2}$ denotes the circular velocity of the orbit. The gravitational potential of the host Φ is

$$\Phi(R) = -V_{\rm vir}^2 \frac{\ln[1 + c_{\rm vir}^{\rm host} R/R_{\rm vir}]}{f(c_{\rm vir}^{\rm host})R/R_{\rm vir}}, \tag{5.3.23}$$

where $V_{\rm vir} = (GM/R_{\rm vir})^{1/2}$ and $c_{\rm vir}^{\rm host}$ the host halo's virial velocity and virial concentration, respectively. The concentration parameter for the host $c_{\rm vir}^{\rm host}$ is drawn from the log-normal distribution as discussed in the previous section.

The orbital period T_r and the truncation radius of the subhalo, r_t is numerically obtained by solving the equations below. The pericenter R_p and the apocenter R_a of a given subhalo orbit are determined by solving

$$\frac{1}{R^2} + \frac{2[\Phi(R) - E]}{L^2} = 0, \tag{5.3.24}$$

then the orbital period T_r is obtained as

$$T_r = 2\int_{R_p}^{R_a} \frac{dR}{\sqrt{2[E - \Phi(R)] - L^2/R^2}}. \tag{5.3.25}$$

The truncation radius r_t is determined by solving another equation

$$r_t = R_p \left[\frac{m(r_t)/M(< R_p)}{2 + \frac{L^2}{R_p GM(<R_p)} - \frac{d\ln M}{d\ln R}\Big|_{R_p}} \right]^{\frac{1}{3}}. \tag{5.3.26}$$

Assuming that ρ_s and r_s hardly change as the result of one complete orbit after the infall, we specify the mass profile $m(r)$ up to truncation radius r_t. Then the mass-loss rate $\dot{m}$ is determined using Eq. (5.3.15). Note that the (un)change of the profile parameter ρ_s and r_s is a simplification to capture the most relevant physics of tidal mass loss in our analytical modeling. For example in [319], ρ_s and r_s change in one orbit by $\lesssim 50\%$. However, the change of ρ_s and r_s can be compensated by the change of the truncation radius r_t. As we show in below, our results show good agreements with those of N-body simulations under these simplifications.

5.3.3 numerical simulations

We have also calculated the tidal stripping of subhalos using N-body simulations. To cover a wide range of halo mass, we use five large cosmological N-body simulations. The details of the simulation are summarized in Table 5.1. The ν^2GC-S, ν^2GC-H2 [324], and Phi-1 simulations cover the relatively large mass halos of $M \sim 10^{11} M_\odot$. The Phi-2 simulation is for intermediate mass halos of $M \sim 10^7 M_\odot$. To analyze the smallest scale of $M \sim 10^{-6} M_\odot$, the A_N8192L800 simulation is used. The cosmological parameters of these simulations are $\Omega_m = 0.31$, $\lambda_0 = 0.69$, $h = 0.68$, $n_s = 0.96$, and $\sigma_8 = 0.83$, which are consistent with an observation of the cosmic microwave background obtained by the Planck satellite [13, 322] and those adopted in the other parts of the calculations in this chapter. The matter power spectrum in the A_N8192L800 simulation contains the cutoff imposed by the free motion of dark matter particles with a mass of 100 GeV [57, 310]. Further details of these simulations are presented in [324, 325].

Table 5.1: Details of five cosmological N-body simulations used in this study. Here, N, L, and $m_{\rm p}$ are the total number of particles, box size, and mass of a simulation particle, respectively.

Name	N	L	Softening	$m_{\rm p}$ ($M_\odot$)	Reference
ν^2GC-S	2048^3	411.8 Mpc	6.28 kpc	3.2×10^8	[324,330]
ν^2GC-H2	2048^3	102.9 Mpc	1.57 kpc	5.1×10^6	[324,330]
Phi-1	2048^3	47.1 Mpc	706 pc	4.8×10^5	[325]
Phi-2	2048^3	1.47 Mpc	11 pc	14.7	[325]
A_N8192L800	8192^3	800.0 pc	2.0×10^{-4} pc	3.7×10^{-11}	[325]

All simulations are conducted by a massively parallel TreePM code, GreeM [326,327].[b1] For the identification of halos and subhalos, the ROCKSTAR phase space halo and subhalo finder [328] is used. Merger trees are constructed by consistent tree codes in [329]. The halo and subhalo catalogs, the merger trees of the ν^2GC-S, ν^2GC-H2, and Phi-1 simulations are publicly available at http://hpc.imit.chiba-u.jp/~ishiymtm/db.html.

5.3.4 comparison

We calculate the mass-loss rate of the subhalo for various redshift z and the host mass $M_{\rm host}$. The host mass is measured as M_{200}. First, we choose the subhalo mass at the accretion $m_{\rm acc}$ uniformly in a logarithmic scale between the minimum halo mass and the maximum halo mass of $0.1M(z_{\rm acc})$. $M(z_{\rm acc})$ corresponds to the host mass at the accretion redshift. We set the minimum mass of the subhalo to $m_{\rm sh} = 10^{-6}M_\odot$. For each set of $m_{\rm acc}$ and $z_{\rm acc}$ (as well as z and $M_{\rm host}$), we calculate the mass-loss rate $\dot{m}$ following the prescription given in Sec. 5.3.2. The distribution of the concentration parameter of both the host and subhalos, and the orbital distribution of the subhalos are included by adopting a Monte Carlo approach. Then the corresponding mass-loss rate of each subhalo is calculated.

In Fig. 5.2, we show the results of our Monte Carlo simulations with cyan points. The plot range of each figure is adjusted to the simulation range of the N-body calculations. Full-range results obtained by the Monte Carlo calculations are shown in the inserted figures. We find that the mass-loss rate of the subhalo in Eq. (5.1.1) is well-described with a single power-law function in more than 20 orders-of-magnitude as shown in the inserted figures. We compare the results of the Monte Carlo calculations to those obtained in the N-body simulations explained in Sec. 5.3.3. The results in N-body calculations are shown with thick blue lines. At relatively small redshifts for both $M_{\rm host} = 10^{13}M_\odot$ and $10^7M_\odot$, we find very good agreements between the two prescriptions. We also check the applicability of the analytical approach by comparing the results with those of N-body simulations for small-mass hosts

[b1] http://hpc.imit.chiba-u.jp/~ishiymtm/greem/

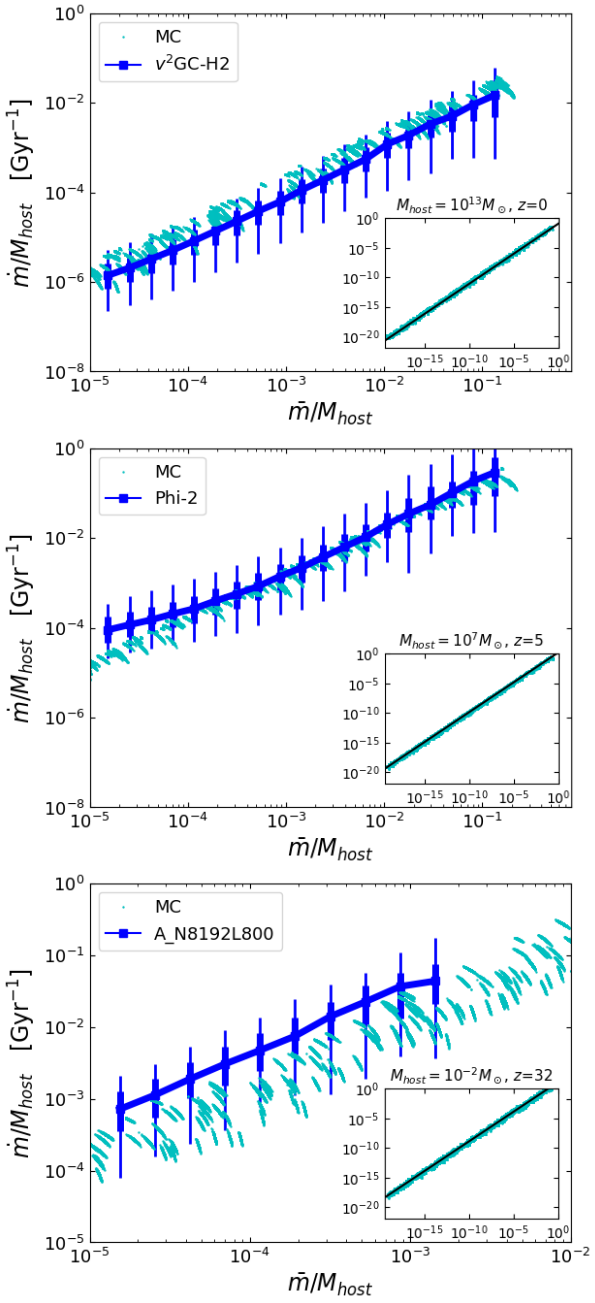

Figure 5.2: Mass-loss rate of subhalos as a function of the orbit-averaged subhalo mass $\overline{m}$ in units of the host mass $M_{\rm host}$ for $M_{\rm host} = 10^{13} M_\odot$ and $z = 0$ (*top*), $M_{\rm host} = 10^{7} M_\odot$ and $z = 5$ (*middle*), and $M_{\rm host} = 10^{-2} M_\odot$ and $z = 32$ (*bottom*). Cyan points show the Monte Carlo simulation results. Blue squares with error bars show the results obtained by N-body simulations. Thick error bars correspond to the 50% of the simulated halos around the median, while thin ones to the 90%. We also show the results of the Monte Carlo simulations of wider mass range in inserted panels, which also include the fitting results with Eq. (5.1.1), as overwritten solid lines on the Monte Carlo points.

at higher redshift, $z = 32$. In order to calculate the mass-loss rate at such a high redshift, we assume the η distribution at $z = 7$ in [323]. Even at the very high redshift and for very small host mass of $M_{\rm host} = 10^{-2} M_\odot$, the mass-loss rate $\dot{m}$ in two calculations agrees within differences of factors of a few. Although we cannot test the validity of our Monte Carlo approach for $\overline{m}/M_{\rm host} \ll 10^{-5}$ by comparing with the N-body simulations, the results shown in Fig. 5.2 from very small to large hosts as well as from very high to low redshifts give us confidence that our analytical prescription captures the physics of tidal stripping. The method can be applied even to the cases with an extremely small mass ratio $\overline{m}/M_{\rm host}$.

From each calculation of the host mass and the redshift, $(M_{\rm host}, z)$, we derive the function of the parameter A and ζ in Eq. (5.1.1). These parameters depends on the host mass $M_{\rm host}$ and the redshift z as

$$\begin{aligned} \log A &= \left[-0.0003 \log\left(\frac{M_{\rm host}}{M_\odot}\right) + 0.02\right] z \\ &\quad + 0.011 \log\left(\frac{M_{\rm host}}{M_\odot}\right) - 0.354, \end{aligned} \tag{5.3.27}$$

$$\begin{aligned} \zeta &= \left[0.00012 \log\left(\frac{M_{\rm host}}{M_\odot}\right) - 0.0033\right] z \\ &\quad - 0.0011 \log\left(\frac{M_{\rm host}}{M_\odot}\right) + 0.026. \end{aligned} \tag{5.3.28}$$

In the derivation of Eqs.(5.3.27) and (5.3.28), we use results of the Monte Carlo simulations that covers the host mass from $M_{\rm host} = 10^{-6} M_\odot$ to $10^{16} M_\odot$ and the redshift $z = 0$ to 7.

5.4 Applications

We calculate the quantities of interest related to the subhalos in this section. The mass function and the mass fraction of the subhalo, as well as the boost factor, are derived here. For this purpose, we combine the mass-loss rate obtained in by combining By combining the tidal mass-loss rate obtained in Sec. 5.3, the calculation of the profile parameters in Sec. 5.2, and the mass accretion history.

5.4.1 accretion rate of the subhalo

One has to know the number distribution of the accreting halo $d^2 N_{\rm sh}/(d \ln m_{\rm acc} dz_{\rm acc})$: the number of subhalos accreted onto the host per unit logarithmic mass range around $\ln m_{\rm acc}$ and per unit redshift range around accretion redshift $z_{\rm acc}$ to calculate the subhalo mass function and the boost factor. With the understanding of the growth history of the hosts,

the distribution $d^2N_{\rm sh}/(d\ln m_{\rm acc}dz_{\rm acc})$ can be determined using an extended Press-Schechter formalism [314]. Following the convention in [314], it is expressed as

$$\frac{d^2N_{sh}}{d\ln m_{\rm acc}dz_{\rm acc}} = \mathcal{F}(s_{\rm acc},\delta_{\rm acc}|S_0,\delta_0;\overline{M}_{\rm acc})\frac{ds_{\rm acc}}{dm_{\rm acc}}\frac{d\overline{M}_{\rm acc}}{dz_{\rm acc}}. \tag{5.4.1}$$

In Eq. (5.4.1), $s_{\rm acc}$ and $\delta_{\rm acc}$ are used to parameterize the mass and redshift, respectively. They are defined as $s_{\rm acc}\equiv\sigma^2(m_{\rm acc},z=0)$ and $\delta_{\rm acc}=\delta_c(z_{\rm acc})=1.686/D(z_{\rm acc})$ [321]. Similarly, for the host, we adopt $S_0=\sigma^2(M_0,z=0)$ and $\delta_0=\delta_{\rm c}(z_0)$ to characterize the mass M_0 and redshift z_0 as a boundary condition. The probability distribution of the mass of the host $M_{\rm acc}$ at the accretion redshift $z_{\rm acc}$ which evolves to M_0 at z_0 is denoted as $P(M_{\rm acc}|S_0,\delta_0)$. We adopt a log-normal distribution with a logarithmic mean $\overline{M}_{\rm acc}=M(z_{\rm acc}|M_0,z_0)$ of Eq. (5.3.7) and a logarithmic dispersion

$$\sigma_{\log M_{\rm acc}} = 0.12-0.15\log\left(\frac{M_{\rm acc}}{M_0}\right). \tag{5.4.2}$$

The definition of the function $\mathcal{F}$ in Eq. (5.4.1) is

$$\begin{aligned}&\mathcal{F}(s_{\rm acc},\delta_{\rm acc}|S_0,\delta_0;\overline{M}_{\rm acc})\\ =&\int\Phi(s_{\rm acc}.\delta_{\rm acc}|S_0,\delta_0;M_{\rm acc})P(M_{\rm acc}|S_0,\delta_0)dM_{\rm acc},\end{aligned} \tag{5.4.3}$$

$$\begin{aligned}&\Phi(s_{\rm acc},\delta_{\rm acc}|S_0,\delta_0;M_{\rm acc})\\ =&\left[\int_{S(m_{\rm max})}^{\infty}F(s_{\rm acc},\delta_{\rm acc}|S_0,\delta_0;M_{\rm acc})ds_{\rm acc}\right]^{-1}\\ &\times\begin{cases}F(s_{\rm acc},\delta_{\rm acc}|S_0,\delta_0;M_{\rm acc}), & (m_{\rm acc}\le m_{\rm max}),\\ 0, & (\text{otherwise}),\end{cases}\end{aligned} \tag{5.4.4}$$

$$\begin{aligned}&F(s_{\rm acc},\delta_{\rm acc}|S_0,\delta_0;M_{\rm acc})\\ =&\frac{1}{\sqrt{2\pi}}\frac{\delta_{\rm acc}-\delta_M}{(s_{\rm acc}-S_M)^{3/2}}\exp\left[-\frac{(\delta_{\rm acc}-\delta_M)^2}{2(s_{\rm acc}-S_M)}\right],\end{aligned} \tag{5.4.5}$$

where $m_{\rm max}=\min[M_{\rm acc},M_0/2]$ and $M_{\rm max}=\min[M_{\rm acc}+m_{\rm max},M_0]$ are introduced. The conditions for $m_{\rm max}$ and $M_{\rm max}$ assure the mass hierarchy of the host and subhalos. $S_M=\sigma_M^2(M_{\rm max})$ and δ_M is defined as $\delta_{\rm c}(z)$ at a redshift at which $M=M_{\rm max}$. The equations above determine the distributions of accreting subhalos $d^2N_{\rm sh}/(d\ln m_{\rm acc}dz_{\rm acc})$ for arbitrary hosts.

5.4.2 mass function of the subhalo

We calculate the mass function of subhalos in the following procedure. First, we fix the redshift of interest z_0 and the host mass at that redshift, M_0. Next, we uniformly sample $m_{\rm acc}$ in logarithmic space between $10^{-6}M_\odot$ and $0.1M_0$, and $z_{\rm acc}$ between $z_0 + 0.1$ and 10 for each set of (M_0, z_0). Each combination is characterized by a subscript i, $(\ln m_{{\rm acc},i}, z_{{\rm acc},i})$. Its weight w_i is chosen to be proportional to the subhalo accretion rate from the extended Press-Schechter formalism in Sec. 5.4.1, i.e.,

$$w_i \propto \left(\frac{d^2N_{\rm sh}}{d\ln m_{\rm acc} dz_{\rm acc}}\right)_i . \tag{5.4.6}$$

The normalization of the weight is determined by the condition

$$\sum_i w_i = N_{\rm sh,total} \tag{5.4.7}$$

where $N_{\rm sh,total}$ is the total number of subhalos ever accreted on the given host by the time $z = z_0$. $N_{\rm sh,total}$ is obtained from the numerical integrations of Eq. (5.4.1) as

$$N_{\rm sh,total} = \int d\ln m_{\rm acc} dz_{\rm acc} \frac{d^2N_{\rm sh}}{d\ln m_{\rm acc} dz_{\rm acc}} \to \sum_i w_i. \tag{5.4.8}$$

We calculate the subhalo mass at z_0 after tidal stripping, $m_{0,i}$, by integrating Eq. (5.1.1) over cosmic time from that corresponding to $z = z_{{\rm acc},i}$ to $z = z_0$. The parameters A and ζ are taken from Eqs. (5.3.27) and (5.3.28), respectively. For each set specified with i, we obtain the subhalo concentrations at the accretion following the log-normal distribution $P(c_{\rm vir,acc}|m_{{\rm acc},i}, z_{{\rm acc},i})$ as discussed in Sec. 5.2. For the concentration-mass relation, we adopt the model in [316] (see Sec. 5.3.1). Then we calculate the scale radius $r_{s,i}$ and the characteristic density $\rho_{s,i}$ at redshift $z_{{\rm acc},i}$ as functions of $c_{\rm vir,acc}$. The characteristic density and the scale radius after the tidal stripping are determined from those quantities before the stripping and the mass ratio of the subhalo before and after the tidal stripping, $m_{0,i}/m_{\rm acc}$, as explained in Sec. 5.2. We remove the halos of which truncation radius $r_{t,i} < 0.77 r_{s,i}$ at $z = z_0$ after the tidal stripping. Such halos are regarded to be completely disrupted.

The subhalo mass function is then constructed as the distribution of $m_{0,i}$ properly weighted by w_i:

$$\begin{aligned}\frac{dN_{\rm sh}}{dm} &= \sum_i w_i \delta(m - m_{0,i}) \\ &\quad \times \int dc_{\rm vir,acc} P(c_{\rm vir,acc}|m_{{\rm acc},i}, z_{{\rm acc},i}) \\ &\quad \times \Theta[r_{t,i}(z_0|c_{\rm vir,acc}) - 0.77 r_{s,i}(z_0|c_{\rm vir,acc})],\end{aligned} \tag{5.4.9}$$

where $\delta(x)$ and $\Theta(x)$ are the Dirac delta function and Heaviside step function, respectively. Our calculation includes the condition of tidal disruptions.

The subhalo mass function has been studied most commonly through N-body simulations in the literature. We compare in Fig. 5.3 the subhalo mass function $m^2 dN_{\rm sh}/dm$ obtained by the numerical simulations and by our analytical model of Eq. (5.4.9). Three panels in Fig. 5.3 differ in the host mass and the redshift. In the *top* panel, we compare the subhalo mass function at $z = 0$. The cases of the host mass $M_{\rm host} = 1.8 \times 10^{12} M_\odot$ and $5.9 \times 10^{14} M_\odot$ are shown. The fitting functions corresponding to the results of [305] and [331] are also shown. In both cases, the simulations and analytical models show reasonable agreements, while our model predicts fewer subhalos. In the *middle* panel, we compare the mass function at $z = 2$ and $z = 4$ with results of [332], as well as of ν^2GC-H2 simulation, for the host of which mass $M_{\rm host} = 10^{13} M_\odot$ at $z = 0$. This again shows very good agreements between the two approaches in resolved regimes of numerical simulations. Our model can also be applied to even smaller hosts. This is shown in the *bottom* panel. The subhalo mass function for $M_{\rm host} = 10^6 M_\odot$ and $10^7 M_\odot$ at $z = 5$ are compared with the results of the Phi-2 simulations. The results agree well down to the resolution limit of the numerical simulation at around $\sim 500 - 1000 M_\odot$. Hence, the subhalo mass functions in our analytical model are well-calibrated to the results of the numerical simulations. This assures that our analytical model captures the important physics of the subhalo evolutions. The behavior at the low-mass end down to very small mass scales can be regarded as reliable.

In Fig. 5.4, we show the slope of the subhalo mass function

$$-\alpha = \frac{d \ln(dN_{\rm sh}/dm)}{d \ln m}, \tag{5.4.10}$$

(i.e., $dN_{\rm sh}/dm \propto m^{-\alpha}$) for the same host and redshifts as those in Fig. 5.3. We find that the slope α lies in a range between 2 and 1.8 for a large range of the subhalo mass m. The exceptions are those at the lower and the higher edges where the mass function features cutoffs. This is consistent with one of the findings from the numerical simulations, again confirming the validity of our analytical prescription.

The mass fraction of the subhalo obtained as

$$f_{\rm sh} = \frac{1}{M_{\rm host}} \int_{10^{-6} M_\odot}^{0.1 M_{\rm host}} dm\, m \frac{dN_{\rm sh}}{dm}. \tag{5.4.11}$$

This is shown in Fig. 5.5. At redshift $z = 0$, the mass fraction of the subhalo is smaller than $\sim$10% level up to cluster-size halos ($M_{\rm host} \sim 10^{15} - 10^{16} M_\odot$). The fraction $f_{\rm sh}$ gets larger at high redshifts. The suppression of the tidal mass-loss effect at high redshifts is responsible for this feature. For comparison, we show the results obtained from N-body simulation in [332] with square markers in the figure. In the N-body calculation, contributions from the subhalos in the mass range of $1.73 \times 10^{10} h^{-1} M_\odot$ and $0.1 M_{\rm host}$ are counted. A good agreement can be seen with the thin blue line corresponds to our calculation in the same subhalo mass range.

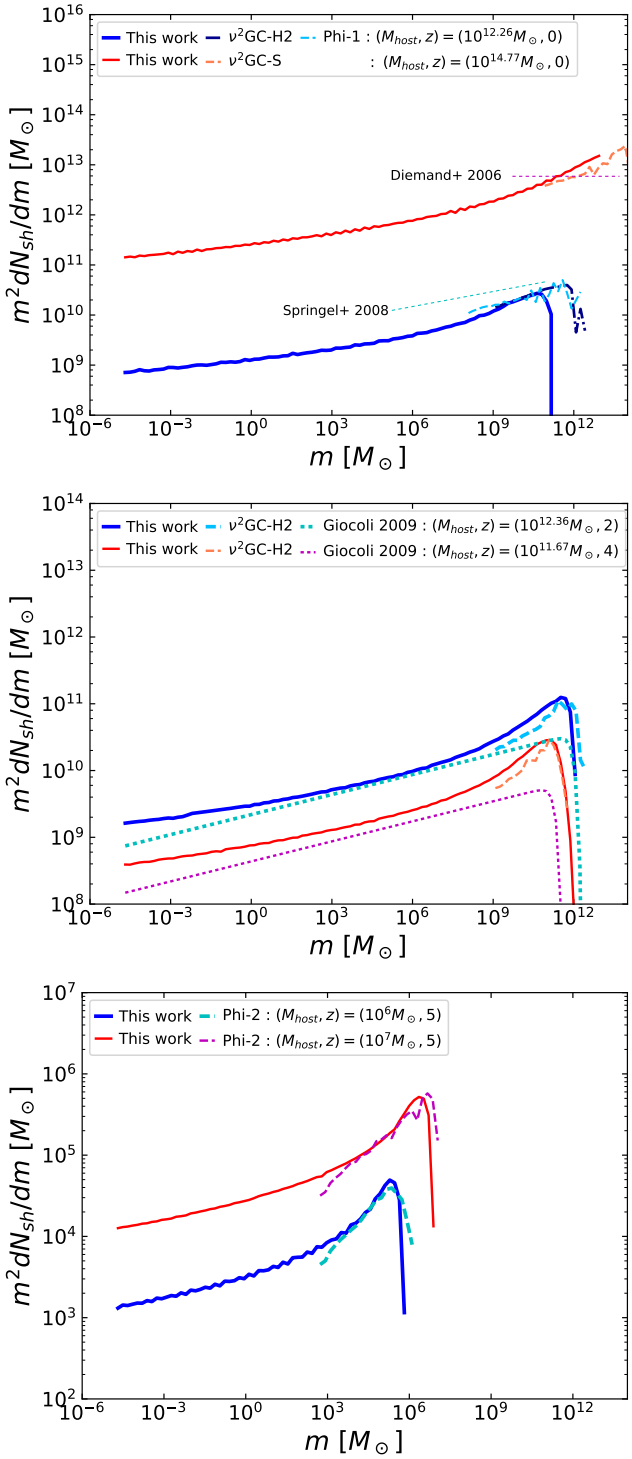

Figure 5.3: Comparison of the mass function of subhalos. *Top*: Comparison at $z = 0$. Thick-blue lines correspond to the $M_{\rm host} = 1.8 \times 10^{12} M_\odot$ while the thin-red lines to $5.9 \times 10^{14} M_\odot$. Solid (Dashed) lines correspond to the analytical (N-body) results. Fitting functions in [305] for $M_{\rm host} = 1.8 \times 10^{12} M_\odot$ and in [331] for $5.9 \times 10^{14} M_\odot$ are also shown. *Middle*: Cases of $M_{\rm host} = 2.3 \times 10^{12} M_\odot$ at $z = 2$ (blue) and $M_{\rm host} = 4.7 \times 10^{11} M_\odot$ at $z = 4$ (red), compared to the N-body results in Table 5.1 and [332]. *Bottom*: Comparison at $z = 5$ for $M_{\rm host} = 10^6 M_\odot$ (blue) and $M_{\rm host} = 10^7 M_\odot$ (red). The lines corresponding to our N-body results extend toward large masses because halos of various masses around a given geometric mean are stacked to derive the mass functions.

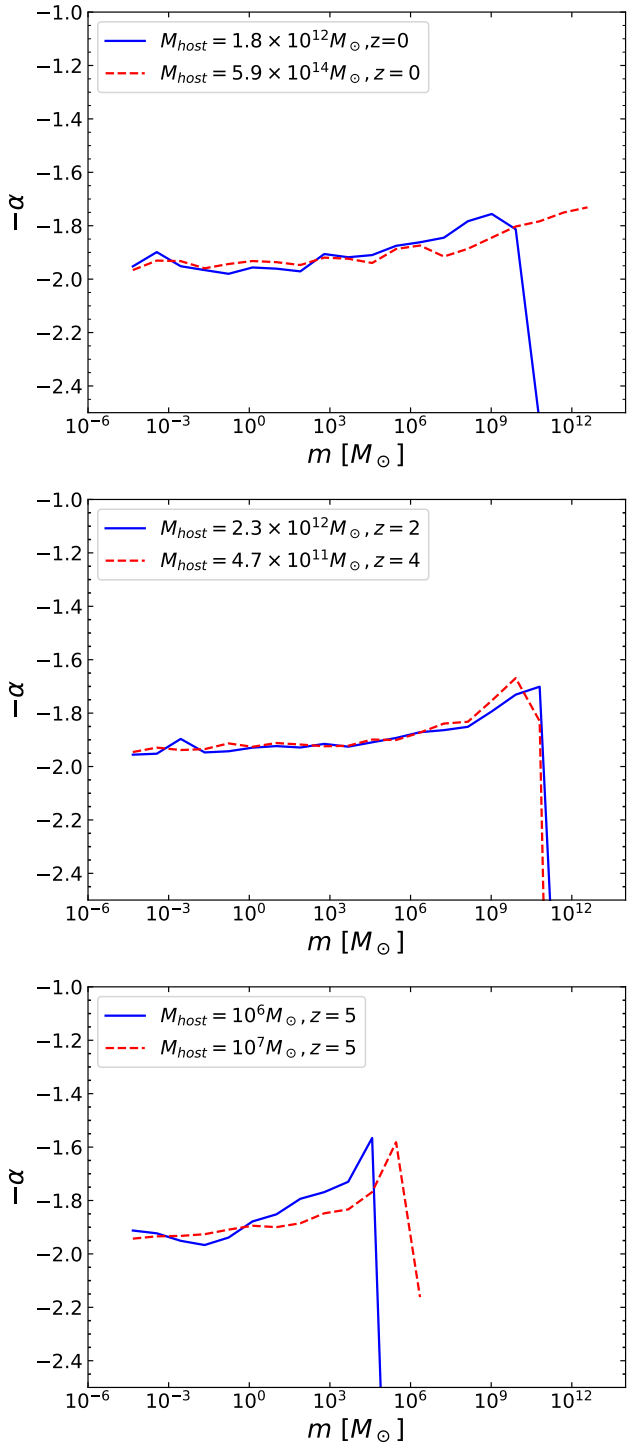

Figure 5.4: The slope of the subhalo mass function $-\alpha = d\ln(dN_{\rm sh}/dm)/d\ln m$ as a function of the subhalo mass m. The slope is averaged over mass bins of width $\Delta \log m = 1$.

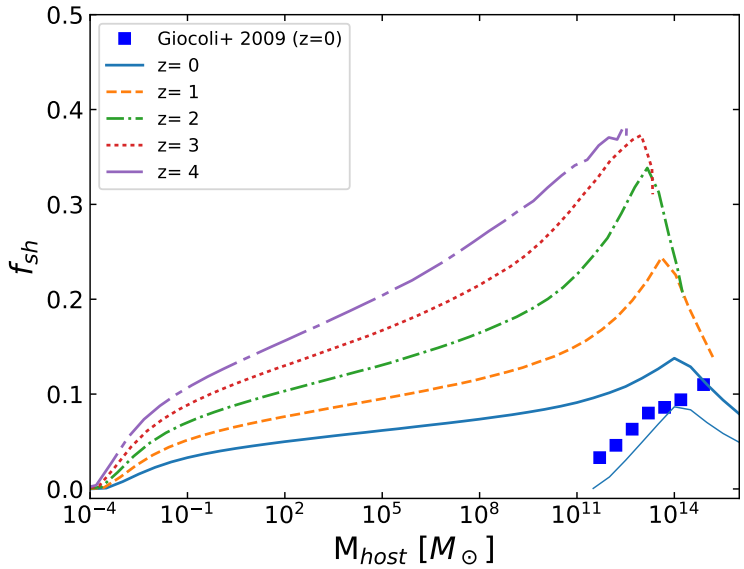

Figure 5.5: Mass fraction of subhalos $f_{\rm sh}$ as a function of $M_{\rm host}$, for $z = 0$, 1, 2, 3, and 4. Blue squares represent the subhalo mass fractions in [332], which are derived using subhalos in the mass range between $1.73 \times 10^{10} h^{-1} M_\odot$ and $0.1 M_{\rm host}$. Solid thin line shows the corresponding subhalo mass fraction in our calculation.

5.4.3 boost factor

Assuming a host halo of NFW profile, the γ-ray luminosity from the dark matter annihilation is expressed as

$$L_{\rm host}(M) \propto \int dc_{\rm vir} P(c_{\rm vir}|M,z)\rho_s^2 r_s^3 \left[1 - \frac{1}{(1+c_{\rm vir})^3}\right], \tag{5.4.12}$$

where $P(c_{\rm vir}|M,z)$ is again the log-normal distribution of the host's concentration parameter for a given host mass M and the redshift z. The scale radius r_s and the characteristic density ρ_s are both dependent on $c_{\rm vir}$ as well as on the mass M and the redshift z. We do not show the constant of the proportionality of the relation in Eq. (5.4.12). It includes particle physics parameters such as the mass and the annihilation cross-section of dark matter particles. However, the constant is canceled in the boost factor by taking the ratio of the host and subhalo luminosity.

The enhancement of the dark matter annihilation signal due to the contribution from all the subhalos is quantified as the boost factor. It is defined as

$$B_{\rm sh}(M) = \frac{L_{\rm sh}^{\rm total}(M)}{L_{\rm host}(M)}, \tag{5.4.13}$$

then, the total luminosity from the halo is given as $L_{\rm total} = (1 + B_{\rm sh})L_{\rm host}$. Following the prescription in this thesis, all the subhalos today are characterized with its accretion mass $m_{{\rm acc},i}$, the virial concentration at the accretion $c_{\rm vir,acc}$, and the accretion redshift $z_{{\rm acc},i}$. Then the luminosity from a single subhalo i is also characterized with these quantities. The luminosity of each subhalo is determined as

$$L_{{\rm sh},i} \propto \rho_{s,i}^2 r_{s,i}^3 \left[1 - \frac{1}{(1 + r_{t,i}/r_{s,i})^3}\right], \tag{5.4.14}$$

where $r_{s,i}$, $r_{t,i}$, and $\rho_{s,i}$ are the scale radius, truncation radius, and characteristic density of the subhalo i after it experienced the tidal mass loss. They also depend on the host mass M and the observation redshift z. The total subhalo luminosity $L_{\rm sh}^{\rm total}(M)$ is obtained as the sum of $L_{{\rm sh},i}$ with weight w_i and averaged over $c_{\rm vir,acc}$ with its distribution:

$$\begin{aligned} L_{\rm sh}^{\rm total}(M) \;=\; & \sum_i w_i \int dc_{\rm vir,acc} P(c_{\rm vir,acc}|m_{{\rm acc},i}, z_{{\rm acc},i}) \\ & \times L_{{\rm sh},i}(z|c_{\rm vir,acc}) \\ & \times \Theta[r_{t,i}(z|c_{\rm vir,acc}) - 0.77 r_{s,i}(z|c_{\rm vir,acc})]. \end{aligned} \tag{5.4.15}$$

Presence of sub-subhalos

As shown in the literature, the halo structure is highly hierarchical. This is because the subhalos before the accretions have been formed by mergers or accretions of even smaller halos. Then, there should exist sub-subhalos and further substructures in the subhalos of the host halo. In the following, we refer to them as sub^n-subhalos. Note that the discussion in the above section corresponds to the case of $n = 0$, where subhalos do not include sub-subhalos. Especially Eq. (5.4.14) is based on the assumption that the density profile of subhalos is given by smooth NFW profile neglecting the sub-sub halo contributions.

We include the effect of sub^n-subhalos iteratively. In the case of $n \geq 1$, when a subhalo i accretes at $z_{\rm acc,}i$ with a mass $m_{\rm acc,}i$, we give it a sub-subhalo boost $B_{\rm sh}^{(n-1)}(m_{\rm acc,}i, z_{\rm acc,}i)$ obtained from the previous iteration; for $n = 1$, it is Eq. (5.4.13) evaluated at $m_{\rm acc,}i$ and $z_{\rm acc,}i$. After the subhalo experiences the tidal mass-loss, its sub-subhalos as well as the subhalo component are stripped away up to the tidal radius $r_{t,i}$. It is known that the sub-subhalo distribution (that the γ-ray brightness profile from the sub-subhalos follows) is flatter than the brightness profile of the subhalo's smooth component that is proportional to the NFW profile squared (e.g. [333]), then the sub-subhalo boost decreases. In order to quantify this effect, we assume that the sub-subhalos are distributed as $n_{\rm ssh}(r) \propto (r^2 + r_s^2)^{-3/2}$ which is a favored form in previous works (e.g. [145] and references therein). We also assume that the NFW profile parameter r_s and ρ_s hardly change after the mass loss. Then the total sub-subhalo luminosity enclosed within a radius of r from the center of the host halo is

$$L_{{\rm ssh},i}(< r) \propto \ln\left[\sqrt{1+\left(\frac{r}{r_{s,i}}\right)^2} + \frac{r}{r_{s,i}}\right] - \frac{r}{\sqrt{r^2 + r_{s,i}^2}}. \tag{5.4.16}$$

On the other hand, the enclosed luminosity from the smooth NFW component is

$$L_{{\rm sh},i}(< r) \propto 1 - \left(1 + \frac{r}{r_{s,i}}\right)^{-3}. \tag{5.4.17}$$

The sub-subhalo boost for the subhalo i at redshift z after n-th iteration is therefore estimated as

$$\begin{aligned} B_{{\rm ssh},i}^{(n)}(z) &= B_{\rm sh}^{(n-1)}(m_{\rm acc,}i, z_{\rm acc,}i) \\ &\quad \times \frac{L_{{\rm ssh},i}(< r_{t,i})/L_{{\rm ssh},i}(< r_{{\rm vir},i})}{L_{{\rm sh},i}(< r_{t,i})/L_{{\rm sh},i}(< r_{{\rm vir},i})}, \end{aligned} \tag{5.4.18}$$

where $r_{{\rm vir},i}$ is the virial radius of the subhalo i at the accretion.

We finally obtain the subhalo boost factor after n-th iteration (that takes up to sub^{n-1}-subhalos into account), $B_{\rm sh}^{(n)}(M, z)$, by combining Eqs. (5.4.12)–(5.4.15), but also by multiplying

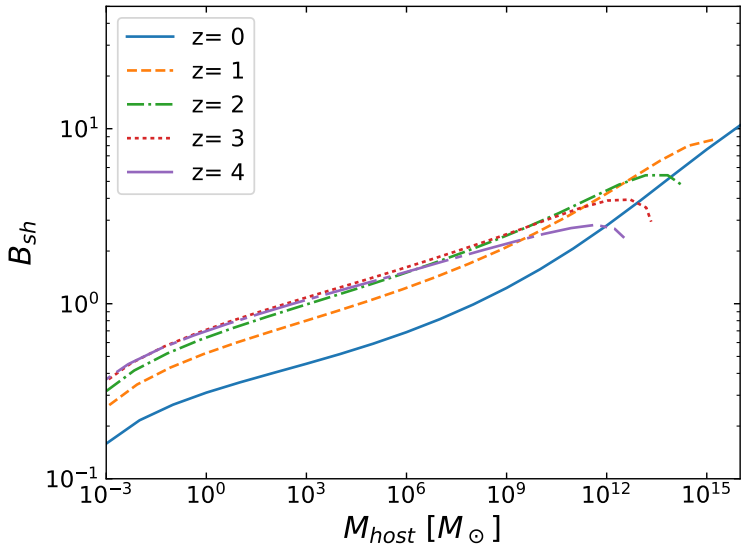

Figure 5.6: Boost factor $B_{\rm sh} = L_{\rm sh}^{\rm total}/L_{\rm host}$ as a function of the host mass $M_{\rm host}$ (defined as M_{200}) between $10^{-3}M_\odot$ and $10^{16}M_\odot$ at observation redshifts $z = 0$, 1, 2, 3, and 4. The calculations include up to sub^3-subhalos.

$L_{{\rm sh},i}$ in Eq. (5.4.14) with $1+B^{(n)}_{{\rm ssh},i}(z_0)$ in Eq. (5.4.18). In this calculation, we consider the subhalos accreted after $z = 10$ to calculate the boost factor at $z < 5$. Fig. 5.6 shows the boost factor $B_{\rm sh}$ as a function of host mass $M_{\rm host}$ for several redshifts, after the fourth iteration that takes up to sub^3-subhalos into account. Host mass is defined as M_{200}. For $z = 0$, the subhalo boost increases gradually with the mass of the host halos and reaches to about a factor of ∼10 for cluster-size halos while it is smaller than 1 for halos of the dwarf spheroidal galaxy scale. The boost is significant at higher redshifts, being on the order of ∼ 1 for a wide range of host masses.

The effect of the higher-order subhalos (sub^n-subhalos) is shown in Fig. 5.7. In this figure, we show the boost factor at redshift $z = 0$. The boost factor could be underestimated if we neglect the contributions from higher-order substructures. It can differ by about a factor of a few for cluster-scale halos. We find that the boost saturates after the third iteration, after which further enhancement is of several percent levels.

Dependence on the concentration-mass relation

In our calculations of the boost factor, we adopted the concentration-mass relation in [316] as the canonical model. Their derivation is based on the analysis with N-body simulations. However, the concentration-mass relation is a topic under discussion. In order to compare the

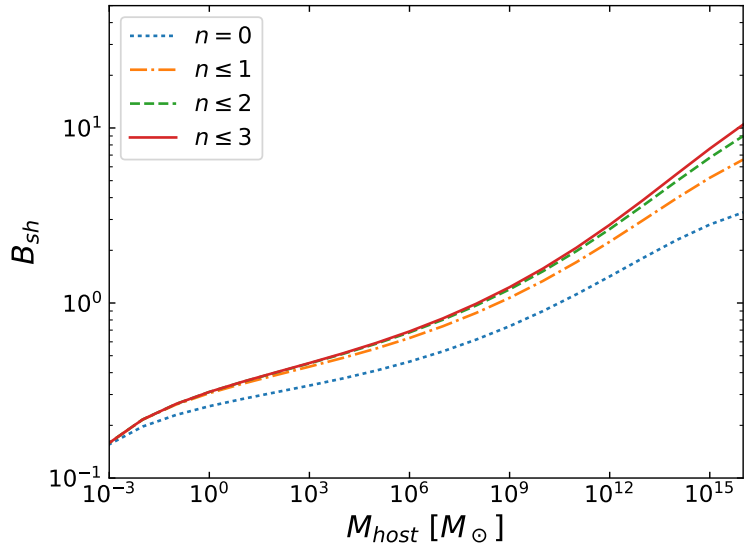

Figure 5.7: Subhalo boost factor at $z = 0$ including sub^n-subhalos; i.e., n-th sub-substructure.

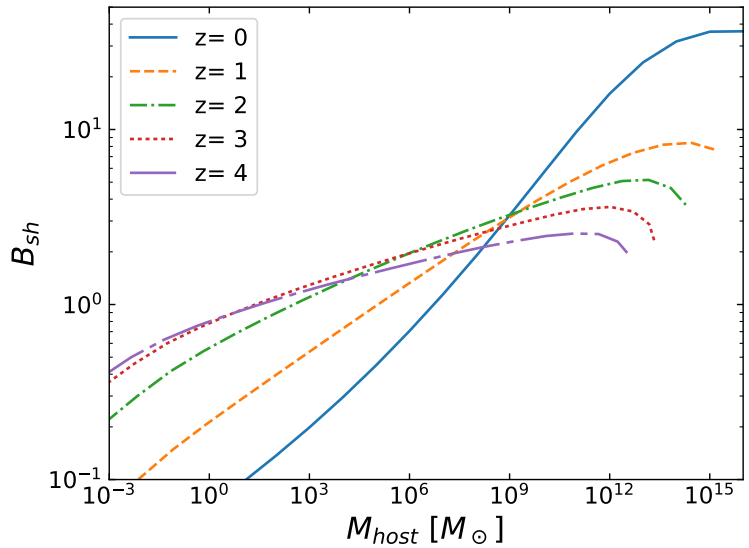

Figure 5.8: The same as Fig. 5.6, but for the concentration-mass relation in [334].

boost factor with different concentration-mass relations, we adopt another model proposed in [334] and conduct the same calculation. The concentration-mass relation in [334] is derived from analytical discussions. The difference between the two models is that a higher value of the concentration is expected in [334] especially around $z = 0$. Fig. 5.8 is the boost factor assuming the concentration-mass relation in [334]. The boost factor enhances by more than a factor of a few compared to the value obtained with [316]. The boost factor directly reflects the difference of the concentrations around redshift $z = 0$. Our results show that a deeper understanding of the concentration-mass relation is necessary to obtain the boost factor corresponding to the actual situations.

Note that the concentration-mass relation is related to the primordial curvature perturbations in the early Universe [335]. The primordial power spectrum which can produce the ultra-compact minihalos (e.g. [336]) should enhance the boost factor significantly by changing the density profiles and the concentration-mass relation. In fact, possibilities of such significant boosts are discussed in [335, 337]. However, such extreme cases may already be constrained by current γ-ray observations.

A case without tidal disruption

There is an argument that the tidal disruption of the subhalo is a numerical artifafct [306]. If this is the case, we can expect a larger number of subhalos even with much smaller truncation radius $r_t < 0.77 r_s$ could survive against the tidal disruption. Our condition that requires $r_t \geq 0.77 r_s$ leads to a conservative estimate if this is the case. We repeat the same calculation without implementing the condition for tidal disruption $r_t \geq 0.77 r_s$ assuming that the survival of the subhalo does not depend on the amount of the stripped mass. The obtained boost factor hardly changes at any redshift.

5.5 Discussions

5.5.1 comparison with earlier works

Analytical calculations of the boost factor are conducted in previous works such as [311] and [333]. Comparing with the calculation of [311], the following points are improved: (i) the implementation of the scatter distribution in the concentration-mass relation for host and subhalos, (ii) the calibration of the subhalo mass-loss rate down to the extremely small mass ratio m/M using the Monte Carlo simulations of the tidal stripping, (iii) the extension in the calculations of the boost factor as well as the subhalo mass function beyond $z = 0$, and (iv) the inclusion of the higher-order substructures. Our results are consistent with those in [311] if we omit the contribution from the sub^n-subhalos with $n \geq 1$. By including up to the sub^3-subhalo, the enhancement of the boost factor by a factor of a few is expected in the largest

halos. Our results are also consistent with that obtained in another analytical work [333] after integrating over the entire volume of the halo and assuming the subhalo mass function of $dN_{\rm sh}/dm \propto m^{-1.9}$. They consider subhalos in a Milky-Way-like halo at $z = 0$ and include the effect of the disk shocking as well as the tidal stripping. We can directly compare our results with that of [333] if we extend our calculations to include baryonic effects. Another work to compare is the calculation of the subhalo boost in [338,339]. They have developed a different analytical model assuming self-similarity of the substructures and computed the probability distribution function of the dark matter density that has a power-law tail, then calibrated it with numerical simulations of the Galactic halo. The boost factor within the volume of the virial radius of ~200 kpc have been found to be a factor of ~10, which is slightly higher than our result with the canonical model. Two results are quantitatively consistent if we adopt the concentration-mass relation of [334].

5.5.2 updates on the current IGRB limit

The boost factor at a higher redshift is calculable with our analytical model. Applying the result of the boost calculations, we update the current limits on the dark matter annihilation cross-section with the isotropic γ-ray background (IGRB) observations. The latest measurements of the IGRB intensity is available in [141,147]. In Fig. 5.9, we show the observed γ-ray intensity and the expected flux from the dark matter annihilations. We assume the case that dark matter of mass $m_{\rm DM} = 100$ GeV annihilates into $\bar{b}b$ with the canonical cross-section of $\langle\sigma v\rangle \sim 2 \times 10^{-26}$ cm^3/s [38] in this figure. Following the "halo model" approach of [145] to compute the contribution of the dark matter annihilation signal in the IGRB, a factor of a few enhancement of the dark matter annihilation signal is expected when subhalos exist. In our formalism, we can automatically compute all the subhalo properties at once including mass function and the boost factor.

The constraints on the annihilation cross-section are derived by performing a simple analysis of the *Fermi* IGRB data [147]. Two components are included: (1) dark matter annihilation of a given mass $m_{\rm DM}$ and assuming a $\bar{b}b$ final state, and (2) an "astrophysical" power-law component with a cutoff. We adopt the best-fit spectral shape, $I_{\rm astro}(E) \propto E^{-2.32} \exp(-E/279\ {\rm GeV})$ in [147] for the astrophysical component. The normalizations of these components are free parameters of the fitting procedure. We derive the upper limits on the cross-section $\langle\sigma v\rangle$ conducting the $\Delta\chi^2$ analysis. For the IGRB data, we adopt those for a foreground model "A" in [147], but treat statistical and systematic uncertainties as independent errors.

By implementing the results of our boost calculations, the current constraints are updated as shown in Fig. 5.10. Fig. 5.10 shows the upper limits on $\langle\sigma v\rangle$ at 95% confidence level ($\Delta\chi^2 = 2.71$) using our canonical boost model assuming the concentration-mass relation in [316]. The upper limit obtained by assuming no boosts is also shown. The subhalo boost improves the constraints by a factor of a few. The improvements are almost independent of the dark matter

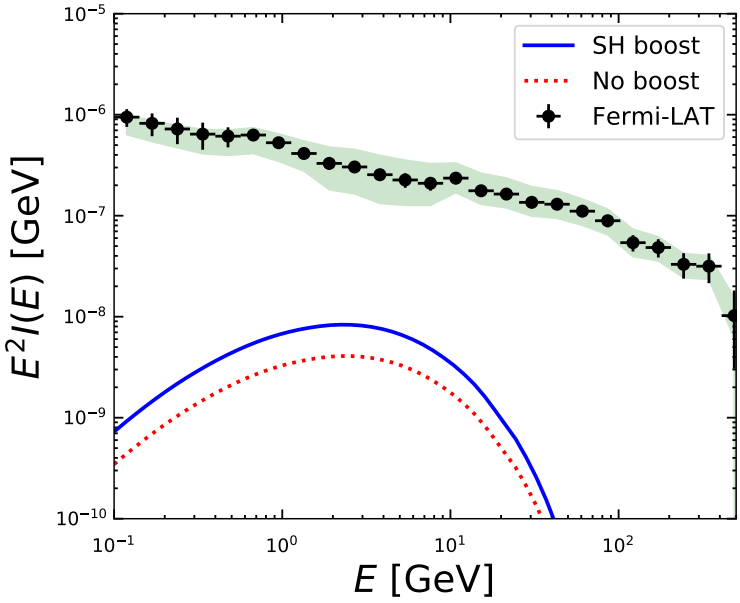

Figure 5.9: Contriubtion to the IGRB intensity measured by *Fermi* satellite from dark matter annihilation for $\langle\sigma v\rangle = 2\times10^{-26}$ cm$^3/s$, $m_{\rm DM} = 100$ GeV, and $\bar{b}b$ final state. The solid (dotted) curve shows the case of the subhalo boost (no boost).

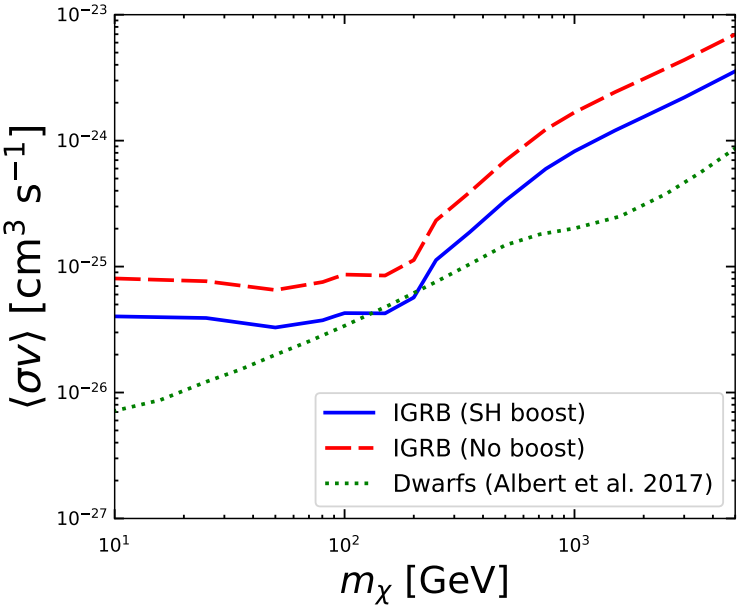

Figure 5.10: Upper limits on the dark matter annihilation cross section at 95% confidence level as a function of dark matter mass. The dark matter annihilation into the $\bar{b}b$ pair is assumed. Solid and dashed curves are for the canonical boost model and without subhalo boost, respectively. For comparison, the result of the latest joint-likelihood analysis of 41 dwarfs [45] are shown with a dotted curve.

mass, which is consistent with the tendencies seen in the previous works (e.g. [340, 341]). Our estimate is conservative in the sense that we do not include the contribution from the Galactic subhalos [342]. We also compare our limits with the latest results of the joint likelihood analysis of 41 dwarf spheroidal galaxies [45], which set the benchmark as the most robust constraints on the dark matter annihilation cross-section.

One might expect some improvements of the limit obtained from the observations of dwarf spheroidal galaxies with subhalos. However, this effect is negligible as is already discussed in [311]. We find that the IGRB limits with our boost model are competitive to the results obtained from observations of dwarf spheroidal galaxies at ~200 GeV. Note that more accurate limits should include uncertainties coming from modeling of the astrophysical contributions (e.g. [143]). A further consideration is needed [148] for correct values.

We can also implement our subhalo boost in different ways. The small-scale angular power spectrum of the IGRB has also been measured with *Fermi* satellite [146], which is another way to search dark matter annihilation signals [145, 343] as well as high-energy astrophysical sources [344, 345]. It is also pointed out that taking cross-correlations with local

gravitational tracers such as galaxy catalogs is a promising way along the same line [150, 346, 347]. Since these constraints obtained from the analysis of the anisotropy are more sensitive to the dark matter distribution at smaller redshifts and in larger hosts, the effect of the subhalo boost is expected to be even more important than for the example case using IGRB intensity. We also note that our updated boost model will impact the result of stacking analysis of nearby galaxy groups [348], which relied on the boost model of [311].

5.6 Summary

We examined possible enhancements of the dark matter annihilation signals, which is referred to as the boost, in dwarf spheroidal galaxies by contributions from subhalos. In WIMP dark matter scenarios, the existence of small-scale halos of $M \sim 10^{-6} M_\odot$ is naturally expected. Such halos cannot be resolved in N-body simulations, which are traditional ways to study halo structures. In previous works based on N-body simulations, the estimates of the boost factor differ by more than one order-of-magnitude depending on the models of extrapolations. We reduced these uncertainties by developing a new analytical formalism to calculate the evolution of the subhalo and the boost factor. Our formulation is physically motivated and not limited by the numerical resolution. It can cover more than 20 orders-of-magnitude in halo mass and the redshift up to $z \sim 10$.

We modeled the tidal mass-loss of the subhalos after their accretion onto the hosts and derived the mass-loss rate as a function of the host mass and the redshift. As shown in Fig. 5.2, the mass-loss rates calculated in our analytical formalism are consistent with those of N-body simulations in resolved regimes. Combining the derived relation for mass-loss rates with the mass accretion history in the extended Press-Schechter formalisms, we derived the mass function and the mass fraction of subhalos for hosts of $M_{\rm host} = 10^{-4} - 10^{16} M_\odot$ and redshift up to $z \sim 10$. We show in Figs. 5.3, 5.4, and 5.5 that the results of our analytical calculations agree well with those of the N-body simulations. We calculated the boost factor taking the contributions from the halos down to the minimum-mass scales and up to the sub^3-subhalos into account. The boost factor is less than one for present-day dwarf spheroidal galaxies while it is as high as a factor of ~ 10 for galaxy clusters. This is shown in Fig. 5.6. We also calculated the boost factor assuming a different concentration-mass relation and showed that the boost could not be expected in dwarf spheroidal galaxies. For larger halos of $M_{\rm host} \gtrsim 10^{12} M_\odot$, the boost factor increases by changing the concentration-mass relation.

Contributions from subhalos in the largest scale halos of $M_{\rm host} \sim 10^{15} - 10^{16} M_\odot$ and at higher redshifts affect the dark matter search in galaxy clusters and/or isotropic γ-ray backgrounds. At dwarf spheroidal galaxy scales of $M_{\rm host} \lesssim 10^{8} M_\odot$ it does not occur. Hence we conclude that the uncertainties are fewer for dwarf spheroidal galaxies and they good targets to search dark matter with Cherenkov Telescope Array.

Chapter 6

Conclusion

In this thesis, we have discussed dark matter searches in dwarf spheroidal galaxies (dSphs) with Cherenkov Telescope Array (CTA). We focused on the Weakly Interacting Massive Particle (WIMP), which is one of the strongest candidates for dark matter. Assuming that the annihilation cross-section into the standard model particle to be the canonical value of $\langle\sigma v\rangle \sim 3\times10^{-26}\mathrm{cm}^3/s$, WIMP of mass $m_{\mathrm{DM}} \sim O(1)$ GeV - $O(1)$ TeV naturally achieves the relic abundance through the thermal freeze-out mechanism. Observations of dSphs with *Fermi* satellite constrains the annihilation cross-section of the WIMP of $m_{\mathrm{DM}} \sim O(1) - O(100)$ GeV to be smaller than the canonical value. CTA is expected to enhance our accessibility to the dark matter heavier than $m_{\mathrm{DM}} \gtrsim O(1)$ TeV. Different from the observations with *Fermi* satellite, dSphs are resolved as extended sources with CTA.

In Chapter 4, we have investigated how the spatial extension of the target dSphs affects the sensitivity to dark matter. For this purpose, we sampled the dark matter density profiles of Draco dSph and calculated the 2-σ level upper limits on the annihilation cross-section with a simulated 500-hour observation of this dSph with CTA. We conducted binned maximum-likelihood analyses assuming 16 different profiles and 3 annihilation channels, $\bar{b}b$, W^+W^-, and $\tau^+\tau^-$. If we simply adopt the profiles in the literature, the sensitivity differs by a factor of ∼10 as shown in Fig. 4.13. Both of the value of the J-factor and the spatial extension contribute to the uncertainty in this case. Removing the J-factor dependence in the analyses, we showed for the first time that the spatial extension of the target dSph should affect the sensitivity in a different way from that of the J-factor. This is shown in Fig. 4.15. In the most optimistic case, we can search the dark matter annihilation signal corresponding to the cross-section of $\langle\sigma v\rangle \sim O(10^{-25} - 10^{-24})$ cm$^3/s$ for the dark matter of $m_{\mathrm{DM}} \gtrsim O(1)$ TeV. The limits shift upwards by a factor of ∼10 if we adopt profiles with larger spatial extensions. We can explore the annihilation cross-section down to $\langle\sigma v\rangle \lesssim O(10^{-22})$ cm$^3/s$ for the dark matter of $m_{\mathrm{DM}} \sim O(1) - O(10)$ TeV in the most conservative case, which cannot be achieved with the other γ-ray experiments. Parts of well-motivated models with resonant annihilations can be

tested by observing dSphs with CTA. The dependence on the spatial extension of the profile is clarified in Fig. 4.16 introducing a new quantity θ_{90} as the parametrization of the source size. θ_{90} is defined to be the angular scale corresponds to the 90% containment radius of the J-factor. When the spatial extension of the target dSph, θ_{90}, is larger than $\sim$ 1 degree, the upper limits on the annihilation cross-section get milder by more than a factor of a few compared to the case analyzing a point source of the same J-factor. The index of the density profile γ of $\rho(r) \propto r^{-\gamma}$ also affects the sensitivity. Dependence of the source-size effect on the dark matter mass is understood with the characteristics of the instrument.

The boost of the dark matter annihilation signals caused by the subhalos in the focusing halos is another source of the uncertainty. In Chapter 5, we showed that the subhalo boost is negligible for dSph scale halos. In order to quantify the contributions to the dark matter annihilation signals from such small-scale structures beyond the resolution of the N-body calculations, we developed a new method to calculate the evolution of subhalos in an analytical way. We modeled the tidal stripping of subhalos approximating that the tidal mass-loss occurs in the first orbit of the subhalos after their accretion onto the hosts. We also assumed NFW profiles up to the truncation radius for host and subhalos in our formulation. Combining the derived relation of the tidal mass-loss with the mass accretion history of subhalos and the host evolution in the extended Press-Schechter formalism, we derived the subhalo mass function and the boost factor. Our results of the tidal mass-loss rate, the subhalo mass function, and the subhalo mass fraction are consistent with those of N-body calculations in resolved regimes. Figs. 5.2, 5.3, and 5.5 show the consistency between the two calculations. Furthermore, our formulation covers more than 20 orders in the halo mass and the redshift up to $z \sim 10$. The contributions from the halos down to the minimum scale of $M \sim O(10^{-6})M_\odot$ in the galaxy cluster scales of $M \sim O(10^{16})M_\odot$ are quantified. For dSph scale hosts of $M \sim O(10^{8})M_\odot$, the boost factor is less than one while it reaches a factor of $\sim$ 10 at the galaxy cluster scale. This means that the uncertainties in the dark matter search in dSphs are dominated by those in dark matter density profiles and the contributions from the subhalos are negligible. Compared to the other targets proposed in the *Key Science Project* of CTA, dSphs are better-motivated targets to obtain robust constraints on the dark matter properties since they do not contain astrophysical sources nor booster subhalos.

The nature of the dark matter is one of the most important problems in modern physics. There are motivations to search them in the Universe where the first indication for dark matter was found. The field of the indirect dark matter search is now rapidly developing. Taking this approach, we can access the higher energy regions beyond the scope of the laboratory experiments. However, the ability of this approach is limited by our knowledge about the astrophysics. One of the most important tasks in the indirect dark matter search is to reduce the uncertainty coming from astrophysical modelings. Competing astrophysical emissions, dark matter distributions in the region of interest and on the line-of-sight, are examples. In spite of such uncertainties, our knowledge about the heavier dark matter of

$m_{\rm DM} \gtrsim O(1)$ TeV should be enlarged in this era. We showed in this thesis that we will soon access the unexplored parameter regions of dark matter with CTA. For example, we could capture the signatures of WIMP dark matter if we observe dSph with high J-factors and small angular extensions. If we detect no signatures of WIMPs, which are thought to be one of the strongest candidates, it may imply that we have to consider other possibilities seriously. In either of the case, precise understandings about the environment of the observing regions are required. The importance of the astrophysical knowledge increases for observations with advanced facilities like CTA. We tackle these problems in future works.

Acknowledgement

First of all, I would like to express my great gratitude to Masahiro Kawasaki for his careful and thoughtful support as my supervisor at the University of Tokyo. I also deeply thank my supervisor at the KEK, Kazunori Kohri. Their supports realized the further opportunity for me to collaborate with Shin'ichiro Ando. I would like to appreciate the collaboration with him. My works are also supported by other great collaborators, Masaaki Hayashida and Tomoaki Ishiyama.

I would like to express my appreciation to two communities here. One is the *honkan members* in addition to the cosmophysics group member of the KEK. The other is the CTA-Japan consortium. Also, I would like to thank Toshio Terasawa and Katsuaki Asano, and all members of the *High Energy Astrophysics Group* at ICRR who have helped me to develop the fundamentals of astrophysics in my Master course.

As a graduate student, I spent really a happy school life. Let me thank all the researches I have met in workshops, conferences, seminars and so on. Interactions in such sophisticated communities are really impressive for me and also highly motivative. Finally, I would like to thank my family and friends who have continuously encouraged me to go my way.

Appendix A

Symbols and acronyms

A.1 Symbols

Table A.1: Physical constants

c	$2.99792458 \times 10^{10}$cm/s	speed of light
m_e	511keV = 9.109×10^{-31} g	electron mass
$\hbar$	1.0546×10^{-27} cm^2/g/s	Planck's constant
$M_{\rm pl}$	1.12211×10^{19} GeV	Planck mass
G	6.673×10^{-8} cm^3/g/s^2	Newton's constant
σ_T	6.6524×10^{-25} cm^2	Thomson cross-section
$M_\odot$	1.989×10^{33} g	solar mass

A.2 Acronyms

Table A.2: A list of the acronym used in this thesis.

ALP	axion-like particle
CMB	cosmic microwave background
CTA	Cherenkov Telescope Array
Dec	declination
DM	dark matter
dSph	dwarf spheroidal galaxy
G.C.	galactic center
IACT	imaging atmospheric Cherenkov telescope
IGRB	isotropic γ-ray background
IRF	instrumental response function
LMC	Large Magellanic Cloud
l.o.s	line of sight
LSP	the lightest supersymmetric particle
LST	Large-sized telescope
MST	Medium-sized telescope
PBH	primordial black hole
R.A	right ascension
RoI	region of interest
SIMP	strongly interacting massive particle
SST	Small-sized telescope
WIMP	weakly interacting massive particle

Appendix B

Cosmological history

B.1 Brief summary

In this section, we briefly summarize the cosmological history. Throughout the section, we use the convention of $c = \hbar = k_B = 1$. More detailed explanations are provided in [349]. We pick up some topics related to this thesis here.

Cosmological observations revealed that the Universe is expanding. This indicates that it was very small and dense at early times. If we go back in time, the temperature and the density get higher. At some epoch, both the quantity exceed the energy scale which is achievable on the Earth. The hints of the early universe are obtained only from the cosmological observations. Observationally, the current Universe is very flat, isotropic and homogeneous. One has to consider the expansion history to understand the structure of the current Universe.

The evolution of the universe is described with the Einstein's equation. It is an equation that relates the energy and the geometry of the spacetime

$$G^{\mu}_{\nu} = 8\pi G T^{\mu}_{\nu}. \tag{B.1.1}$$

G^{μ}_{ν} in the left-hand side is the Einstein tensor determined by the geometrical structure of the spacetime while the T^{μ}_{ν} in the right-hand side is the energy-momentum tensor. Assuming that the universe is homogeneous and isotropic, the simplest metric of the flat spacetime is

$$ds^2 = -c^2 dt^2 + a(t)^2 \left(dr^2 + r^2 \left(d\theta^2 + \sin^2 \theta d\phi^2 \right) \right). \tag{B.1.2}$$

The scale factor $a(t)$ parametrize the expansion of the universe, or equivalently we use the redshift z defined as $a = (1+z)^{-1}$. Under this metric the, energy-momentum tensor is limited

to be the form of

$$T^{\mu}_{\nu} = \begin{pmatrix} -\rho & 0 & 0 & 0 \\ 0 & p & 0 & 0 \\ 0 & 0 & p & 0 \\ 0 & 0 & 0 & p \end{pmatrix} \tag{B.1.3}$$

where ρ and p is the energy density and pressure, respectively. The structure of Eq. (B.1.1) allows to add a constant term in either side of the equation. Then, Eq. (B.1.1) is rewritten as

$$G^{\mu}_{\nu} + \Lambda\delta^{\mu}_{\nu} = 8\pi G T^{\mu}_{\nu}. \tag{B.1.4}$$

If we move the Λ term to the right-hand side, it behaves as an energy component. All the energy component, including the Λ term, contribute to the evolution of the universe. So ρ in Eq. (B.1.3) is

$$\rho = \sum_i \rho_i. \tag{B.1.5}$$

The index i runs over all the energy components. The pressure p is determined by the property of each energy component. We consider three components: dust ($p = 0$), radiation($p = \rho/3$), and the so-called dark energy ($p = -\rho$).

From the conservation of the energy and momentum, and also from the Bianchi identity, Eq. (B.1.4) is reduced to two independent equations

$$\left(\frac{\dot{a}}{a}\right)^2 = \frac{8\pi G}{3}\rho + \frac{\Lambda}{3} = \frac{8\pi G}{3}\left(\rho + \frac{\Lambda}{8\pi G}\right) \tag{B.1.6}$$

$$\frac{\ddot{a}}{a} = -\frac{4\pi G}{3}(\rho + 3p) + \frac{\Lambda}{3}, \tag{B.1.7}$$

assuming an isotropic and homogeneous spacetime. In this expression, we separate Λ term from the other energy components. It is clear in Eq. (B.1.6) that the additional term of Λ behaves as an energy component. The first equation is called the Friedmann equation. We omit the negligible contribution from the curvature in this expression. There are three unknown quantities a, ρ, and p, and two independent equations. By combining the above equation with the equation of state $p = \gamma\rho$ for each component, we can solve the evolution of the spacetime. The behavior of the Universe at a certain epoch is almost determined by the most dominant component ρ_i at that stage.

In order to explain the observational facts that the Universe is flat and homogeneous, we need a rapid expansion epoch in the early time. This can be achieved if the Universe is dominated by dark energy at the beginning. This epoch is referred to as the *inflation*. The source of the inflation is called the inflaton. At the inflation, the scale factor grows as $a(t) \propto \exp\left[\sqrt{\Lambda/3}t\right]$ hence the Universe expands exponentially. Radiation dominated era appears when the inflaton decays into radiations. Density fluctuations, which are seeds

of the current structure of the Universe, are also generated in this mechanism. In the radiation-dominated era, the Universe expands as $a(t) \propto t^{1/2}$. Since the radiation energy density decreases as $\rho_r \propto a^{-4}$ while the matter as $\rho_m \propto a^{-3}$, the contribution from the matter-energy becomes dominant in the later stage. The Universe is matter-dominated after the matter-radiation equality. In this epoch, the Universe expands as $a \propto t^{2/3}$. Throughout the cosmological history, dark energy density keeps a small but constant value. It becomes dominant at a sufficiently late time because it could not be diluted. Our era is a dark-energy dominated era in which matter and radiation density are already rarefied to be subdominant.

The Hubble parameter, denoted as $H = \dot{a}/a$ is an important quantity to parametrize the evolution of the Universe. It can be derived from Eq. (B.1.6). If we take the value at the redshift $z = 0$, it corresponds to the expansion rate of the current Universe. Once the Hubble parameter is fixed, the total energy density ρ is expressed as

$$\rho_{\rm crit} = \frac{3H^2}{8\pi G}. \tag{B.1.8}$$

The $\rho_{\rm crit}$ is referred to as the critical density. It is convenient to introduce cosmological parameters Ω_i for each energy component defined as

$$\Omega_i = \frac{\rho_i}{\rho_{\rm crit}}. \tag{B.1.9}$$

The latest measurement of $\rho_{\rm crit}$ and Ω_i are given in [17].

Since the expansion of the Universe is an adiabatic process, the temperature decreases monotonically. When the temperature of the Universe is high enough, the timescale of the particle interaction is shorter than the Hubble time $H(t)^{-1}$, which is an indicator of the expansion speed of the Universe, the thermal equilibrium is sustained. Particles in the thermal equilibrium follows the distribution of

$$f(\mathbf{p}) = \left(\exp\left[\frac{E(\mathbf{p}) - \mu}{T} \pm 1 \right] \right)^{-1}. \tag{B.1.10}$$

where $\mathbf{p}$, μ and T is the momentum, chemical potential, and the temperature, respectively. The sign + is taken for fermions and the − for bosons. Using the distribution function Eq. (B.1.10), the number density, the energy density, and the pressure are

$$n = g \int \frac{d^3p}{(2\pi)^3} f(\mathbf{p}) \tag{B.1.11}$$

$$\rho = g \int \frac{d^3p}{(2\pi)^3} E(\mathbf{p}) f(\mathbf{p}) \tag{B.1.12}$$

$$p = g \int \frac{d^3p}{(2\pi)^3} \frac{p^2}{3E(\mathbf{p})} f(\mathbf{p}) \tag{B.1.13}$$

introducint g to be the internal degree of freedom. Asymptotic expressions are available for each of the non-relativistic and relativistic limit. In the non-relativistic limit,

$$n = g\left(\frac{mT}{2\pi}\right)^{3/2} \exp\left[-\frac{mc^2-\mu}{T}\right] \tag{B.1.14}$$

$$\rho = nmc^2 + \frac{3}{2}nT, \tag{B.1.15}$$

$$p = nT \tag{B.1.16}$$

while in the relativistic limits

$$n = \frac{1.202}{\pi^2}Tsg \times \begin{cases} 3/4 & \text{for fermion} \\ 1 & \text{for boson} \end{cases} \tag{B.1.17}$$

$$\rho = \frac{pi^2}{30}T^4 g \times \begin{cases} 7/8 & \text{for fermion} \\ 1 & \text{for boson} \end{cases} \tag{B.1.18}$$

$$p = \frac{\rho}{3}. \tag{B.1.19}$$

The non-relativistic and the relativistic limits corresponds to the matter and the radiation, respectively.

The total energy density in the radiation-dominated era is

$$\rho_r = \frac{\pi^2}{30}T^4 g_* \tag{B.1.20}$$

with the effective degree of the freedom g_* defined as

$$g_* = \sum_{\text{b:boson}} g_b \left(\frac{T_b}{T}\right)^4 + \frac{7}{8}\sum_{\text{f:fermion}} g_f \left(\frac{T_f}{T}\right)^4. \tag{B.1.21}$$

The contributions from both of the boson and the fermion are counted in this expression. In this era, the temperature T is same as the photon temperature. The entropy density is

$$s = \frac{\rho + p}{T} = \frac{2\pi^2}{45} g_{*,s} T^3. \tag{B.1.22}$$

Note that the effective degrees of freedom for the entropy $g_{*,s}$ is different from that for the energy, g_* as

$$g_{*,s} = \sum_{\text{b:boson}} g_b \left(\frac{T_b}{T}\right)^3 + \frac{7}{8}\sum_{\text{f:fermion}} g_f \left(\frac{T_f}{T}\right)^3. \tag{B.1.23}$$

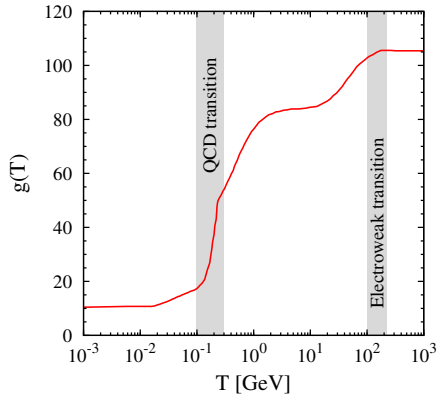

Figure B.1: The evolution of the effective degree of freedom in the radiation dominated era [38]. The right regions correspond to the early Universe. At the epoch of two shaded regions in the figure, there might be $\lesssim 10\%$ uncertainties. At other regions, the accuracy is a few %.

The entropy of the Universe is conserved except for some special situations. Then the temperature of the universe behaves as $T \propto g_{*,s}^{-1/3} a^{-1}$. The change of the effective degree of freedom is subtle as shown in Fig. B.1. they do not differ by more than two orders-of-magnitude while the temperature changes in six orders-of-magnitude. So the relation $a \propto T^{-1}$ holds as a good approximation.

The changes in the effective degrees of freedom seen in Fig. B.1 is an outcome of the particle annihilation in the Universe. At a high temperature of $T \gtrsim 300$GeV, all the standard model particles are relativistic and sharing the same thermal bath. The electroweak symmetry breaks at $T \sim 200$GeV then particles other than the gluon and the photon become massive. Creation of the weak bosons ($W^{\pm}$, Z) stops at $T \sim 100$ GeV. They could not be produced at $T \lesssim 100$ GeV. Weak bosons interact with other particles only through the decay into leptons and quarks. A heavier particle stops its creation earlier than a lighter one. The effective degree of freedom g_* decreases continuously in this process. The quark-hadron phase transition should occur at $T \sim 15 - 200$ MeV. After this phase transition, proton (p), neutron (n), photon (γ), electron and positron ($e^{\pm}$), and neutrino (ν) remain. The value of the g_* is fixed at $T \sim 0.5$MeV. No particle creation occurs after this time when electrons and positrons become non-relativistic.

The contribution from the non-relativistic matter to the total energy increases as the number of the relativistic species decreases. Using the scaling of $\rho_r \propto a^{-4} \propto T^4$ and $\rho_m \propto a^{-3} \propto T^3$, the energy density of two components becomes equal at $T \sim$ eV, i.e.,

$$T_{\rm eq} = 8.526 \times 10^3 \ \ {\rm K}, \tag{B.1.24}$$

or equivalently,

$$a_{\rm eq} = 3.196 \times 10^{-4}, \tag{B.1.25}$$
$$1 + z_{\rm eq} = 3.129 \times 10^{3}. \tag{B.1.26}$$

After the matter-radiation equality, the Universe is matter-dominated. In this epoch, electrons are free and interact with photons through the Thomson scattering. Also, they are interacting with protons through the process of

$$p + e^- \leftrightarrow \gamma + \mathrm{H}. \tag{B.1.27}$$

The reaction in Eq. (B.1.27) proceed in both directions. When the temperature becomes lower than $T \sim 0.3$ eV, which is much below the ionization energy of the hydrogen of 13.6 eV, the reaction from the right to the left in Eq. (B.1.27) stops. Electrons are captured by protons to form neutral hydrogens then the Universe becomes neutral. This is the *recombination*. The recombination occurs at

$$T_{\rm rec} \simeq 3500 \ \mathrm{K} \tag{B.1.28}$$
$$z_{\rm rec} \simeq 1300. \tag{B.1.29}$$

After the recombination, the number density of the free-electron decreases rapidly. Then the interaction between electrons and photons stops., i.e., the *decoupling* of the photon occurs. The temperature and the redshift of the Universe at the decoupling are

$$T_{\rm dec} \simeq 3000 \ \mathrm{K} \tag{B.1.30}$$
$$z_{\rm dec} \simeq 1100. \tag{B.1.31}$$

After the decoupling, photons propagate in straight paths. We see the last-scattered photon as the cosmic microwave background (CMB). The structure formation occurs after the photon decoupling as we explain in below. Table B.1 is a brief summary of the cosmological event after the inflation [349, 350].

There are lots of structures in the Universe. The initial density fluctuation is the seed of the structure of the Universe. It evolves through the gravitational interaction and forms the current Universe. This is described in the framework of the general relativity. However, a Newtonian discussion is sufficient to capture the qualitative behavior of the structure formation. Considering the equation of the mass conservation and the Euler's equation in a co-moving frame of the expanding universe, the density and velocity fields evolve as

$$\frac{\partial \rho}{\partial t} + 3\frac{\dot{a}}{a}\rho + \frac{1}{a}\nabla \cdot (\rho \mathbf{v}) = \mathbf{0} \tag{B.1.32}$$
$$\frac{\partial \mathbf{v}}{\partial t} + \frac{\dot{a}}{a}\mathbf{v} + \frac{1}{a}(\mathbf{v} \cdot \nabla)\mathbf{v} = -\frac{1}{a}\nabla\Phi - \frac{1}{a\rho}\nabla p \tag{B.1.33}$$

Table B.1: Thermal history of the Universe.

time [s]	temperature [GeV]	event
		inflation and reheating
10^{-12}	1 TeV	Electroweak phase transition ($\sim$ 100 GeV)
		top quark, $W^{\pm}$ boson, Z boson annihilation
		bottom quark, $\tau^{\pm}$ particle, charm quark annihilation
10^{-6}	1 GeV	quark-hadron transition ($\sim$ 0.1 GeV)
10^{-4}	0.1 GeV	$\mu^{\pm}$ particle annihilation
0.1	2-3 MeV	neutrino decoupling
1	0.5 MeV	$e^{\pm}$ pair annihilation
100	0.1 MeV	Big-Bang nucleosynthesis ($\sim$ 0.07 MeV)
10^{3}	10 eV	matter-radiation equality
10^{13}	0.3 eV	reionization
10^{13}	0.2 eV	photon decoupling
10^{16}		galaxy formation (continues)
10^{17}	10^{-4} eV	today

where Φ is the gravitational potential in the co-moving frame. In order to see the evolution of the density fluctuations, we decomposing the quantities into the average and the small perturbation as

$$\delta(\mathbf{x}, t) = \frac{\rho(\mathbf{x}, t) - \bar{\rho}(t)}{\bar{\rho}(t)} \tag{B.1.34}$$

$$\delta p(\mathbf{x}, t) = p(\mathbf{x}, t) - \bar{p}(t) \tag{B.1.35}$$

where barred components correspond to the averages. It is convenient to work in the Fourier space when we solve the evolution. We assume a self-gravitating system with no entropy perturbations, which is the simplest case. The equation of motion for the Fourier component $\tilde{\delta}(\mathbf{k}, t)$ is

$$\frac{\partial^2 \tilde{\delta}}{\partial t^2} + 2\frac{\dot{a}}{a}\frac{\partial \tilde{\delta}}{\partial t} - \left(4\pi G\bar{\rho} - \frac{c_s^2 k^2}{a^2}\right)\tilde{\delta} = 0. \tag{B.1.36}$$

The second term in Eq. (B.1.36) coming from the expansion of the universe work as friction in the equation of motion. If the third term is negative, $4\pi G\bar{\rho} - (c_s k)^2/a^2 \leq 0$, the equation is the same as that of a damped oscillation. This is a so-called acoustic oscillation. On the other hand, if $4\pi G\bar{\rho} > (c_s k)^2/a^2$, the perturbation $\tilde{\delta}$ grows. The critical wavenumber k_J is

$$k_J = \frac{a\sqrt{4\pi G\bar{\rho}}}{c_s}. \tag{B.1.37}$$

This is referred to as the Jeans wavenumber. Only longer scale perturbations of $l \geq \lambda_J = 2\pi a/k_J$ can evolve. We can estimate the minimum mass of the gravitationally-formed object from this condition that

$$M_J = \frac{4\pi}{3}\left(\frac{\lambda_J}{2}\right)^3 \bar{\rho}. \tag{B.1.38}$$

Before the matter-radiation equality, the perturbation could not grow due to the radiation pressure. The Jeans length is equal to the horizon scale in this case. The growth of the perturbation starts when the Universe enters the matter-dominated era. However, baryons are tightly coupled to the photons through the Thomson scattering. Then the evolution of the baryon is suppressed due to the photon pressure. It starts to evolve after the photon decoupling. The Jeans mass at the decoupling is estimated to be

$$M_J \sim \frac{\pi^{5/2}}{6\sqrt{G^3\rho_b}}\left[c_s\left(\frac{3\rho_b}{4\rho_r}\right)^{-1/2}\right]^3 \to 1.9\times 10^{16} M_\odot, \tag{B.1.39}$$

which corresponds to the mass scale of the largest structures in the current Universe. We do not have smaller structures like galaxies if this is the case. This problem can be solved by introducing dark matter, of which perturbation starts to evolve just after the matter-radiation equality. Their coupling to the photon must be small to satisfy the requirement.

B.2 The canonical cross-section

As we have explained in the previous section, we need dark matter, i.e., non-relativistic and non-baryonic component in the Universe to form small-scale structures. Weakly Interacting Massive Particle (WIMP) is a strong candidate. Based on the thermodynamics in an expanding spacetime, we summarize the derivation of the canonical cross-section for the annihilation process of WIMP dark matter into the standard model particles [38]. We only consider the velocity-independent case and discuss the thermally-averaged annihilation-cross section $\langle\sigma v\rangle$ here.

As a rough estimate, the decoupling of the particle occurs when their interaction rate becomes smaller than the expansion rate of the Universe. This is a so-called Gamow's criteria. The WIMP dark matter is initially in the thermal equilibrium with photons, i.e., the timescale of the WIMP-photons interaction is shorter than the Hubble time. The evolution of their number density n is described with the following equation

$$\frac{dn}{dt} + 3Hn = \langle\sigma v\rangle\left(n_{\rm eq}^2 - n^2\right). \tag{B.2.1}$$

The second term in the left-hand side corresponds to the expansion of the Universe. When the interaction rate is high enough, the number density n follows the thermal distribution $n_{\rm eq}$. Then the right-hand side of the equation becomes zero and

$$n(t_f) = n(t_i) \exp\left[-3 \int_{t_i}^{t_f} H(t) dt\right] \tag{B.2.2}$$

hence the number density is expected to decrease due to the Hubble expansion. The value of $n_{\rm eq}$ is determined as

$$n_{\rm eq} = \begin{cases} 1.202 \times \frac{3}{4\pi^2} g_\chi T^3 & (m \ll T, \ \text{relativistic}) \\ g_\chi \left(\frac{mT}{2\pi}\right)^{3/2} \exp\left[-\frac{m}{T}\right] & (m \gtrsim T, \ \text{non} - \text{relativistic}) \end{cases} \tag{B.2.3}$$

using Eq. (B.1.17) or (B.1.14). If the particle is non-relativistic, the number density decreases exponentially as m/T increases. It is convenient to re-write Eq. (B.2.1) with different variables $Y = n/s$ and $x = m/T$. We introduce the entropy density s defined as $s = S/a^3$. The effective degree of freedom for the entropy $g_{*,s}$ is defined in Eq. (B.1.23). Using these variables, Eq. (B.2.1) becomes

$$\frac{dY}{dx} = \frac{s \langle \sigma v \rangle}{Hx} \left[1 + \frac{1}{3} \frac{d \ln g_{*,s}}{d \ln T}\right] \left(Y_{\rm eq}^2 - Y^2\right). \tag{B.2.4}$$

Eq. (B.2.4) can be solved analytically in two asymptotic regime, the early and the late time limits.

At the early time of the evolution, the relation $n_{\rm eq} \simeq n$ holds. Then expanding the variable Y to $Y = (1 + \Delta) Y_{\rm eq}$, Eq. (B.2.4) becomes

$$\frac{d \ln(1 + \Delta)}{d \ln x} + \frac{d \ln Y_{\rm eq}}{d \ln x} = -\frac{Y_{\rm eq} s \langle \sigma v \rangle}{H} \left[1 + \frac{1}{3} \frac{d \ln g}{d \ln T}\right] \frac{\Delta(2 + \Delta)}{1 + \Delta}. \tag{B.2.5}$$

Using the fact that $Y_{\rm eq} \propto g x^{3/2} \exp[-x]$, it is the same as

$$\frac{\Delta(2 + \Delta)}{1 + \Delta} = \frac{x - \frac{3}{2} - \frac{d \ln g}{d \ln T} - \frac{d \ln(1+\Delta)}{d \ln x}}{\frac{Y_{\rm eq} s \langle \sigma v \rangle}{H} \left[1 + \frac{1}{3} \frac{d \ln g}{d \ln T}\right]}. \tag{B.2.6}$$

The third and forth terms are negligible when $\Delta \ll 1$ and $d\Delta/dx \ll 1$. The change of g in the denominator can also be neglected. In this regime, Δ is obtained by solving

$$\frac{\Delta(2 + \Delta)}{1 + \Delta} \sim 1.25 \times 10^{-35} \sqrt{g} \langle \sigma v \rangle^{-1} \left(\frac{m}{\rm GeV}\right)^{-1} \left(\frac{(x - 3/2) e^x}{x^{1/2}}\right). \tag{B.2.7}$$

The approximation breaks when $\Delta = O(1)$. The breaking time $x_* = m/T_*$ defined as $\Delta(x_*) = 1$ is obtained by solving the following equation

$$x_* + \ln(x_* - 1,5) - 0.5 \ln x_* = 20.5 + \ln(10^{26} \langle\sigma v\rangle) + \ln m - 0.5 \ln g_*. \tag{B.2.8}$$

The x_* mildly depends on the particle mass m. If m =100MeV - 10TeV, then x_* varies from ~ 17 to ~ 24. The value monotonically increases with the particle mass.

When the deviation from the thermal equilibrium becomes significant, $\Delta \gtrsim O(1)$, the exponential growth of the Δ starts. The number density of the particle is much larger than that at the equilibrium, $Y \gg Y_{\rm eq}$, at this stage. Eq. (B.2.4) becomes

$$\frac{dY}{dx} = -\frac{s \langle\sigma v\rangle}{Hx} \left[1 + \frac{1}{3} \frac{d \ln g}{d \ln T}\right] Y^2. \tag{B.2.9}$$

We can determine the number density at the final time n_f by integrate Eq. (B.2.9) from x_* to $x_f = m/T_f$. The solution is

$$Y_f = \frac{n_f}{s_f} = Y_* \left(1 + \frac{\langle\sigma v\rangle n_*}{H_*} \alpha_*\right)^{-1} \tag{B.2.10}$$

where

$$\alpha_* = \int_{T_f}^{T_*} \frac{dT}{T_*} \sqrt{\frac{g}{g_*}} \left[1 + \frac{1}{3} \frac{d \ln g}{d \ln T}\right]. \tag{B.2.11}$$

The final temperature T_f is same as the temperature of the current Universe.The cosmological parameter of the WIMP dark matter is

$$\Omega_{\rm DM} = \frac{8\pi G}{3H_0^2} \left(\frac{m H_* s_0}{\langle\sigma v\rangle s_*}\right) \cdot K \tag{B.2.12}$$

where

$$K = \frac{n_* \langle\sigma v\rangle}{H_* + n_* \alpha * \langle\sigma v\rangle} \tag{B.2.13}$$

and $n_* = Y_* s_*$ by definition. K varies from 0.97 to 1.07 depending on the mass of the dark matter. The dark matter density in the current Universe is also written as

$$\Omega_{\rm DM} = \frac{\rho_{\rm DM,0}}{\rho_{\rm crit,0}} = \frac{m Y_0 s_0}{\rho_{\rm crit,0}}. \tag{B.2.14}$$

The suffix 0 refers to the current value. Rewriting Eq. (B.2.12) using $x_* = m/T_*$ and $H = H(T)$, we obtain the annihilation cross-section $\langle\sigma v\rangle$:

$$\langle\sigma v\rangle = 0.902 \times 10^{-26} x_* g_*^{-1/2} \left(\frac{\Omega_{\rm DM}}{0.11}\right)^{-1} K. \tag{B.2.15}$$

Fig. B.2 shows that the canonical cross-section depends on the mass of the dark matter [38].

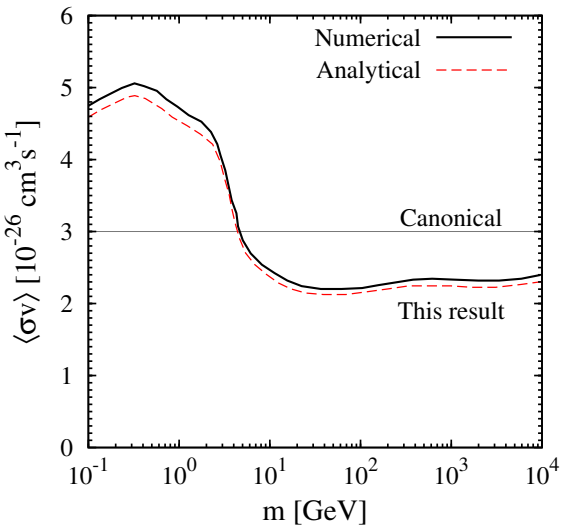

Figure B.2: The canonical cross-section of WIMP dark matter [38]. They have confirmed their analytical calculation (red-dashed line) with a numerical calculation (black-solid line). For lower mass dark matter of $m_{\rm DM} \lesssim 1$ GeV, the annihilation cross-section becomes higher by a factor of ~2 compared to the heavier dark matter.

Appendix C

Constraints from the collider and direct detection experiments

C.1 Collider experiments

High-energy environments which are similar to some points at the early Universe can be produced inside the collider. We might see processes similar to the inverse of the thermal-freeze out there. The coupling between dark matter and the standard model sector should be very weak then we do not expect to see dark matter as products of the particle collision. It is mainly searched through the measurements of the missing transverse momentum or energy. The so-called "mono-X" search is a strategy which investigates the excess of a certain final state X in the opposite direction of the large missing transverse momentum or energy. Analyses are also conducted for channels that produce something decay into the standard model particles and dark matters. In the latter search, the final state is more complex than that of the former one.

We have to assume the "model" when we search dark matter signature in the collider. Following the classification in [351], dark matter search in the collider is categorized into the three:

- Effective field theory approach
- Simplified model approach
- complete dark matter model approach

The simplest strategy is the *effective field theory approach*. In this approach, dark matter is assumed to be in a unique final state within the accessible region. An example process is (e.g. [352])

$$q\bar{q} \rightarrow Z/\gamma^* \rightarrow \gamma\chi\bar{\chi}. \tag{C.1.1}$$

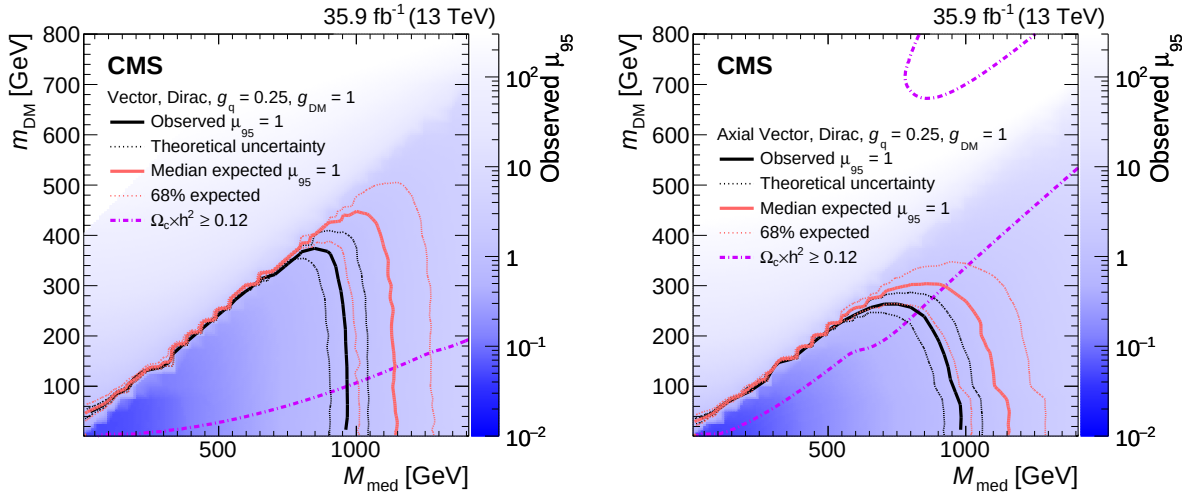

Figure C.1: Constraints in the $m_{\mathrm{DM}} - m_{\mathrm{med}}$ plain [353]. In the *left* (*right*) panel, a vector-mediator (an axial-vector mediator) is assumed. In this analysis, coupling strength of the mediator to the standard model particles, as well as to the dark matter particle, is fixed. Regions below the black lines are excluded. The region below the magenta lines in both panels and the top regions in the right panel are excluded from cosmological requirement $\Omega_{\mathrm{DM}}h^2 \leq 0.12$.

This enables us to limit the scale where the new physics appears. Also, it makes comparisons with the results of direct and/or indirect detection experiments easier. However, it is not assured whether the effective field theory holds or not at the energy scale of the experiments.

The *simplified theory approach* is a more sophisticated and complicated one which solve the problem in the effective field theory approach. Introducing the mediator of dark matter and the standard model sector, we can describe the contact interaction between the two sectors. The number of model parameter is larger than that of the effective field theory approach, hence the analysis becomes more difficult.

The latest results obtained in this approach are shown in Fig. C.1. CMS collaboration searched dark matter signals in the simplified model approach, as well as the effective field theory approach, using $\sqrt{s}$ = 13TeV proton-proton collision data of the LHC [353]. Similar analyses were also conducted by the ATLAS collaboration [354]. Their results show reasonable agreements. In the effective field theory approach, they have found no signatures of the deviation from the standard model predictions. In terms of the simplified field theory approach, corresponding constraints are obtained in the plain of the dark matter mass m_{DM} and the mediator mass m_{med}. The limits shown in the m_{DM} - m_{med} plain can be converted to the constraints on the scattering cross-section between the dark matter particle and nuclei

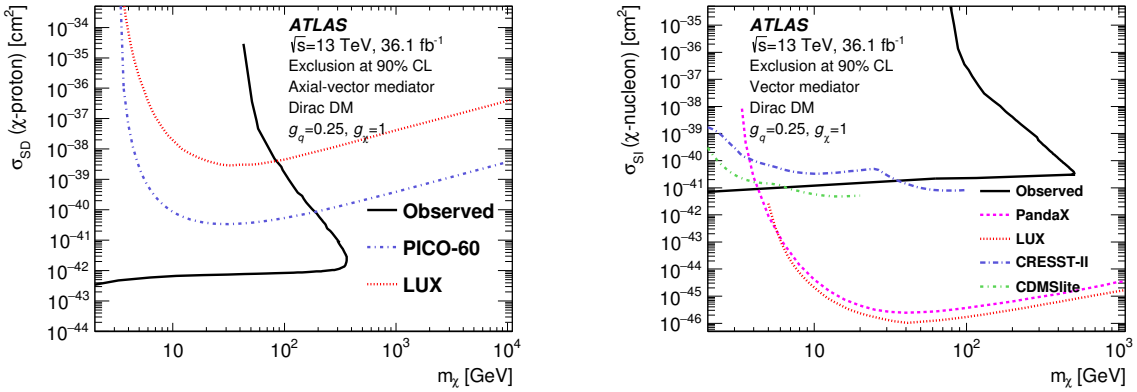

Figure C.2: Constraints on the scattering cross-section between the dark matter particle and nuclei [354]. The *left* panel shows the results for the spin-dependent cross-section between dark matter particles and protons. An axial-vector is assumed as the mediator. The *right* panel is for the spin-independent cross-section, assuming a vector mediator between two sectors. In each panel, the left-side regions of the black contours are excluded. Thin lines with colors are results obtained by direct detection experiments.

following the prescription in [355]. Fig. C.2 is an example of comparison between the results of collider and direct detection experiments [354]. One example case comparing the ATLAS results with those of direct detections is shown in Fig. C.2. They derive the constraints in Fig. C.2 assuming the model of [355]. Note that the comparison between different types of dark matter search is always model dependent [356].

The *complete dark matter model approach*, which specify the whole structure of the dark matter and the standard model sector, is the most complicated one. In this approach, we can properly treat the correlation between the observables which could not be addressed in the simplified approach. However, the number of the model parameter is huge and varieties of phenomena are expected. It is almost impossible to derive the property of the dark matter sector solving the degeneracy. The minimal supersymmetric extension of the standard model (MSSM) is such an example. Four gaugino particles appears in the MSSM, $(\tilde{\chi}_1^0, \tilde{\chi}_1^+, \tilde{\chi}_1^-, \tilde{\chi}_2^0)$. Analyses can be done by assuming the electrowikino pair-production from the proton-proton collision for example. After the collision, they successively decay into the lightest SUSY particles $\tilde{\chi}_1^0$ and W/Z bosons. The lightest SUSY particle $\tilde{\chi}_1^0$ is regarded as the WIMP in the main text. ATLAS [357] and CMS [358] collaboration respectively search signals of SUSY particles. The constraints are obtained in the $m_{\tilde{\chi}_1^0}$ -$m_{\tilde{\chi}_1^\pm/\tilde{\chi}_0^2}$ plain assuming that the next-to-the-lightest states $\tilde{\chi}_1^\pm$ and $\tilde{\chi}_2^0$ are degenerate. Fig. C.3 is the results obtained in [358]. Constraints obtained in several search channels are compared in this figure.

Recently, combined analyses of the ATLAS and CMS results are also performed [359].

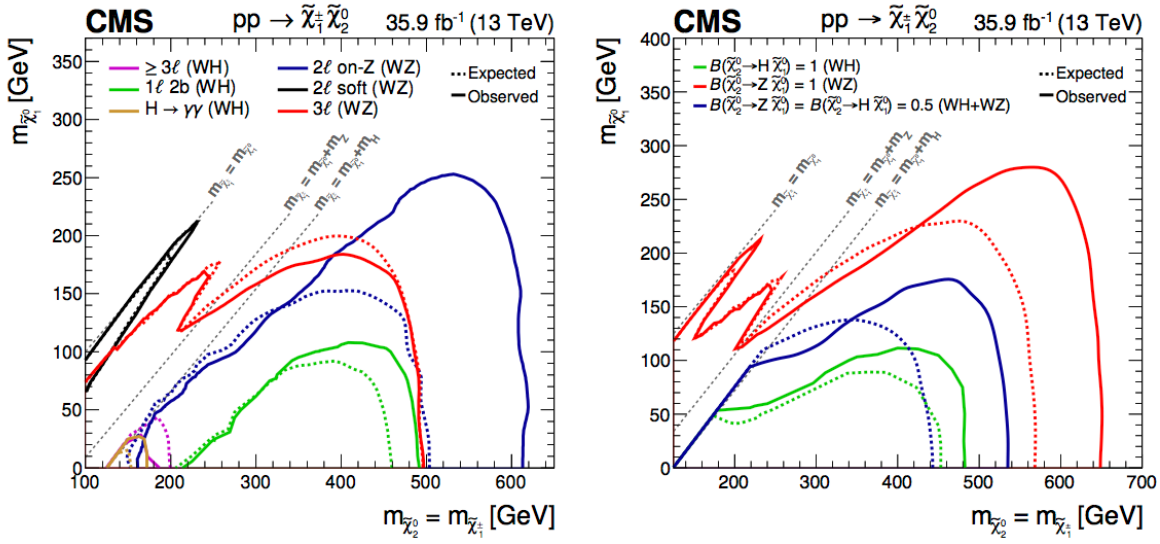

Figure C.3: Constraints in the mass plain of the gaugino, $\tilde{\chi}_1^0$ and $\tilde{\chi}_1^{\pm}/\tilde{\chi}_0^2$ [358]. The *left* panel corresponds to the individual analysis while the *right* one to the combined analysis. Depending on the possible decay channels and the event topologies, results slightly differs. The results shows good agreements with those obtained with ATLAS detector.

They derived the best-fit points of the likelihood analyses converting the model parameters to the relic abundance and/or the scattering cross-section between the dark matter and the nucleus. It is slightly below the observational limits obtained by the indirect or direct detection experiments (see Fig.15 of [359]). It may be possible that we find neutralino signatures in near-future indirect and/or direct detection experiments.

C.2 Direct detection experiments

C.2.1 method

In direct detection experiments, we directly measure the scattering between dark matter particles and nuclei (or electrons). The differential energy spectrum of the target recoiled by the dark matter particle is [360]

$$\frac{dR}{dE_R} = \frac{R_0}{E_0 r} \exp\left[-\frac{E_R}{E_0 r}\right] \tag{C.2.1}$$

denoting the total event rate with R_0. E_R and E_0 is the recoil and incoming dark matter energy, respectively. The kinematic factor r is defined as

$$r = \frac{4m_{\rm DM}m_N}{m_{\rm DM} + m_N} \tag{C.2.2}$$

where $m_{\rm DM}$ and m_N is the mass of the dark matter and the target nucleon. In the real measurement, modifications of Eq. (C.2.1) is needed due to the physical and practical reasons:

- the Earth (and the detector) is moving with a finite relative velocity to the dark matter particles,
- the detection efficiency of the nuclear recoil event is different from that of the electron recoil event, and always less than 1,
- the target is not a single object,
- the instrument and threshold effect appears,
- the amplitude of the spin-independent scattering is enhanced compared to the spin-dependent case due to the coherence effect,
- the form factor correction needs to be considered.

Hence it is better to rewrite the recoil spectrum by introducing the spectrum modification function $S(E)$, the form factor correction $F(E)$, and the interaction function for the spin-dependence I to

$$\left.\frac{dR}{dE}\right|_{\rm obs} = R_0 S(E) F(E)^2 I. \tag{C.2.3}$$

C.2.2 current limits

Numbers of direct detection experiments using different materials are under operations. The constraints obtained by XENON-1T [44], LUX [42], and PandaX-II [361] are similarly strong by each other at $m_{\rm DM} \gtrsim 5$ GeV. Those experiments use liquid xenon as the target. The constraints obtained by XMASS is slightly weaker [362, 363]. PICO-60 using a C_3F_8 bubble chamber also gives a milder upper limit in this mass range [43]. We can probe the lower mass regions down to $m_{\rm DM} \sim$ 1GeV by using liquid argon target [364] or germanium target [365]. CRESST-III experiments using $CaWO_4$ is sensitive to the dark matter as light as $m_{\rm DM} \sim 0.3$ GeV [366]. All of these experiments report the non-detection of the dark matter signals. Only the upper limits on the dark matter-nuclei scattering cross-section are obtained. However, DAMA/LIBRA collaboration has reported the detection of the annual modulation

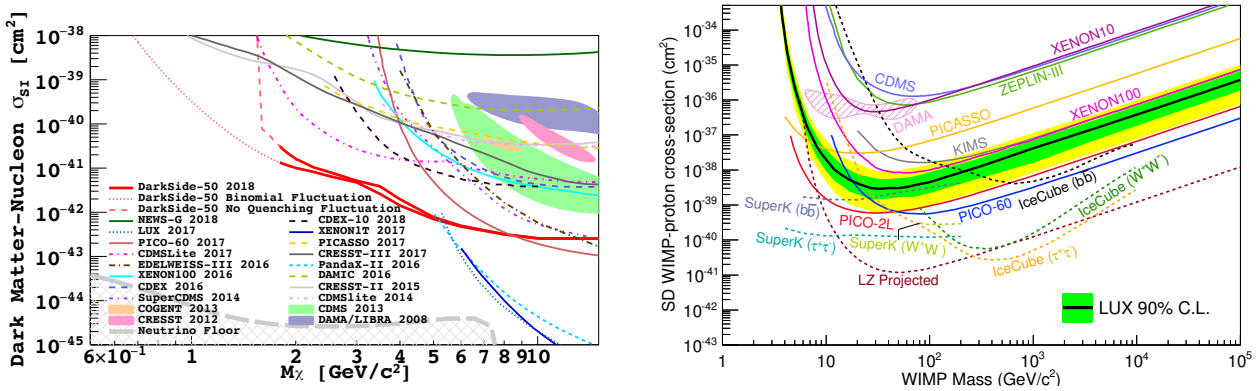

Figure C.4: Constraints on dark matter-nucleon scattering cross section. *Left* panel shows the upper limits on spin-independent scattering cross-section of dark matter and nucleus [364]. *Right* panel shows the upper limits of the spin-dependent cross-section for proton-dark matter scattering [376].

signal of the dark matter [367–369], which is in tension with the results of the other experiments. DAMA/LIBRA uses the NaI crystal as the target. Several new experiments using the same material have been launched in purpose of independent analyses [370–375].

The lower mass region is difficult to search since the incoming particle energy is so small that the nuclear recoil could not occur. The electron recoil event can be used to probe the dark matter in the low mass regions [377,378]. In electron recoil measurements, background rejection is further difficult compared to the nuclear recoil case. Recently, a new idea to use cosmic-rays scattered by dark matter around the Earth is proposed [379–381]. Constraints by this method are shown in Fig. C.5. Another new approach is a so-called paleo-detector search [382, 383]. In this strategy, tracks of the particle scattered by the dark matter are searched in the ancient minerals. Solar neutrinos or α-particles produced by the radioactive decay is the dominant background for the paleo-detector.

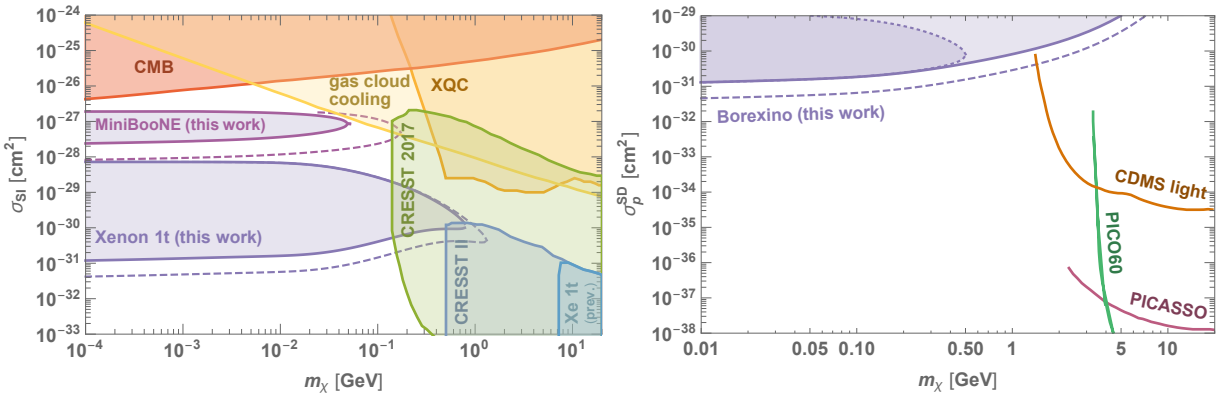

Figure C.5: Constraints on the spin-independent scattering cross-section for sub-GeV dark matter (*left*) and the spin-dependent cross-section with proton (*right*). Cosmic-rays kicked by dark matter particles are used as probes [380].

Appendix D

Detection principle of the high-energy γ-ray experiments

Depending on the energy of the incoming γ-ray, different methods are adopted in observations. γ-rays of energy $E_\gamma \lesssim O(1)$ TeV are measured with satellite. Higher energy γ-rays are detected with ground-based Cherenkov telescopes using their interaction in the atmosphere. The basic principle is described in [384].

D.1 Imaging atmospheric Cherenkov telescope (IACT)

In this section, we explain the method to detect high-energy γ-ray of $E_\gamma \gtrsim O(1)$ TeV. For details of the method, see [385, 386]. The γ-rays of energy $E_\gamma \gtrsim O(1)$ TeV are indirectly detected by measuring the *shower* they cause in the atmosphere. A shower initiates when the incoming γ-ray photon interacts with the electric fields of the nuclei in the Earth's atmosphere. Then an electron-positron pair is produced as

$$\gamma + p, n \to e^+ + e^-. \tag{D.1.1}$$

These electron and positron produce γ-rays through Bremsstrahlung emissions if their energy exceeds ~86 MeV. The reaction is repeated and particles are copiously produced. The energy loss of the electron or positron is described as

$$\frac{dE}{dx} = -\frac{E}{X_0^e} \tag{D.1.2}$$

with $X_0^e = 37.2\text{g/cm}^2$ is the attenuation length of electron. For γ-rays, attenuation length is $X_0^\gamma = (7/9)X_0^e$. Cherenkov lights are emitted when the propagation speed of the electron

(positron) v is larger than the speed of light in the atmosphere, c/n. n is the refractive index of the atmosphere. The condition for an electron to emit Cherenkov light is

$$E \geqq \frac{m_e c^2}{\sqrt{1-1/n^2}} \sim 21 \ \text{MeV}. \tag{D.1.3}$$

When this condition is satisfied, Cherenkov photons are emitted in the cone region of angle θ

$$\cos\theta = \frac{c}{vn(\lambda)}. \tag{D.1.4}$$

The refractive index $n(\lambda)$ depends on the wavelength. For photons of $\lambda \sim 300$ nm, $n(\lambda) \sim 1.00029$. Cherenkov photon from each particle is emitted in a ring region, and superposition of the rings by numbers of particles makes the circle region on the ground called *Cherenkov pool*. The number of the Cherenkov photons is given by [387]

$$\frac{d^2N}{d\lambda dx} = \frac{\alpha}{\hbar c}\sin^2\theta \simeq 370\sin^2\theta(\lambda) \ \text{eV}^{-1}\,\text{cm}^{-1}. \tag{D.1.5}$$

where $\alpha \sim 1/137$ is the fine structure constant. This is proportional to λ^{-2}. However, due to the attenuation caused by Rayleigh and Mie scattering, the peak comes around the UV wavelength ($\lambda = 300-500$ nm). If the incoming photon energy is E_γ=1 TeV, then the number density of the total Cherenkov photon is ~50 /cm^2. If the shower is initiated by a vertically incoming γ-ray photon, the number density of Cherenkov photon at the ground is almost constant within a ~120m circle [388].

The imaging technique is a method to collect Cherenkov photons generated by high-energy γ-ray photons with an array of large reflectors on the ground. The minimum energy of the detectable γ-ray is determined by the aperture of the reflector telescope. The Cherenkov light is very weak and observations are possible only in the dark and clear night without the moonlight. Any lights in the night sky are noises. More significant noises are incoming high-energy cosmic-ray protons. π-particles are produced in cosmic-ray interactions, and Cherenkov photons are emitted in the following processes:

$$\begin{aligned}
\pi^0 &\rightarrow 2\gamma \\
\pi^+ &\rightarrow \mu^+\nu_\mu \rightarrow e^+ + \nu_e + \bar{\nu_\mu} + \ldots \\
\pi^- &\rightarrow \mu^- + \bar{\nu_\mu} \rightarrow e^-\bar{\nu_e} + \nu_\mu + \ldots
\end{aligned}$$

Proton-induced showers are discriminated from the γ-ray induced ones by analyzing the morphology of the shower evolution (e.g. [388,389]). The proton-induced showers extend to larger radii from the shower axis while the γ-ray induced ones concentrate on the axis. Also,

Table D.1: Numbers of telescopes at each site. The latest information is available at https://www.cta-observatory.org/

	North (La Palma)	South (Paranal)
LST(20GeV-3TeV)	4	4
MST(80GeV-50TeV)	15	25
SST(1TeV-300TeV)	0	70

the photon density in the light pool decreases with the radius when the shower is produced by a proton. In another way, proton signals also separated by using the Cherenkov image at the camera. The incoming directions of the proton determined from the images are different from those of γ-rays. The Cherenkov image becomes elliptical if the incoming particle path is parallel to the optical axis of the telescope. The semi-major axis of the ellipse always crosses the optical axis. The γ-ray photons concentrate on the target direction while the background protons come randomly. The semi-major axis does not cross the optical axis in a proton-induced image.

Using two telescopes on the ground, the position of the γ-ray source is determined. The intersection of the semi-major axis of the image in each telescope points the target. The energy resolution of the measurement is also increased by observing with more than one telescope. The hight of the shower-initiation point is determined by the shower axis and the distance between the telescopes. Combining this information with the intensity of the Cherenkov emissions, a better estimate of the incoming γ-ray energy is achieved. The localization of the source is further improved by observing with multiple telescopes.

Adopting above-mentioned technique, CTA observes γ-rays from $O(10)$ GeV to $O(100)$ TeV. Three types of telescopes, the large-sized telescope (LST), the medium-sized telescope (MST), and the small-sized telescope (SST), are used. Numbers of telescopes are summarized in Table. D.1. We need to cover a larger Cherenkov pool for higher energy γ-ray photons. In this purpose, SST array is constructed in a 2400m-diameter circle. MST, which is an intermediate type of the LST and SST, is arrayed in a ~1000m circle. On the other hand for the lower energy γ-ray photons, we need to collect weak Cherenkov emissions. LSTs have 23m-dishes and to detect γ-rays as low-energy as $E_\gamma \sim 20$GeV. They are arrayed in a ~200 m circle. Because of its large dish size, we need to be careful about the light-travel time from the dish to the camera for LST. In order to minimize the time-difference between reflected lights from different points on the dish, CTA adopts a Parabolic telescope for an LST. For MST and SST, the modified Davies Cotton telescope is adopted because it shows a better aberration compared to the Parabolic telescope.

D.2 Satellite missions

Fermi satellite is the representative of the γ-ray mission in the space. It was launched in 2008 and is monitoring the whole sky continuously. The field of view of the *Fermi*-LAT (large area telescope) is 2.4 steradian. It detects γ-rays of 20 MeV $\leq E_\gamma \leq$ 300 GeV by measuring the interaction between γ-ray photons and the target material loaded on the satellite. The most dominant process of γ-ray interactions with materials at $E_\gamma \geq O(10)$ MeV is the electron-positron pair creation. When a γ-ray photon hits the material, it produces a pair of electron-positron with the interaction cross-section of

$$\sigma_{\gamma\to e^+e^-} = \frac{7}{9}\frac{A}{X_0} \times 6.02 \times 10^{23} \tag{D.2.1}$$

where X_0 is the radiation length (see [390] for detail). The radiation length is defined as

$$E(x) = E_0 \exp\left[-\frac{x}{X_0}\right]. \tag{D.2.2}$$

As is seen in Eq. (D.2.1), materials with high atomic numbers achieve good efficiencies. We track the produced electron-positron pairs to derive the incoming direction of γ-ray photons. After passing the layers of trackers, γ-ray energy is measured with the calorimeter set at the bottom of the equipment. In order to reject the backgrounds from charged cosmic-rays, the whole system of the tracker and the calorimeter is covered by the anti-coincidence detector. In this method, the minimum of the detectable γ-ray energy is determined by the pair-creation threshold. The higher energy end is determined by the size of the calorimeter. If the energy of the incoming γ-ray is high enough to go through the calorimeter, we only know the lower limit of the incoming energy.

A tracker of the *Fermi* satellite [235,391] is composed of a tungsten converter and 2-layers of single-sided strip detectors. Incoming γ-rays are converted to electron-positron pairs. The electrons and positrons produce pass the silicon strip detector. Electron-hole pairs are produced along with their paths in the silicon-strip. They are collected by the attached anode and/or cathode. The large area telescope (LAT) detector of the *Fermi* satellite tracks the electrons and positrons by layering the system and determine the incoming direction of γ-ray photons. At the bottom of the 18 layers of converters and silicon strips, a CsI calorimeter is installed. LAT's calorimeter measures the total deposited energy and also takes the image of electron- and/or positron-induced showers. Information about the shower development is used to discriminate signals from the background events. Calorimeters are arranged in 8 layers of 12 CsI crystals. Fig. D.1 shows the angular and energy resolution of *Fermi*-LAT.

The angular resolution of the instrument is limited by (i) the uncertainties in the emission angle of the electron-positron pair at the converter, (ii) the accuracy of the tracking, and (iii)

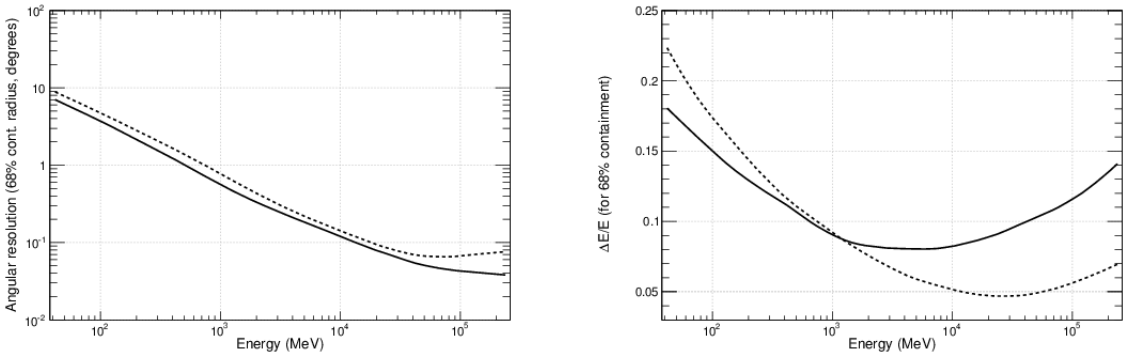

Figure D.1: The angular (*left*) and the energy (*right*) resolution of the *Fermi*-LAT. Energy is measured in units of MeV. In each panel, the solid line corresponds to the nominal (on-axis) observations while the dashed one to the 60° off-axis case. The angular resolution is $\sim$ 3.5 degrees at E_γ=100 MeV and 0.6 degrees at 1GeV. It is finer than 0.15 degrees at $E_\gamma \geq 10$ GeV. The typical energy resolution for an on-axis observation is $\sim$ 8 to $\lesssim$ 20 %. The best energy resolution is achieved at E_γ=1-10 GeV [235].

the multiple Coulomb scattering in the tracker. The uncertainty of the emission angle (i) is given by [384]

$$\left\langle \theta^2 \right\rangle^{1/2} = Q(E_\gamma, E_{e^\pm}, Z) \left(\frac{E_\gamma}{511\mathrm{keV}} \right)^{-1} \ln \left[\frac{E_\gamma}{511\mathrm{keV}} \right]. \tag{D.2.3}$$

where Z is the atomic number of the target. Q is a $O(1)$ factor that depends on the ratio of the electron (positron) and the γ-ray photon energies.

Appendix E

List of dwarf spheroidal galaxies

On-going survey missions continuously report the discovery of new small-sized galaxies. After analyzing their properties, parts of them are classified as dwarf spheroidal galaxies of the Milky Way (or Andromeda. The mass-center of the system and the heliocentric distance are derived in this process. Careful treatments about the membership of the stars are required. Their properties are frequently updated when new data becomes available. For example, Segue1 was thought to be the best target to search for dark matter [198, 199, 264]. However, the J-factor is not so high in the latest dataset. The contamination from the foreground star caused an overestimate of the J-factor [392]. Table E.1 and E.2 list the dwarf satellite associated with Milky Way and Andromeda, respectively. The lists consist of the name, the right ascension (R.A.) and the declination (Dec) of the mass center, the heliocentric distance (d) and its error (σ_d), the half-light radius ($r_{1/2}$) and its error ($\sigma_{r_{1/2}}$), and the number of the member star if available.

Table E.1: A list of the candidates of the dwarf spheroidal galaxy associated with the Milky Way. Those above the line are so-called classical dwarfs. Note that the values in the list are frequently updated when new data appears. This list is based on the several reference papers [45, 191, 192, 240–242, 245, 246, 393–410].

Name	R.A. [hh:mm:ss]	Dec [dd:mm:ss]	d [kpc]	σ_d [kpc]	$r_{1/2}$ [pc]	$\sigma_{r_{1/2}}$ [pc]	N_{member}
Carina	06:41:36.7	- 50:57:58	105.6	5.4	203	22	758
Draco	17:20:12.4	+ 57:54:55	76	6	182	13	476
Fornax	02:39:59.3	- 34:26:57	147	9	609	38	2409
Leo I	10:08:28.1	+ 12:18:23	258.2	9.5	292	26	327
Leo II	11:13:28.8	+ 11:09:06	233	1	159	14	175
Sculptor	01:00:09.4	- 33:42:33	83.9	1.5	159	14	1349
Sextans	10:13:03.0	- 01:36:53	92.5	2.2	524	23	424
Ursa Minor	15:09:08.5	+ 67:13:21	76	4	201	23	311
Aquarius II	22:33:55.5	- 09:19:39	107.9	3.3	132	22	9
Bootes I	14:00:06.0	+ 14:30:00	66	3	187	20	37
Bootes II	13:57:12.0	+ 26:48:00	46	-	56	-	5
Carina II	07:36:24.1	- 57:59:56.76	37.4	0.4	76	8	14
Carina III	07:38:31.1	- 57:53:58.92	27.8	0.6	30	9	?
Cetus II	01:17:52.7	- 17:25:12	30	3	17	7	?
Columba I	05:31:25.67	- 28:02:33.1	183	10	117	17	?
Coma	12:26:59.0	+ 23:54:15	42	1.5	57	4	58
CVen I	13:28:03.5	+ 33:33:21	210	6	424	25	209
CVen II	12:57:10.0	+ 34:19:15	160	7	68	8	25
Draco II	02:39:51	- 34:30:39	20	3	12	-	9
Eridanus III	02:22:45.5	- 52:16:48	96	-	11	8	?
Grus I	22:56:42	- 50:09:48	120.2	11.1	52	25	5
Grus II	22:04:04.7	- 46:26:24	53	5	93	14	?
Hercules	16:31:02.0	+ 12:47:30	132	6	106	13	30
Horologium I	02:55:28.7	- 54:06:36	87	8	32	5	5
Horologium II	03:16:32.1	- 50:01:05	78	-	47	10	?
Hydra II	10:08:29.4	+ 12:18:48	151	8	71	11	13
Indus I	21:08:47.9	- 51:09:36	69	-	12	2	?
Indus II	20:38:52.8	- 46:09:36	214	16	181	67	?
Laevens I	11:36:16.2	- 10:52:38.8	145	17	19	2	10
Leo IV	11:32:57.0	- 00:32:00	154	5	111	36	17
Leo V	11:31:09.6	+ 02:13:12	173	5	30	16	8
Pegasus III	22:24:24.48	+ 05:24:18.0	215	12	37	14	7
Phoenix II	23:39:57.6	- 54:24:36	96	-	33	20	?
Pictor I	04:43:48	- 50:16:48	126	-	43	153	?
Pisces II	22:58:31.0	+ 05:57:09	183	15	48	10	7
Reticulum II	03:35:41	- 54:03:00	30	2	32	3	25
Reticulum III	03:45:26.3	- 60:27:00	92	13	64	24	?
Sagittarius	18:55:19.5	- 30:32:43	24	-	1550	50	?
Sagittarius II	19:52:40.5	- 22:04:05	67	5	38	8	?
Segue 1	10:07:04.0	+ 16:04:55	23	2	21	5	62
Segue 2	02:19:16.0	+ 20:10:31	36.6	2.45	33	3	25
Triangulum II	02:13:17.4	+ 36:10:42.4	30	2	28	8	13
Tucana	22:41:49.6	- 64:25:11	880	-	221	-	?
Tucana II	22:51:55	- 58:34:08	57.5	5.3	162	35	10
Tucana III	21:01:31.1	+ 56:11:24	25	2	43	6	26
Tucana IV	00:02:55.1	- 60:51:00	48	-	127	24	?
Tucana V	23:37:24	- 63:16:12	55	9	17	6	?
Ursa Major I	10:34:52.8	+ 51:55:12	97.3	5.85	200	21	36
Ursa Major II	08:51:30.0	+ 63:07:48	34.7	2.1	99	7	19
Willman 1	10:49:21.0	+ 51:03:00	38	7	18	4	40

Table E.2: The list of the candidates of the dwarf spheroidal galaxy associated with the Andromeda galaxy. Note that the values in the list are frequently updated when new data appears. This list is based on [192, 246, 411–418].

Name	R.A. [hh:mm:ss]	Dec [dd:mm:ss]	d [kpc]	σ_d [kpc]	$r_{1/2}$ [pc]	$\sigma_{r_{1/2}}$ [pc]	N_{member}
And I	00:45:39.8	+ 38:02:28	727	17.5	699	29	51
And II	01:16:29.8	+ 33:25:09	652	18	965	45	95
And III	00:35:30.9	+ 36:29:56	723	21	296	33	62
And V	01:10:17.1	+ 47:37:41	742	21.5	294	33	85
And VI (Pegasus)	03:01:23.6	+ 40:59:18	785	65	400	105	?
And VII	23:26:31.7	+ 50:40:33	763	35	717	39	136
And IX	00:52:53.0	+ 43:11:45	765	150	552	110	?
And X	01:06:33.7	+ 44:48:16	701	37	210	70	22
And XI	00:46:20.0	+33:48:05	763	106	120	53	?
And XII	00:47:27.0	+ 34:22:29	928	136	420	280	?
And XIII	00:51:51.0	+ 33:00:16	760	154	130	80	?
And XIV	00:51:35.0	+ 29:41:49	793	50	297	53	48
And XV	01:14:18.7	+ 38:07:03	630	60	230	35	?
And XVI	00:59:29.8	+ 32:22:36	525	50	130	30	?
And XVII	00:37:07.0	+ 44:19:28	727	39	285	55	?
And XVIII	00:02:14.5	+ 45:05:20	1214	41.5	260	38	22
And XIX	00:19:32.1	+ 35:02.37.1	821	148	1481	268	?
And XX	00:07:30.7	+ 35:07:56	741	52	90	35	?
And XXI	23:54:47.7	+ 42:28:15	827	25	842	77	?
And XXII	01:27:40.0	+ 28:05:25	920	139	225	75	?
And XXIII	01:29:21.8	+ 38:43:08	748	31	1001	53	?
And XXIV	01:18:30.0	+ 46:21:58	898	42	548	37	?
And XXV	00:30:08.9	+ 46:51:07	736	69	642	74	?
And XXVi	00:23:45.6	+ 47:54:58	754	218	219	67	?
And XXVII	00:37:27.1	+ 45:23:13	1255	474	657	271	?
And XXIX	23:58:55.6	+ 30:45:20	730	75	360	60	?
And XXX	00:36:34.6	+ 49:38:49	681	78	267	36	?
And XXXI	22:58:16.3	+ 41:17:28	756	44	912	124	?
And XXXII	00:53:59.4	+ 51:33:35	772	61	1456	267	?
Cetus	00:26:11.0	- 11:02:40	789	40	497	37	116
Eridanus II	03:44:20.1	- 43:32:01.7	366	17	176	14	28
LeoT	09:34:53.4	+ 17:03:04	407	38	142	36	19

Bibliography

[1] L. Bergström, "Nonbaryonic dark matter: Observational evidence and detection methods," *Rept. Prog. Phys.* **63** (2000) 793, arXiv:hep-ph/0002126 [hep-ph].

[2] G. Bertone, D. Hooper, and J. Silk, "Particle dark matter: Evidence, candidates and constraints," *Phys. Rept.* **405** (2005) 279–390, arXiv:hep-ph/0404175 [hep-ph].

[3] J. M. Gaskins, "A review of indirect searches for particle dark matter," *Contemp. Phys.* **57** no. 4, (2016) 496–525, arXiv:1604.00014 [astro-ph.HE].

[4] H. Hoekstra, H. Yee, and M. Gladders, "Current status of weak gravitational lensing," *New Astron. Rev.* **46** (2002) 767–781, arXiv:astro-ph/0205205 [astro-ph].

[5] T. S. van Albada, J. N. Bahcall, K. Begeman, and R. Sancisi, "The Distribution of Dark Matter in the Spiral Galaxy NGC-3198," *Astrophys. J.* **295** (1985) 305–313.

[6] P. Salucci and A. Borriello, "The intriguing distribution of dark matter in galaxies," *Lect. Notes Phys.* **616** (2003) 66–77, arXiv:astro-ph/0203457 [astro-ph].

[7] F. Zwicky, "Die Rotverschiebung von extragalaktischen Nebeln," *Helv. Phys. Acta* **6** (1933) 110–127. [Gen. Rel. Grav.41,207(2009)].

[8] F. Zwicky, "Republication of: The redshift of extragalactic nebulae," *General Relativity and Gravitation* **41** no. 1, (Jan, 2009) 207–224. https://doi.org/10.1007/s10714-008-0707-4.

[9] R. Barrena, A. Biviano, M. Ramella, E. E. Falco, and S. Seitz, "The dynamical status of the cluster of galaxies 1e0657-56," *Astron. Astrophys.* **386** (2002) 816, arXiv:astro-ph/0202323 [astro-ph].

[10] D. Clowe, A. Gonzalez, and M. Markevitch, "Weak lensing mass reconstruction of the interacting cluster 1E0657-558: Direct evidence for the existence of dark matter," *Astrophys. J.* **604** (2004) 596–603, arXiv:astro-ph/0312273 [astro-ph].

[11] G. R. Blumenthal, S. M. Faber, J. R. Primack, and M. J. Rees, "Formation of Galaxies and Large Scale Structure with Cold Dark Matter," *Nature* **311** (1984) 517–525. [,96(1984)].

[12] P. J. E. Peebles, "Large scale background temperature and mass fluctuations due to scale invariant primeval perturbations," *Astrophys. J.* **263** (1982) L1–L5.

[13] **Planck** Collaboration, P. A. R. Ade *et al.*, "Planck 2015 results. XIII. Cosmological parameters," *Astron. Astrophys.* **594** (2016) A13, arXiv:1502.01589 [astro-ph.CO].

[14] J. Silk, "Cosmic black body radiation and galaxy formation," *Astrophys. J.* **151** (1968) 459–471.

[15] **WMAP** Collaboration, E. Komatsu *et al.*, "Seven-Year Wilkinson Microwave Anisotropy Probe (WMAP) Observations: Cosmological Interpretation," *Astrophys. J. Suppl.* **192** (2011) 18, arXiv:1001.4538 [astro-ph.CO].

[16] **Planck** Collaboration, Y. Akrami *et al.*, "Planck 2018 results. I. Overview and the cosmological legacy of Planck," arXiv:1807.06205 [astro-ph.CO].

[17] **Planck** Collaboration, N. Aghanim *et al.*, "Planck 2018 results. VI. Cosmological parameters," arXiv:1807.06209 [astro-ph.CO].

[18] T. Bringmann and S. Hofmann, "Thermal decoupling of WIMPs from first principles," *JCAP* **0704** (2007) 016, arXiv:hep-ph/0612238 [hep-ph]. [Erratum: JCAP1603,no.03,E02(2016)].

[19] C. Rott, "Review of Indirect WIMP Search Experiments," arXiv:1210.4161 [astro-ph.HE]. [Nucl. Phys. Proc. Suppl.235-236,413(2013)].

[20] H. Pagels and J. R. Primack, "Supersymmetry, Cosmology and New TeV Physics," *Phys. Rev. Lett.* **48** (1982) 223.

[21] F. D. Steffen, "Gravitino dark matter and cosmological constraints," *JCAP* **0609** (2006) 001, arXiv:hep-ph/0605306 [hep-ph].

[22] R. N. Mohapatra, F. I. Olness, R. Stroynowski, and V. L. Teplitz, "Searching for strongly interacting massive particles (SIMPs)," *Phys. Rev.* **D60** (1999) 115013, arXiv:hep-ph/9906421 [hep-ph].

[23] Y. Hochberg, E. Kuflik, T. Volansky, and J. G. Wacker, "Mechanism for Thermal Relic Dark Matter of Strongly Interacting Massive Particles," *Phys. Rev. Lett.* **113** (2014) 171301, arXiv:1402.5143 [hep-ph].

[24] J. Preskill, M. B. Wise, and F. Wilczek, "Cosmology of the Invisible Axion," *Phys. Lett.* **120B** (1983) 127–132.

[25] L. J. Rosenberg and K. A. van Bibber, "Searches for invisible axions," *Phys. Rept.* **325** (2000) 1–39.

[26] L. Visinelli and P. Gondolo, "Dark Matter Axions Revisited," *Phys. Rev.* **D80** (2009) 035024, arXiv:0903.4377 [astro-ph.CO].

[27] S. Dodelson and L. M. Widrow, "Sterile-neutrinos as dark matter," *Phys. Rev. Lett.* **72** (1994) 17–20, arXiv:hep-ph/9303287 [hep-ph].

[28] X.-D. Shi and G. M. Fuller, "A New dark matter candidate: Nonthermal sterile neutrinos," *Phys. Rev. Lett.* **82** (1999) 2832–2835, arXiv:astro-ph/9810076 [astro-ph].

[29] K. Abazajian, G. M. Fuller, and M. Patel, "Sterile neutrino hot, warm, and cold dark matter," *Phys. Rev.* **D64** (2001) 023501, arXiv:astro-ph/0101524 [astro-ph].

[30] A. Boyarsky, O. Ruchayskiy, and M. Shaposhnikov, "The Role of sterile neutrinos in cosmology and astrophysics," *Ann. Rev. Nucl. Part. Sci.* **59** (2009) 191–214, arXiv:0901.0011 [hep-ph].

[31] N. Afshordi, P. McDonald, and D. N. Spergel, "Primordial black holes as dark matter: The Power spectrum and evaporation of early structures," *Astrophys. J.* **594** (2003) L71–L74, arXiv:astro-ph/0302035 [astro-ph].

[32] B. Carr, F. Kuhnel, and M. Sandstad, "Primordial Black Holes as Dark Matter," *Phys. Rev.* **D94** no. 8, (2016) 083504, arXiv:1607.06077 [astro-ph.CO].

[33] B. J. Carr, K. Kohri, Y. Sendouda, and J. Yokoyama, "Constraints on primordial black holes from the Galactic gamma-ray background," *Phys. Rev.* **D94** no. 4, (2016) 044029, arXiv:1604.05349 [astro-ph.CO].

[34] B. Carr and J. Silk, "Primordial Black Holes as Seeds for Cosmic Structures," arXiv:1801.00672 [astro-ph.CO].

[35] K. Kohri and T. Terada, "Primordial Black Hole Dark Matter and LIGO/Virgo Merger Rate from Inflation with Running Spectral Indices," arXiv:1802.06785 [astro-ph.CO].

[36] G. Jungman, M. Kamionkowski, and K. Griest, "Supersymmetric dark matter," *Phys. Rept.* **267** (1996) 195–373, arXiv:hep-ph/9506380 [hep-ph].

[37] J. L. Feng, K. T. Matchev, and F. Wilczek, "Neutralino dark matter in focus point supersymmetry," *Phys. Lett.* **B482** (2000) 388–399, arXiv:hep-ph/0004043 [hep-ph].

[38] G. Steigman, B. Dasgupta, and J. F. Beacom, "Precise Relic WIMP Abundance and its Impact on Searches for Dark Matter Annihilation," *Phys. Rev.* **D86** (2012) 023506, arXiv:1204.3622 [hep-ph].

[39] H. Goldberg, "Constraint on the Photino Mass from Cosmology," *Phys. Rev. Lett.* **50** (1983) 1419. [,219(1983)].

[40] **ATLAS** Collaboration, M. Aaboud *et al.*, "Search for top-squark pair production in final states with one lepton, jets, and missing transverse momentum using 36 fb^{-1} of $\sqrt{s}$ = 13 TeV pp collision data with the ATLAS detector," arXiv:1711.11520 [hep-ex].

[41] **CMS** Collaboration, A. M. Sirunyan *et al.*, "Search for dark matter produced in association with heavy-flavor quark pairs in proton-proton collisions at $\sqrt{s}$ = 13 TeV," *Eur. Phys. J.* **C77** no. 12, (2017) 845, arXiv:1706.02581 [hep-ex].

[42] **LUX** Collaboration, D. S. Akerib *et al.*, "Results from a search for dark matter in the complete LUX exposure," *Phys. Rev. Lett.* **118** no. 2, (2017) 021303, arXiv:1608.07648 [astro-ph.CO].

[43] **PICO** Collaboration, C. Amole *et al.*, "Dark Matter Search Results from the PICO-60 C_3F_8 Bubble Chamber," *Phys. Rev. Lett.* **118** no. 25, (2017) 251301, arXiv:1702.07666 [astro-ph.CO].

[44] **XENON** Collaboration, E. Aprile *et al.*, "Dark Matter Search Results from a One Tonne×Year Exposure of XENON1T," arXiv:1805.12562 [astro-ph.CO].

[45] **DES, Fermi-LAT** Collaboration, A. Albert *et al.*, "Searching for Dark Matter Annihilation in Recently Discovered Milky Way Satellites with Fermi-LAT," *Astrophys. J.* **834** no. 2, (2017) 110, arXiv:1611.03184 [astro-ph.HE].

[46] S. Tremaine and J. E. Gunn, "Dynamical Role of Light Neutral Leptons in Cosmology," *Phys. Rev. Lett.* **42** (1979) 407–410. [,66(1979)].

[47] K. Abazajian, "Linear cosmological structure limits on warm dark matter," *Phys. Rev.* **D73** (2006) 063513, arXiv:astro-ph/0512631 [astro-ph].

[48] S. Horiuchi, P. J. Humphrey, J. Onorbe, K. N. Abazajian, M. Kaplinghat, and S. Garrison-Kimmel, "Sterile neutrino dark matter bounds from galaxies of the Local Group," *Phys. Rev.* **D89** no. 2, (2014) 025017, arXiv:1311.0282 [astro-ph.CO].

[49] A. Boyarsky, J. Lesgourgues, O. Ruchayskiy, and M. Viel, "Lyman-alpha constraints on warm and on warm-plus-cold dark matter models," *JCAP* **0905** (2009) 012, arXiv:0812.0010 [astro-ph].

[50] **AMS** Collaboration, M. Aguilar *et al.*, "Precision Measurement of the Proton Flux in Primary Cosmic Rays from Rigidity 1 GV to 1.8 TV with the Alpha Magnetic Spectrometer on the International Space Station," *Phys. Rev. Lett.* **114** (2015) 171103.

[51] **AMS** Collaboration, M. Aguilar *et al.*, "Precision Measurement of the Boron to Carbon Flux Ratio in Cosmic Rays from 1.9 GV to 2.6 TV with the Alpha Magnetic Spectrometer on the International Space Station," *Phys. Rev. Lett.* **117** no. 23, (2016) 231102.

[52] **DAMPE** Collaboration, J. Chang *et al.*, "The DArk Matter Particle Explorer mission," *Astropart. Phys.* **95** (2017) 6–24, arXiv:1706.08453 [astro-ph.IM].

[53] H. Motz, Y. Asaoka, S. Torii, and S. Bhattacharyya, "CALET's Sensitivity to Dark Matter Annihilation in the Galactic Halo," *JCAP* **1512** no. 12, (2015) 047, arXiv:1510.03168 [astro-ph.HE].

[54] **IceCube** Collaboration, M. G. Aartsen *et al.*, "Search for Neutrinos from Dark Matter Self-Annihilations in the center of the Milky Way with 3 years of IceCube/DeepCore," *Eur. Phys. J.* **C77** no. 9, (2017) 627, arXiv:1705.08103 [hep-ex].

[55] **ANTARES** Collaboration, A. Albert *et al.*, "Search for Dark Matter Annihilation in the Earth using the ANTARES Neutrino Telescope," *Phys. Dark Univ.* **16** (2017) 41–48, arXiv:1612.06792 [hep-ex].

[56] S. Hofmann, D. J. Schwarz, and H. Stoecker, "Damping scales of neutralino cold dark matter," *Phys. Rev.* **D64** (2001) 083507, arXiv:astro-ph/0104173 [astro-ph].

[57] A. M. Green, S. Hofmann, and D. J. Schwarz, "The power spectrum of SUSY - CDM on sub-galactic scales," *Mon. Not. Roy. Astron. Soc.* **353** (2004) L23, arXiv:astro-ph/0309621 [astro-ph].

[58] S. Profumo, K. Sigurdson, and M. Kamionkowski, "What mass are the smallest protohalos?," *Phys. Rev. Lett.* **97** (2006) 031301, arXiv:astro-ph/0603373 [astro-ph].

[59] R. Diamanti, M. E. C. Catalan, and S. Ando, "Dark matter protohalos in a nine parameter MSSM and implications for direct and indirect detection," *Phys. Rev.* **D92** no. 6, (2015) 065029, arXiv:1506.01529 [hep-ph].

[60] X.-l. Chen, M. Kamionkowski, and X.-m. Zhang, "Kinetic decoupling of neutralino dark matter," *Phys. Rev.* **D64** (2001) 021302, arXiv:astro-ph/0103452 [astro-ph].

[61] A. Pinzke, C. Pfrommer, and L. Bergstrom, "Prospects of detecting gamma-ray emission from galaxy clusters: cosmic rays and dark matter annihilations," *Phys. Rev.* **D84** (2011) 123509, arXiv:1105.3240 [astro-ph.HE].

[62] M. A. Sanchez-Conde, M. Cannoni, F. Zandanel, M. E. Gomez, and F. Prada, "Dark matter searches with Cherenkov telescopes: nearby dwarf galaxies or local galaxy clusters?," *JCAP* **1112** (2011) 011, arXiv:1104.3530 [astro-ph.HE].

[63] W. Hu and J. Silk, "Thermalization constraints and spectral distortions for massive unstable relic particles," *Phys. Rev. Lett.* **70** (1993) 2661–2664.

[64] P. Blasi, A. V. Olinto, and C. Tyler, "Detecting WIMPs in the microwave sky," *Astropart. Phys.* **18** (2003) 649–662, arXiv:astro-ph/0202049 [astro-ph].

[65] **WMAP** Collaboration, C. L. Bennett *et al.*, "First year Wilkinson Microwave Anisotropy Probe (WMAP) observations: Preliminary maps and basic results," *Astrophys. J. Suppl.* **148** (2003) 1–27, arXiv:astro-ph/0302207 [astro-ph].

[66] **SDSS** Collaboration, D. J. Eisenstein *et al.*, "Detection of the Baryon Acoustic Peak in the Large-Scale Correlation Function of SDSS Luminous Red Galaxies," *Astrophys. J.* **633** (2005) 560–574, arXiv:astro-ph/0501171 [astro-ph].

[67] A. G. Sanchez, M. Crocce, A. Cabre, C. M. Baugh, and E. Gaztanaga, "Cosmological parameter constraints from SDSS luminous red galaxies: a new treatment of large-scale clustering," *Mon. Not. Roy. Astron. Soc.* **400** (2009) 1643, arXiv:0901.2570 [astro-ph.CO].

[68] **DES** Collaboration, T. M. C. Abbott *et al.*, "Dark Energy Survey Year 1 Results: A Precise H_0 Measurement from DES Y1, BAO, and D/H Data," *Mon. Not. Roy. Astron. Soc.* **480** (2018) 3879, arXiv:1711.00403 [astro-ph.CO].

[69] J. Hisano, M. Kawasaki, K. Kohri, T. Moroi, and K. Nakayama, "Cosmic Rays from Dark Matter Annihilation and Big-Bang Nucleosynthesis," *Phys. Rev.* **D79** (2009) 083522, arXiv:0901.3582 [hep-ph].

[70] B. Henning and H. Murayama, "Constraints on Light Dark Matter from Big Bang Nucleosynthesis," arXiv:1205.6479 [hep-ph].

[71] **Telescope Array** Collaboration, R. U. Abbasi *et al.*, "Mass composition of ultra-high-energy cosmic rays with the Telescope Array Surface Detector Data," arXiv:1808.03680 [astro-ph.HE].

[72] **Pierre Auger** Collaboration, A. Aab *et al.*, "Large-scale cosmic-ray anisotropies above 4 EeV measured by the Pierre Auger Observatory," *Astrophys. J.* **868** no. 1, (2018) 4, arXiv:1808.03579 [astro-ph.HE].

[73] J. R. Ellis, J. S. Hagelin, D. V. Nanopoulos, K. A. Olive, and M. Srednicki, "Supersymmetric Relics from the Big Bang," *Nucl. Phys.* **B238** (1984) 453–476. [,223(1983)].

[74] M. Ibe, H. Murayama, and T. T. Yanagida, "Breit-Wigner Enhancement of Dark Matter Annihilation," *Phys. Rev.* **D79** (2009) 095009, arXiv:0812.0072 [hep-ph].

[75] J. Hisano, S. Matsumoto, and M. M. Nojiri, "Explosive dark matter annihilation," *Phys. Rev. Lett.* **92** (2004) 031303, arXiv:hep-ph/0307216 [hep-ph].

[76] **Fermi-LAT** Collaboration, E. Charles *et al.*, "Sensitivity Projections for Dark Matter Searches with the Fermi Large Area Telescope," *Phys. Rept.* **636** (2016) 1–46, arXiv:1605.02016 [astro-ph.HE].

[77] J. Hisano, M. Kawasaki, K. Kohri, T. Moroi, K. Nakayama, and T. Sekiguchi, "Cosmological constraints on dark matter models with velocity-dependent annihilation cross section," *Phys. Rev.* **D83** (2011) 123511, arXiv:1102.4658 [hep-ph].

[78] S. Tulin and H.-B. Yu, "Dark Matter Self-interactions and Small Scale Structure," *Phys. Rept.* **730** (2018) 1–57, arXiv:1705.02358 [hep-ph].

[79] D. N. Spergel and P. J. Steinhardt, "Observational evidence for selfinteracting cold dark matter," *Phys. Rev. Lett.* **84** (2000) 3760–3763, arXiv:astro-ph/9909386 [astro-ph].

[80] W. J. G. de Blok, "The Core-Cusp Problem," *Adv. Astron.* **2010** (2010) 789293, arXiv:0910.3538 [astro-ph.CO].

[81] M. Boylan-Kolchin, J. S. Bullock, and M. Kaplinghat, "Too big to fail? The puzzling darkness of massive Milky Way subhaloes," *Mon. Not. Roy. Astron. Soc.* **415** (2011) L40, arXiv:1103.0007 [astro-ph.CO].

[82] J. Zavala, M. Vogelsberger, and M. G. Walker, "Constraining Self-Interacting Dark Matter with the Milky Way's dwarf spheroidals," *Mon. Not. Roy. Astron. Soc.* **431** (2013) L20–L24, arXiv:1211.6426 [astro-ph.CO].

[83] M. Vogelsberger, J. Zavala, and A. Loeb, "Subhaloes in Self-Interacting Galactic Dark Matter Haloes," *Mon. Not. Roy. Astron. Soc.* **423** (2012) 3740, arXiv:1201.5892 [astro-ph.CO].

[84] M. Bradac, S. W. Allen, T. Treu, H. Ebeling, R. Massey, R. G. Morris, A. von der Linden, and D. Applegate, "Revealing the properties of dark matter in the merging cluster MACSJ0025.4-1222," *Astrophys. J.* **687** (2008) 959, arXiv:0806.2320 [astro-ph].

[85] J. Merten *et al.*, "Creation of cosmic structure in the complex galaxy cluster merger Abell 2744," *Mon. Not. Roy. Astron. Soc.* **417** (2011) 333–347, arXiv:1103.2772 [astro-ph.CO].

[86] W. A. Dawson *et al.*, "Discovery of a Dissociative Galaxy Cluster Merger with Large Physical Separation," *Astrophys. J.* **747** (2012) L42, arXiv:1110.4391 [astro-ph.CO].

[87] F. Kahlhoefer, K. Schmidt-Hoberg, J. Kummer, and S. Sarkar, "On the interpretation of dark matter self-interactions in Abell 3827," *Mon. Not. Roy. Astron. Soc.* **452** no. 1, (2015) L54–L58, arXiv:1504.06576 [astro-ph.CO].

[88] E. K. Akhmedov, V. A. Rubakov, and A. Yu. Smirnov, "Baryogenesis via neutrino oscillations," *Phys. Rev. Lett.* **81** (1998) 1359–1362, arXiv:hep-ph/9803255 [hep-ph].

[89] L. Canetti, M. Drewes, and M. Shaposhnikov, "Sterile Neutrinos as the Origin of Dark and Baryonic Matter," *Phys. Rev. Lett.* **110** no. 6, (2013) 061801, arXiv:1204.3902 [hep-ph].

[90] A. D. Dolgov and S. H. Hansen, "Massive sterile neutrinos as warm dark matter," *Astropart. Phys.* **16** (2002) 339–344, arXiv:hep-ph/0009083 [hep-ph].

[91] M. Laine and M. Shaposhnikov, "Sterile neutrino dark matter as a consequence of nuMSM-induced lepton asymmetry," *JCAP* **0806** (2008) 031, arXiv:0804.4543 [hep-ph].

[92] R. Shrock, "Decay l0 —¿ nu(lepton) gamma in gauge theories of weak and electromagnetic interactions," *Phys. Rev.* **D9** (1974) 743–748.

[93] P. B. Pal and L. Wolfenstein, "Radiative Decays of Massive Neutrinos," *Phys. Rev.* **D25** (1982) 766.

[94] V. D. Barger, R. J. N. Phillips, and S. Sarkar, "Remarks on the KARMEN anomaly," *Phys. Lett.* **B352** (1995) 365–371, arXiv:hep-ph/9503295 [hep-ph]. [Erratum: Phys. Lett.B356,617(1995)].

[95] A. Boyarsky, M. Drewes, T. Lasserre, S. Mertens, and O. Ruchayskiy, "Sterile Neutrino Dark Matter," *Prog. Part. Nucl. Phys.* **104** (2019) 1–45, arXiv:1807.07938 [hep-ph].

[96] E. Bulbul, M. Markevitch, A. Foster, R. K. Smith, M. Loewenstein, and S. W. Randall, "Detection of An Unidentified Emission Line in the Stacked X-ray spectrum of Galaxy Clusters," *Astrophys. J.* **789** (2014) 13, arXiv:1402.2301 [astro-ph.CO].

[97] A. Boyarsky, O. Ruchayskiy, D. Iakubovskyi, and J. Franse, "Unidentified Line in X-Ray Spectra of the Andromeda Galaxy and Perseus Galaxy Cluster," *Phys. Rev. Lett.* **113** (2014) 251301, arXiv:1402.4119 [astro-ph.CO].

[98] C. R. Watson, Z.-Y. Li, and N. K. Polley, "Constraining Sterile Neutrino Warm Dark Matter with Chandra Observations of the Andromeda Galaxy," *JCAP* **1203** (2012) 018, arXiv:1111.4217 [astro-ph.CO].

[99] S. Riemer-S ø rensen, "Constraints on the presence of a 3.5 keV dark matter emission line from Chandra observations of the Galactic centre," *Astron. Astrophys.* **590** (2016) A71, arXiv:1405.7943 [astro-ph.CO].

[100] L. Gu, J. Kaastra, A. J. J. Raassen, P. D. Mullen, R. S. Cumbee, D. Lyons, and P. C. Stancil, "A novel scenario for the possible X-ray line feature at 3.5 keV: Charge exchange with bare sulfur ions," *Astron. Astrophys.* **584** (2015) L11, arXiv:1511.06557 [astro-ph.HE].

[101] C. Shah, S. Dobrodey, S. Bernitt, R. Steinbr ü gge, J. R. C. L ó pez-Urrutia, L. Gu, and J. Kaastra, "Laboratory measurements compellingly support charge-exchange mechanism for the 'dark matter' ~3.5 keV X-ray line," *Astrophys. J.* **833** no. 1, (2016) 52, arXiv:1608.04751 [astro-ph.HE].

[102] J. Baur, N. Palanque-Delabrouille, C. Yeche, A. Boyarsky, O. Ruchayskiy, U. Armengaud, and J. Lesgourgues, "Constraints from Ly-α forests on non-thermal dark matter including resonantly-produced sterile neutrinos," *JCAP* **1712** no. 12, (2017) 013, arXiv:1706.03118 [astro-ph.CO].

[103] M.-Y. Wang, J. F. Cherry, S. Horiuchi, and L. E. Strigari, "Bounds on Resonantly-Produced Sterile Neutrinos from Phase Space Densities of Milky Way Dwarf Galaxies," arXiv:1712.04597 [astro-ph.CO].

[104] R. D. Peccei and H. R. Quinn, "CP Conservation in the Presence of Instantons," *Phys. Rev. Lett.* **38** (1977) 1440–1443. [,328(1977)].

[105] M. Dine, W. Fischler, and M. Srednicki, "A Simple Solution to the Strong CP Problem with a Harmless Axion," *Phys. Lett.* **104B** (1981) 199–202.

[106] R. D. Peccei, "The Strong CP problem and axions," *Lect. Notes Phys.* **741** (2008) 3–17, arXiv:hep-ph/0607268 [hep-ph]. [,3(2006)].

[107] J. E. Kim and G. Carosi, "Axions and the Strong CP Problem," *Rev. Mod. Phys.* **82** (2010) 557–602, arXiv:0807.3125 [hep-ph].

[108] L. Hui, J. P. Ostriker, S. Tremaine, and E. Witten, "Ultralight scalars as cosmological dark matter," *Phys. Rev.* **D95** no. 4, (2017) 043541, arXiv:1610.08297 [astro-ph.CO].

[109] G. G. Raffelt, "Astrophysical axion bounds," *Lect. Notes Phys.* **741** (2008) 51–71, arXiv:hep-ph/0611350 [hep-ph]. [,51(2006)].

[110] D. J. E. Marsh and J. C. Niemeyer, "Strong Constraints on Fuzzy Dark Matter from Ultrafaint Dwarf Galaxy Eridanus II," arXiv:1810.08543 [astro-ph.CO].

[111] S. Hoof, F. Kahlhoefer, P. Scott, C. Weniger, and M. White, "Axion global fits with Peccei-Quinn symmetry breaking before inflation using GAMBIT," arXiv:1810.07192 [hep-ph].

[112] C. Abel *et al.*, "Search for Axionlike Dark Matter through Nuclear Spin Precession in Electric and Magnetic Fields," *Phys. Rev.* **X7** no. 4, (2017) 041034, arXiv:1708.06367 [hep-ph].

[113] T. Dafni, C. A. J. O'Hare, B. Laki ć , J. Gal á n, F. J. Iguaz, I. G. Irastorza, K. Jakov č i ć , G. Luz ó n, J. Redondo, and E. R. Ch ó liz, "Weighing the Solar Axion," arXiv:1811.09290 [hep-ph].

[114] B. J. Carr and S. W. Hawking, "Black holes in the early Universe," *Mon. Not. Roy. Astron. Soc.* **168** (1974) 399–415.

[115] B. J. Carr, K. Kohri, Y. Sendouda, and J. Yokoyama, "New cosmological constraints on primordial black holes," *Phys. Rev.* **D81** (2010) 104019, arXiv:0912.5297 [astro-ph.CO].

[116] S. W. Hawking, "Black hole explosions," *Nature* **248** (1974) 30–31.

[117] S. W. Hawking, "Particle Creation by Black Holes," *Commun. Math. Phys.* **43** (1975) 199–220. [,167(1975)].

[118] A. Barnacka, J. F. Glicenstein, and R. Moderski, "New constraints on primordial black holes abundance from femtolensing of gamma-ray bursts," *Phys. Rev.* **D86** (2012) 043001, arXiv:1204.2056 [astro-ph.CO].

[119] K. Griest, A. M. Cieplak, and M. J. Lehner, "Experimental Limits on Primordial Black Hole Dark Matter from the First 2 yr of Kepler Data," *Astrophys. J.* **786** no. 2, (2014) 158, arXiv:1307.5798 [astro-ph.CO].

[120] K. Griest, A. M. Cieplak, and M. J. Lehner, "New Limits on Primordial Black Hole Dark Matter from an Analysis of Kepler Source Microlensing Data," *Phys. Rev. Lett.* **111** no. 18, (2013) 181302.

[121] **EROS-2** Collaboration, P. Tisserand *et al.*, "Limits on the Macho Content of the Galactic Halo from the EROS-2 Survey of the Magellanic Clouds," *Astron. Astrophys.* **469** (2007) 387–404, arXiv:astro-ph/0607207 [astro-ph].

[122] S. Calchi Novati, S. Mirzoyan, P. Jetzer, and G. Scarpetta, "Microlensing towards the SMC: a new analysis of OGLE and EROS results," *Mon. Not. Roy. Astron. Soc.* **435** (2013) 1582, arXiv:1308.4281 [astro-ph.GA].

[123] E. Mediavilla, J. A. Munoz, E. Falco, V. Motta, E. Guerras, H. Canovas, C. Jean, A. Oscoz, and A. M. Mosquera, "Microlensing-Based Estimate of the Mass Fraction in Compact Objects in Lens," *Astrophys. J.* **706** (2009) 1451–1462, arXiv:0910.3645 [astro-ph.CO].

[124] P. N. Wilkinson, D. R. Henstock, I. W. A. Browne, A. G. Polatidis, P. Augusto, A. C. S. Readhead, T. J. Pearson, W. Xu, G. B. Taylor, and R. C. Vermeulen, "Limits on the cosmological abundance of supermassive compact objects from a search for multiple imaging in compact radio sources," *Phys. Rev. Lett.* **86** (2001) 584–587, arXiv:astro-ph/0101328 [astro-ph].

[125] F. Capela, M. Pshirkov, and P. Tinyakov, "Constraints on primordial black holes as dark matter candidates from capture by neutron stars," *Phys. Rev.* **D87** no. 12, (2013) 123524, arXiv:1301.4984 [astro-ph.CO].

[126] P. W. Graham, S. Rajendran, and J. Varela, "Dark Matter Triggers of Supernovae," *Phys. Rev.* **D92** no. 6, (2015) 063007, arXiv:1505.04444 [hep-ph].

[127] T. D. Brandt, "Constraints on MACHO Dark Matter from Compact Stellar Systems in Ultra-Faint Dwarf Galaxies," *Astrophys. J.* **824** no. 2, (2016) L31, arXiv:1605.03665 [astro-ph.GA].

[128] D. P. Quinn, M. I. Wilkinson, M. J. Irwin, J. Marshall, A. Koch, and V. Belokurov, "On the Reported Death of the MACHO Era," *Mon. Not. Roy. Astron. Soc.* **396** (2009) 11, arXiv:0903.1644 [astro-ph.GA].

[129] B. J. Carr and M. Sakellariadou, "Dynamical constraints on dark compact objects," *Astrophys. J.* **516** (1999) 195–220.

[130] K. Kohri and J. Yokoyama, "Primordial black holes and primordial nucleosynthesis. 1. Effects of hadron injection from low mass holes," *Phys. Rev.* **D61** (2000) 023501, arXiv:astro-ph/9908160 [astro-ph].

[131] H. Tashiro and N. Sugiyama, "Constraints on Primordial Black Holes by Distortions of Cosmic Microwave Background," *Phys. Rev.* **D78** (2008) 023004, arXiv:0801.3172 [astro-ph].

[132] Y. Inoue and A. Kusenko, "New X-ray bound on density of primordial black holes," *JCAP* **1710** no. 10, (2017) 034, arXiv:1705.00791 [astro-ph.CO].

[133] M. Ricotti, J. P. Ostriker, and K. J. Mack, "Effect of Primordial Black Holes on the Cosmic Microwave Background and Cosmological Parameter Estimates," *Astrophys. J.* **680** (2008) 829, arXiv:0709.0524 [astro-ph].

[134] Y. Ali-Haï moud and M. Kamionkowski, "Cosmic microwave background limits on accreting primordial black holes," *Phys. Rev.* **D95** no. 4, (2017) 043534, arXiv:1612.05644 [astro-ph.CO].

[135] D. Aloni, K. Blum, and R. Flauger, "Cosmic microwave background constraints on primordial black hole dark matter," *JCAP* **1705** no. 05, (2017) 017, arXiv:1612.06811 [astro-ph.CO].

[136] V. Poulin, J. Lesgourgues, and P. D. Serpico, "Cosmological constraints on exotic injection of electromagnetic energy," *JCAP* **1703** no. 03, (2017) 043, arXiv:1610.10051 [astro-ph.CO].

[137] R. R. Lane, L. L. Kiss, G. F. Lewis, R. A. Ibata, A. Siebert, T. R. Bedding, and P. Szekely, "Testing Newtonian Gravity with AAOmega: Mass-to-Light Profiles of Four Globular Clusters," *Mon. Not. Roy. Astron. Soc.* **400** (2009) 917–923, arXiv:0908.0770 [astro-ph.GA].

[138] H. Niikura *et al.*, "Microlensing constraints on primordial black holes with the Subaru/HSC Andromeda observation," arXiv:1701.02151 [astro-ph.CO].

[139] A. Franceschini, G. Rodighiero, and M. Vaccari, "The extragalactic optical-infrared background radiations, their time evolution and the cosmic photon-photon opacity," *Astron. Astrophys.* **487** (2008) 837, arXiv:0805.1841 [astro-ph].

[140] A. De Angelis and M. Mallamaci, "Gamma-Ray Astrophysics," *Eur. Phys. J. Plus* **133** (2018) 324, arXiv:1805.05642 [astro-ph.HE].

[141] **Fermi-LAT** Collaboration, M. Ackermann *et al.*, "The spectrum of isotropic diffuse gamma-ray emission between 100 MeV and 820 GeV," *Astrophys. J.* **799** (2015) 86, arXiv:1410.3696 [astro-ph.HE].

[142] C. Blanco and D. Hooper, "Constraints on Decaying Dark Matter from the Isotropic Gamma-Ray Background," arXiv:1811.05988 [astro-ph.HE].

[143] Y. Inoue and Y. T. Tanaka, "Lower Bound on the Cosmic TeV Gamma-ray Background Radiation," *Astrophys. J.* **818** (2016) 187, arXiv:1512.00855 [astro-ph.HE].

[144] M. Di Mauro, F. Calore, F. Donato, M. Ajello, and L. Latronico, "Diffuse γ-ray emission from misaligned active galactic nuclei," *Astrophys. J.* **780** (2014) 161, arXiv:1304.0908 [astro-ph.HE].

[145] S. Ando and E. Komatsu, "Constraints on the annihilation cross section of dark matter particles from anisotropies in the diffuse gamma-ray background measured with Fermi-LAT," *Phys. Rev.* **D87** no. 12, (2013) 123539, arXiv:1301.5901 [astro-ph.CO].

[146] M. Fornasa *et al.*, "Angular power spectrum of the diffuse gamma-ray emission as measured by the Fermi Large Area Telescope and constraints on its dark matter interpretation," *Phys. Rev.* **D94** no. 12, (2016) 123005, arXiv:1608.07289 [astro-ph.HE].

[147] **Fermi-LAT** Collaboration, M. Ackermann *et al.*, "Limits on Dark Matter Annihilation Signals from the Fermi LAT 4-year Measurement of the Isotropic Gamma-Ray Background," *JCAP* **1509** (2015) 008, arXiv:1501.05464 [astro-ph.CO].

[148] M. H ü tten, C. Combet, and D. Maurin, "Extragalactic diffuse γ-rays from dark matter annihilation: revised prediction and full modelling uncertainties," *JCAP* **1802** no. 02, (2018) 005, arXiv:1711.08323 [astro-ph.CO].

[149] H.-S. Zechlin, S. Manconi, and F. Donato, "Constraining Galactic dark matter with gamma-ray pixel counts statistics," *Phys. Rev.* **D98** no. 8, (2018) 083022, arXiv:1710.01506 [astro-ph.HE].

[150] S. Ando, A. Benoit-L é vy, and E. Komatsu, "Mapping dark matter in the gamma-ray sky with galaxy catalogs," *Phys. Rev.* **D90** no. 2, (2014) 023514, arXiv:1312.4403 [astro-ph.CO].

[151] A. Cuoco, J.-Q. Xia, M. Regis, E. Branchini, N. Fornengo, and M. Viel, "Dark Matter Searches in the Gamma-ray Extragalactic Background via Cross-correlations With Galaxy Catalogs," *Astrophys. J. Suppl.* **221** no. 2, (2015) 29, arXiv:1506.01030 [astro-ph.HE].

[152] T. Tr ö ster *et al.*, "Cross-correlation of weak lensing and gamma rays: implications for the nature of dark matter," arXiv:1611.03554 [astro-ph.CO]. [Mon. Not. Roy. Astron. Soc.467,no.3,2706(2017)].

[153] M. Shirasaki, S. Horiuchi, and N. Yoshida, "Cross-Correlation of Cosmic Shear and Extragalactic Gamma-ray Background: Constraints on the Dark Matter Annihilation Cross-Section," *Phys. Rev.* **D90** no. 6, (2014) 063502, arXiv:1404.5503 [astro-ph.CO].

[154] S. Ammazzalorso, N. Fornengo, S. Horiuchi, and M. Regis, "Characterizing the local gamma-ray Universe via angular cross-correlations," *Phys. Rev.* **D98** no. 10, (2018) 103007, arXiv:1808.09225 [astro-ph.CO].

[155] S. S. Campbell, A. Kwa, and M. Kaplinghat, "The galactic isotropic γ-ray background and implications for dark matter," *Mon. Not. Roy. Astron. Soc.* **479** no. 3, (2018) 3616–3633, arXiv:1709.04014 [astro-ph.HE].

[156] T. Cohen, K. Murase, N. L. Rodd, B. R. Safdi, and Y. Soreq, "γ -ray Constraints on Decaying Dark Matter and Implications for IceCube," *Phys. Rev. Lett.* **119** no. 2, (2017) 021102, arXiv:1612.05638 [hep-ph].

[157] M. Ackermann *et al.*, "Constraints on Dark Matter Annihilation in Clusters of Galaxies with the Fermi Large Area Telescope," *JCAP* **1005** (2010) 025, arXiv:1002.2239 [astro-ph.CO].

[158] X. Huang, G. Vertongen, and C. Weniger, "Probing Dark Matter Decay and Annihilation with Fermi LAT Observations of Nearby Galaxy Clusters," *JCAP* **1201** (2012) 042, arXiv:1110.1529 [hep-ph].

[159] **MAGIC** Collaboration, V. A. Acciari *et al.*, "Constraining Dark Matter lifetime with a deep gamma-ray survey of the Perseus Galaxy Cluster with MAGIC," *Phys. Dark Univ.* **22** (2018) 38–47, arXiv:1806.11063 [astro-ph.HE].

[160] **Fermi-LAT** Collaboration, M. Ackermann *et al.*, "Fermi LAT Search for Dark Matter in Gamma-ray Lines and the Inclusive Photon Spectrum," *Phys. Rev.* **D86** (2012) 022002, arXiv:1205.2739 [astro-ph.HE].

[161] M. Benito, N. Bernal, N. Bozorgnia, F. Calore, and F. Iocco, "Particle Dark Matter Constraints: the Effect of Galactic Uncertainties," *JCAP* **1702** no. 02, (2017) 007, arXiv:1612.02010 [hep-ph]. [Erratum: JCAP1806,no.06,E01(2018)].

[162] V. Lefranc, E. Moulin, P. Panci, F. Sala, and J. Silk, "Dark Matter in γ lines: Galactic Center vs dwarf galaxies," *JCAP* **1609** no. 09, (2016) 043, arXiv:1608.00786 [astro-ph.HE].

[163] O. Y. Gnedin and J. R. Primack, "Dark Matter Profile in the Galactic Center," *Phys. Rev. Lett.* **93** (2004) 061302, arXiv:astro-ph/0308385 [astro-ph].

[164] C. Taylor, M. Boylan-Kolchin, P. Torrey, M. Vogelsberger, and L. Hernquist, "The Mass Profile of the Milky Way to the Virial Radius from the Illustris Simulation," *Mon. Not. Roy. Astron. Soc.* **461** no. 4, (2016) 3483–3493, arXiv:1510.06409 [astro-ph.CO].

[165] V. Gammaldi, V. Avila-Reese, O. Valenzuela, and A. X. Gonzales-Morales, "Analysis of the very inner Milky Way dark matter distribution and gamma-ray signals," *Phys. Rev.* **D94** no. 12, (2016) 121301, arXiv:1607.02012 [astro-ph.HE].

[166] D. Hooper, "The Density of Dark Matter in the Galactic Bulge and Implications for Indirect Detection," *Phys. Dark Univ.* **15** (2017) 53–56, arXiv:1608.00003 [astro-ph.HE].

[167] **Fermi-LAT** Collaboration, M. Ackermann *et al.*, "The Fermi Galactic Center GeV Excess and Implications for Dark Matter," *Astrophys. J.* **840** no. 1, (2017) 43, arXiv:1704.03910 [astro-ph.HE].

[168] **H.E.S.S.** Collaboration, H. Abdalla *et al.*, "H.E.S.S. Limits on Linelike Dark Matter Signatures in the 100 GeV to 2 TeV Energy Range Close to the Galactic Center," *Phys. Rev. Lett.* **117** no. 15, (2016) 151302, arXiv:1609.08091 [astro-ph.HE].

[169] D. Hooper and L. Goodenough, "Dark Matter Annihilation in The Galactic Center As Seen by the Fermi Gamma Ray Space Telescope," *Phys. Lett.* **B697** (2011) 412–428, arXiv:1010.2752 [hep-ph].

[170] D. Hooper and T. Linden, "On The Origin Of The Gamma Rays From The Galactic Center," *Phys. Rev.* **D84** (2011) 123005, arXiv:1110.0006 [astro-ph.HE].

[171] T. Daylan, D. P. Finkbeiner, D. Hooper, T. Linden, S. K. N. Portillo, N. L. Rodd, and T. R. Slatyer, "The characterization of the gamma-ray signal from the central Milky Way: A case for annihilating dark matter," *Phys. Dark Univ.* **12** (2016) 1–23, arXiv:1402.6703 [astro-ph.HE].

[172] A. Boyarsky, D. Malyshev, and O. Ruchayskiy, "A comment on the emission from the Galactic Center as seen by the Fermi telescope," *Phys. Lett.* **B705** (2011) 165–169, arXiv:1012.5839 [hep-ph].

[173] C. Gordon and O. Macias, "Dark Matter and Pulsar Model Constraints from Galactic Center Fermi-LAT Gamma Ray Observations," *Phys. Rev.* **D88** no. 8, (2013) 083521, arXiv:1306.5725 [astro-ph.HE]. [Erratum: Phys. Rev.D89,no.4,049901(2014)].

[174] F. Calore, I. Cholis, and C. Weniger, "Background Model Systematics for the Fermi GeV Excess," *JCAP* **1503** (2015) 038, arXiv:1409.0042 [astro-ph.CO].

[175] K. N. Abazajian and M. Kaplinghat, "Detection of a Gamma-Ray Source in the Galactic Center Consistent with Extended Emission from Dark Matter Annihilation and Concentrated Astrophysical Emission," *Phys. Rev.* **D86** (2012) 083511, arXiv:1207.6047 [astro-ph.HE]. [Erratum: Phys. Rev.D87,129902(2013)].

[176] R. Bartels, S. Krishnamurthy, and C. Weniger, "Strong support for the millisecond pulsar origin of the Galactic center GeV excess," *Phys. Rev. Lett.* **116** no. 5, (2016) 051102, arXiv:1506.05104 [astro-ph.HE].

[177] E. Carlson, T. Linden, and S. Profumo, "Improved Cosmic-Ray Injection Models and the Galactic Center Gamma-Ray Excess," *Phys. Rev.* **D94** no. 6, (2016) 063504, arXiv:1603.06584 [astro-ph.HE].

[178] R. Bartels, E. Storm, C. Weniger, and F. Calore, "The Fermi-LAT GeV excess as a tracer of stellar mass in the Galactic bulge," *Nat. Astron.* **2** no. 10, (2018) 819–828, arXiv:1711.04778 [astro-ph.HE].

[179] **H.E.S.S.** Collaboration, H. Abdallah *et al.*, "Search for dark matter annihilations towards the inner Galactic halo from 10 years of observations with H.E.S.S," *Phys. Rev. Lett.* **117** no. 11, (2016) 111301, arXiv:1607.08142 [astro-ph.HE].

[180] **HAWC** Collaboration, A. U. Abeysekara *et al.*, "A Search for Dark Matter in the Galactic Halo with HAWC," *JCAP* **1802** no. 02, (2018) 049, arXiv:1710.10288 [astro-ph.HE].

[181] L. Pieri, J. Lavalle, G. Bertone, and E. Branchini, "Implications of High-Resolution Simulations on Indirect Dark Matter Searches," *Phys. Rev.* **D83** (2011) 023518, arXiv:0908.0195 [astro-ph.HE].

[182] M. Kuhlen, J. Guedes, A. Pillepich, P. Madau, and L. Mayer, "An Off-center Density Peak in the Milky Way's Dark Matter Halo?," *Astrophys. J.* **765** (2013) 10, arXiv:1208.4844 [astro-ph.GA].

[183] **HESS** Collaboration, H. Abdallah *et al.*, "Search for γ-Ray Line Signals from Dark Matter Annihilations in the Inner Galactic Halo from 10 Years of Observations with H.E.S.S.," *Phys. Rev. Lett.* **120** no. 20, (2018) 201101, arXiv:1805.05741 [astro-ph.HE].

[184] **H.E.S.S.** Collaboration, A. Abramowski *et al.*, "Constraints on an Annihilation Signal from a Core of Constant Dark Matter Density around the Milky Way Center with H.E.S.S.," *Phys. Rev. Lett.* **114** no. 8, (2015) 081301, arXiv:1502.03244 [astro-ph.HE].

[185] A. Tasitsiomi, J. M. Siegal-Gaskins, and A. V. Olinto, "Gamma-ray and synchrotron emission from neutralino annihilation in the Large Magellanic Cloud," *Astropart. Phys.* **21** (2004) 637–650, arXiv:astro-ph/0307375 [astro-ph].

[186] M. R. Buckley, E. Charles, J. M. Gaskins, A. M. Brooks, A. Drlica-Wagner, P. Martin, and G. Zhao, "Search for Gamma-ray Emission from Dark Matter Annihilation in the Large Magellanic Cloud with the Fermi Large Area Telescope," *Phys. Rev.* **D91** no. 10, (2015) 102001, arXiv:1502.01020 [astro-ph.HE].

[187] **H.E.S.S.** Collaboration, A. Abramowski *et al.*, "The exceptionally powerful TeV gamma-ray emitters in the Large Magellanic Cloud," *Science* **347** no. 6220, (2015) 406–412, arXiv:1501.06578 [astro-ph.HE].

[188] M. Mateo, "Dwarf galaxies of the Local Group," *Ann. Rev. Astron. Astrophys.* **36** (1998) 435–506, arXiv:astro-ph/9810070 [astro-ph].

[189] L. E. Strigari, S. M. Koushiappas, J. S. Bullock, M. Kaplinghat, J. D. Simon, M. Geha, and B. Willman, "The Most Dark Matter Dominated Galaxies: Predicted Gamma-ray Signals from the Faintest Milky Way Dwarfs," *Astrophys. J.* **678** (2008) 614, arXiv:0709.1510 [astro-ph].

[190] G. Battaglia, A. Helmi, and M. Breddels, "Internal kinematics and dynamical models of dwarf spheroidal galaxies around the Milky Way," *New Astron. Rev.* **57** (2013) 52–79, arXiv:1305.5965 [astro-ph.CO].

[191] A. Geringer-Sameth, S. M. Koushiappas, and M. Walker, "Dwarf galaxy annihilation and decay emission profiles for dark matter experiments," *Astrophys. J.* **801** no. 2, (2015) 74, arXiv:1408.0002 [astro-ph.CO].

[192] A. B. Pace and L. E. Strigari, "Scaling Relations for Dark Matter Annihilation and Decay Profiles in Dwarf Spheroidal Galaxies," arXiv:1802.06811 [astro-ph.GA].

[193] **HAWC** Collaboration, A. Albert *et al.*, "Dark Matter Limits From Dwarf Spheroidal Galaxies with The HAWC Gamma-Ray Observatory," *Astrophys. J.* **853** no. 2, (2018) 154, arXiv:1706.01277 [astro-ph.HE].

[194] **Fermi-LAT, MAGIC** Collaboration, M. L. Ahnen *et al.*, "Limits to Dark Matter Annihilation Cross-Section from a Combined Analysis of MAGIC and Fermi-LAT Observations of Dwarf Satellite Galaxies," *JCAP* **1602** no. 02, (2016) 039, arXiv:1601.06590 [astro-ph.HE].

[195] **VERITAS** Collaboration, S. Archambault *et al.*, "Dark Matter Constraints from a Joint Analysis of Dwarf Spheroidal Galaxy Observations with VERITAS," *Phys. Rev.* **D95** no. 8, (2017) 082001, arXiv:1703.04937 [astro-ph.HE].

[196] **DES, Fermi-LAT** Collaboration, A. Drlica-Wagner *et al.*, "Search for Gamma-Ray Emission from DES Dwarf Spheroidal Galaxy Candidates with Fermi-LAT Data," *Astrophys. J.* **809** no. 1, (2015) L4, arXiv:1503.02632 [astro-ph.HE].

[197] **MAGIC** Collaboration, M. L. Ahnen *et al.*, "Indirect dark matter searches in the dwarf satellite galaxy Ursa Major II with the MAGIC Telescopes," *JCAP* **1803** no. 03, (2018) 009, arXiv:1712.03095 [astro-ph.HE].

[198] J. Aleksi ć *et al.*, "Optimized dark matter searches in deep observations of Segue 1 with MAGIC," *JCAP* **1402** (2014) 008, arXiv:1312.1535 [hep-ph].

[199] **MAGIC** Collaboration, J. Aleksic *et al.*, "Searches for Dark Matter annihilation signatures in the Segue 1 satellite galaxy with the MAGIC-I telescope," *JCAP* **1106** (2011) 035, arXiv:1103.0477 [astro-ph.HE].

[200] **MAGIC** Collaboration, E. Aliu *et al.*, "Upper limits on the VHE gamma-ray emission from the Willman 1 satellite galaxy with the MAGIC Telescope," *Astrophys. J.* **697** (2009) 1299–1304, arXiv:0810.3561 [astro-ph].

[201] **MAGIC** Collaboration, J. Albert *et al.*, "Upper limit for gamma-ray emission above 140-GeV from the dwarf spheroidal galaxy Draco," *Astrophys. J.* **679** (2008) 428–431, arXiv:0711.2574 [astro-ph].

[202] **HAWC** Collaboration, S. H. Cadena, R. Alfaro, A. Sandoval, E. Belmont, H. Le ó n, V. Gammaldi, E. Karukes, and P. Salucci, "Searching for TeV DM evidence from Dwarf Irregular Galaxies with the HAWC Observatory," *PoS* **ICRC2017** (2018) 897, arXiv:1708.04642 [astro-ph.HE].

[203] **HAWC** Collaboration, A. U. Abeysekara *et al.*, "Searching for Dark Matter Sub-structure with HAWC," arXiv:1811.11732 [astro-ph.HE].

[204] H. Yuksel, S. Horiuchi, J. F. Beacom, and S. Ando, "Neutrino Constraints on the Dark Matter Total Annihilation Cross Section," *Phys. Rev.* **D76** (2007) 123506, arXiv:0707.0196 [astro-ph].

[205] G. Bertone, E. Nezri, J. Orloff, and J. Silk, "Neutrinos from dark matter annihilations at the Galactic Center," *Phys. Rev.* **D70** (2004) 063503, arXiv:astro-ph/0403322 [astro-ph].

[206] **BAIKAL** Collaboration, A. D. Avrorin *et al.*, "A search for neutrino signal from dark matter annihilation in the center of the Milky Way with Baikal NT200," *Astropart. Phys.* **81** (2016) 12–20, arXiv:1512.01198 [astro-ph.HE].

[207] **IceCube** Collaboration, M. G. Aartsen *et al.*, "Search for Dark Matter Annihilation in the Galactic Center with IceCube-79," *Eur. Phys. J.* **C75** no. 10, (2015) 492, arXiv:1505.07259 [astro-ph.HE].

[208] **IceCube** Collaboration, M. G. Aartsen *et al.*, "All-flavour Search for Neutrinos from Dark Matter Annihilations in the Milky Way with IceCube/DeepCore," *Eur. Phys. J.* **C76** no. 10, (2016) 531, arXiv:1606.00209 [astro-ph.HE].

[209] A. Albert *et al.*, "Results from the search for dark matter in the Milky Way with 9 years of data of the ANTARES neutrino telescope," *Phys. Lett.* **B769** (2017) 249–254, arXiv:1612.04595 [astro-ph.HE].

[210] M. Cirelli, R. Franceschini, and A. Strumia, "Minimal Dark Matter predictions for galactic positrons, anti-protons, photons," *Nucl. Phys.* **B800** (2008) 204–220, arXiv:0802.3378 [hep-ph].

[211] D. Maurin, F. Donato, R. Taillet, and P. Salati, "Cosmic rays below z=30 in a diffusion model: new constraints on propagation parameters," *Astrophys. J.* **555** (2001) 585–596, arXiv:astro-ph/0101231 [astro-ph].

[212] H.-B. Jin, Y.-L. Wu, and Y.-F. Zhou, "Cosmic ray propagation and dark matter in light of the latest AMS-02 data," *JCAP* **1509** no. 09, (2015) 049, arXiv:1410.0171 [hep-ph].

[213] T. Delahaye, R. Lineros, F. Donato, N. Fornengo, and P. Salati, "Positrons from dark matter annihilation in the galactic halo: Theoretical uncertainties," *Phys. Rev.* **D77** (2008) 063527, arXiv:0712.2312 [astro-ph].

[214] R. Trotta, G. Johannesson, I. V. Moskalenko, T. A. Porter, R. R. de Austri, and A. W. Strong, "Constraints on cosmic-ray propagation models from a global Bayesian analysis," *Astrophys. J.* **729** (2011) 106, arXiv:1011.0037 [astro-ph.HE].

[215] R. Cowsik and T. Madziwa-Nussinov, "Spectral Intensities of Antiprotons and the Nested Leaky-box Model for Cosmic Rays in the Galaxy," *Astrophys. J.* **827** no. 2, (2016) 119.

[216] M. Korsmeier and A. Cuoco, "Galactic cosmic-ray propagation in the light of AMS-02: Analysis of protons, helium, and antiprotons," *Phys. Rev.* **D94** no. 12, (2016) 123019, arXiv:1607.06093 [astro-ph.HE].

[217] M.-Y. Cui, X. Pan, Q. Yuan, Y.-Z. Fan, and H.-S. Zong, "Revisit of cosmic ray antiprotons from dark matter annihilation with updated constraints on the background model from AMS-02 and collider data," *JCAP* **1806** no. 06, (2018) 024, arXiv:1803.02163 [astro-ph.HE].

[218] A. E. Vladimirov, S. W. Digel, G. Johannesson, P. F. Michelson, I. V. Moskalenko, P. L. Nolan, E. Orlando, T. A. Porter, and A. W. Strong, "GALPROP WebRun: an internet-based service for calculating galactic cosmic ray propagation and associated photon emissions," *Comput. Phys. Commun.* **182** (2011) 1156–1161, arXiv:1008.3642 [astro-ph.HE].

[219] P. Brun, "Indirect Searches for Dark Matter with AMS-02," *Eur. Phys. J.* **C56** (2008) 27–31, arXiv:0710.2458 [astro-ph].

[220] M. Cirelli, M. Kadastik, M. Raidal, and A. Strumia, "Model-independent implications of the e+-, anti-proton cosmic ray spectra on properties of Dark Matter," *Nucl. Phys.* **B813** (2009) 1–21, arXiv:0809.2409 [hep-ph]. [Addendum: Nucl. Phys.B873,530(2013)].

[221] J. Kopp, "Constraints on dark matter annihilation from AMS-02 results," *Phys. Rev.* **D88** (2013) 076013, arXiv:1304.1184 [hep-ph].

[222] L. Bergstrom, T. Bringmann, I. Cholis, D. Hooper, and C. Weniger, "New limits on dark matter annihilation from AMS cosmic ray positron data," *Phys. Rev. Lett.* **111** (2013) 171101, arXiv:1306.3983 [astro-ph.HE].

[223] M. Di Mauro, F. Donato, N. Fornengo, and A. Vittino, "Dark matter vs. astrophysics in the interpretation of AMS-02 electron and positron data," *JCAP* **1605** no. 05, (2016) 031, arXiv:1507.07001 [astro-ph.HE].

[224] A. Cuoco, M. Kr ä mer, and M. Korsmeier, "Novel Dark Matter Constraints from Antiprotons in Light of AMS-02," *Phys. Rev. Lett.* **118** no. 19, (2017) 191102, arXiv:1610.03071 [astro-ph.HE].

[225] A. Cuoco, J. Heisig, M. Korsmeier, and M. Kr ä mer, "Constraining heavy dark matter with cosmic-ray antiprotons," *JCAP* **1804** no. 04, (2018) 004, arXiv:1711.05274 [hep-ph].

[226] H. M. K. K. Hiroshima, N., "Dependence of the accessible dark matter annihilation cross-section on the density profiles of dwarf spheroidal galaxies with Cherenkov Telescope Array,".

[227] **CTA Consortium** Collaboration, B. S. Acharya *et al.*, "Introducing the CTA concept," *Astropart. Phys.* **43** (2013) 3–18.

[228] **CTA Consortium** Collaboration, M. Actis *et al.*, "Design concepts for the Cherenkov Telescope Array CTA: An advanced facility for ground-based high-energy gamma-ray astronomy," *Exper. Astron.* **32** (2011) 193–316, arXiv:1008.3703 [astro-ph.IM].

[229] T. Hassan *et al.*, "Monte Carlo Performance Studies for the Site Selection of the Cherenkov Telescope Array," *Astropart. Phys.* **93** (2017) 76–85, arXiv:1705.01790 [astro-ph.IM].

[230] **Cherenkov Telescope Array Consortium** Collaboration, B. S. Acharya *et al.*, "Science with the Cherenkov Telescope Array," arXiv:1709.07997 [astro-ph.IM].

[231] "CTA's expected baseline performance." https://www.cta-observatory.org/science/cta-performance/.

[232] **CTA Consortium** Collaboration, K. Bernl ö hr *et al.*, "Monte Carlo design studies for the Cherenkov Telescope Array," *Astropart. Phys.* **43** (2013) 171–188, arXiv:1210.3503 [astro-ph.IM].

[233] T. P. Li and Y. Q. Ma, "Analysis methods for results in gamma-ray astronomy," *Astrophys. J.* **272** (1983) 317–324.

[234] **MAGIC** Collaboration, J. Albert *et al.*, "Unfolding of differential energy spectra in the MAGIC experiment," *Nucl. Instrum. Meth.* **A583** (2007) 494–506, arXiv:0707.2453 [astro-ph].

[235] **Fermi-LAT** Collaboration, W. B. Atwood *et al.*, "The Large Area Telescope on the Fermi Gamma-ray Space Telescope Mission," *Astrophys. J.* **697** (2009) 1071–1102, arXiv:0902.1089 [astro-ph.IM].

[236] **MAGIC** Collaboration, J. Aleksi ć *et al.*, "The major upgrade of the MAGIC telescopes, Part II: A performance study using observations of the Crab Nebula," *Astropart. Phys.* **72** (2016) 76–94, arXiv:1409.5594 [astro-ph.IM].

[237] G. Lake, "Detectability of gamma-rays from clumps of dark matter," *Nature* **346** (1990) 39–40.

[238] N. W. Evans, F. Ferrer, and S. Sarkar, "A 'Baedecker' for the dark matter annihilation signal," *Phys. Rev.* **D69** (2004) 123501, arXiv:astro-ph/0311145 [astro-ph].

[239] N. F. Martin *et al.*, "Hydra II: a faint and compact Milky Way dwarf galaxy found in the Survey of the Magellanic Stellar History," *Astrophys. J.* **804** no. 1, (2015) L5, arXiv:1503.06216 [astro-ph.GA].

[240] D. Kim and H. Jerjen, "Horologium II: a Second Ultra-faint Milky Way Satellite in the Horologium Constellation," *Astrophys. J.* **808** (2015) L39, arXiv:1505.04948 [astro-ph.GA].

[241] B. P. M. Laevens *et al.*, "A New Faint Milky Way Satellite Discovered in the Pan-STARRS1 3 π Survey," *Astrophys. J.* **802** (2015) L18, arXiv:1503.05554 [astro-ph.GA].

[242] B. P. M. Laevens *et al.*, "Sagittarius II, Draco II and Laevens 3: Three new Milky way Satellites Discovered in the Pan-starrs 1 3 *pi* Survey," *Astrophys. J.* **813** no. 1, (2015) 44, arXiv:1507.07564 [astro-ph.GA].

[243] **DES** Collaboration, E. Luque *et al.*, "Digging Deeper into the Southern Skies: A Compact Milky-Way Companion Discovered in First-Year Dark Energy Survey Data," *Mon. Not. Roy. Astron. Soc.* **458** no. 1, (2016) 603–612, arXiv:1508.02381 [astro-ph.GA].

[244] S. E. Koposov *et al.*, "Kinematics and chemistry of recently discovered Reticulum 2 and Horologium 1 dwarf galaxies," *Astrophys. J.* **811** no. 1, (2015) 62, arXiv:1504.07916 [astro-ph.GA].

[245] **DES** Collaboration, K. Bechtol *et al.*, "Eight New Milky Way Companions Discovered in First-Year Dark Energy Survey Data," *Astrophys. J.* **807** no. 1, (2015) 50, arXiv:1503.02584 [astro-ph.GA].

[246] A. W. McConnachie, "The observed properties of dwarf galaxies in and around the Local Group," *Astron. J.* **144** (2012) 4, arXiv:1204.1562 [astro-ph.CO].

[247] Gaia Collaboration, "Gaia Data Release 2. Kinematics of globular clusters and dwarf galaxies around the Milky Way," *"Astronomy & Astrophysics* (2018) .

[248] J. D. Simon, "Gaia Proper Motions and Orbits of the Ultra-faint Milky Way Satellites," *"Astrophys. J."* (2018) .

[249] L. E. Strigari, S. M. Koushiappas, J. S. Bullock, and M. Kaplinghat, "Precise constraints on the dark matter content of Milky Way dwarf galaxies for gamma-ray experiments," *Phys. Rev.* **D75** (2007) 083526, arXiv:astro-ph/0611925 [astro-ph].

[250] A. Charbonnier *et al.*, "Dark matter profiles and annihilation in dwarf spheroidal galaxies: prospectives for present and future gamma-ray observatories - I. The classical dSphs," *Mon. Not. Roy. Astron. Soc.* **418** (2011) 1526–1556, arXiv:1104.0412 [astro-ph.HE].

[251] K. Hayashi, K. Ichikawa, S. Matsumoto, M. Ibe, M. N. Ishigaki, and H. Sugai, "Dark matter annihilation and decay from non-spherical dark halos in galactic dwarf satellites," *Mon. Not. Roy. Astron. Soc.* **461** no. 3, (2016) 2914–2928, arXiv:1603.08046 [astro-ph.GA].

[252] M. Irwin and D. Hatzidimitriou, "Structural parameters for the Galactic dwarf spheroidals," *Mon. Not. Roy. Astron. Soc.* **277** (1995) 1354–1378.

[253] A. Geringer-Sameth, M. G. Walker, S. M. Koushiappas, S. E. Koposov, V. Belokurov, G. Torrealba, and N. W. Evans, "Indication of Gamma-ray Emission from the Newly Discovered Dwarf Galaxy Reticulum II," *Phys. Rev. Lett.* **115** no. 8, (2015) 081101, arXiv:1503.02320 [astro-ph.HE].

[254] **Fermi-LAT** Collaboration, A. A. Abdo *et al.*, "Observations of Milky Way Dwarf Spheroidal galaxies with the Fermi-LAT detector and constraints on Dark Matter models," *Astrophys. J.* **712** (2010) 147–158, arXiv:1001.4531 [astro-ph.CO].

[255] **Fermi-LAT** Collaboration, M. Ackermann *et al.*, "Constraining Dark Matter Models from a Combined Analysis of Milky Way Satellites with the Fermi Large Area Telescope," *Phys. Rev. Lett.* **107** (2011) 241302, arXiv:1108.3546 [astro-ph.HE].

[256] **Fermi-LAT** Collaboration, M. Ackermann *et al.*, "Dark matter constraints from observations of 25 Milky Way satellite galaxies with the Fermi Large Area Telescope," *Phys. Rev.* **D89** (2014) 042001, arXiv:1310.0828 [astro-ph.HE].

[257] **Fermi-LAT** Collaboration, M. Ackermann *et al.*, "Searching for Dark Matter Annihilation from Milky Way Dwarf Spheroidal Galaxies with Six Years of Fermi Large Area Telescope Data," *Phys. Rev. Lett.* **115** no. 23, (2015) 231301, arXiv:1503.02641 [astro-ph.HE].

[258] **MAGIC** Collaboration, M. Doro, "A review of the past and present MAGIC dark matter search program and a glimpse at the future," in *25th European Cosmic Ray Symposium (ECRS 2016) Turin, Italy, September 04-09, 2016*. 2017. arXiv:1701.05702 [astro-ph.HE]. https://inspirehep.net/record/1510040/files/arXiv:1701.05702.pdf.

[259] **H.E.S.S.** Collaboration, F. Aharonian, "Observations of the Sagittarius Dwarf galaxy by the H.E.S.S. experiment and search for a Dark Matter signal," *Astropart. Phys.* **29** (2008) 55–62, arXiv:0711.2369 [astro-ph]. [Erratum: Astropart. Phys.33,274(2010)].

[260] **H.E.S.S.** Collaboration, F. Aharonian, "A search for a dark matter annihilation signal towards the Canis Major overdensity with H.E.S.S," *Astrophys. J.* **691** (2009) 175–181, arXiv:0809.3894 [astro-ph].

[261] **H.E.S.S.** Collaboration, A. Abramowski *et al.*, "H.E.S.S. constraints on Dark Matter annihilations towards the Sculptor and Carina Dwarf Galaxies," *Astropart. Phys.* **34** (2011) 608–616, arXiv:1012.5602 [astro-ph.HE].

[262] **H.E.S.S.** Collaboration, A. Abramowski *et al.*, "Search for dark matter annihilation signatures in H.E.S.S. observations of Dwarf Spheroidal Galaxies," *Phys. Rev.* **D90** (2014) 112012, arXiv:1410.2589 [astro-ph.HE].

[263] **VERITAS** Collaboration, V. A. Acciari *et al.*, "VERITAS Search for VHE Gamma-ray Emission from Dwarf Spheroidal Galaxies," *Astrophys. J.* **720** (2010) 1174–1180, arXiv:1006.5955 [astro-ph.CO].

[264] **VERITAS** Collaboration, E. Aliu *et al.*, "VERITAS Deep Observations of the Dwarf Spheroidal Galaxy Segue 1," *Phys. Rev.* **D85** (2012) 062001, arXiv:1202.2144 [astro-ph.HE]. [Erratum: Phys. Rev.D91,no.12,129903(2015)].

[265] R. Essig, N. Sehgal, L. E. Strigari, M. Geha, and J. D. Simon, "Indirect Dark Matter Detection Limits from the Ultra-Faint Milky Way Satellite Segue 1," *Phys. Rev.* **D82** (2010) 123503, arXiv:1007.4199 [astro-ph.CO].

[266] V. Bonnivard *et al.*, "Dark matter annihilation and decay in dwarf spheroidal galaxies: The classical and ultrafaint dSphs," *Mon. Not. Roy. Astron. Soc.* **453** no. 1, (2015) 849–867, arXiv:1504.02048 [astro-ph.HE].

[267] L. Ambrogi, S. Celli, and F. Aharonian, "On the potential of Cherenkov Telescope Arrays and KM3 Neutrino Telescopes for the detection of extended sources," *Astropart. Phys.* **100** (2018) 69–79, arXiv:1803.03565 [astro-ph.HE].

[268] **HESS** Collaboration, H. Abdalla *et al.*, "Searches for gamma-ray lines and 'pure WIMP' spectra from Dark Matter annihilations in dwarf galaxies with H.E.S.S," *JCAP* **1811** no. 11, (2018) 037, arXiv:1810.00995 [astro-ph.HE].

[269] E. L. Lokas, "Dark matter distribution in dwarf spheroidal galaxies," *Mon. Not. Roy. Astron. Soc.* **333** (2002) 697, arXiv:astro-ph/0112023 [astro-ph].

[270] E. L. Lokas, G. A. Mamon, and F. Prada, "Dark matter distribution in the Draco dwarf from velocity moments," *Mon. Not. Roy. Astron. Soc.* **363** (2005) 918, arXiv:astro-ph/0411694 [astro-ph].

[271] S. Mashchenko, A. Sills, and H. M. P. Couchman, "Constraining global properties of the draco dwarf spheroidal galaxy," *Astrophys. J.* **640** (2006) 252–269, arXiv:astro-ph/0511567 [astro-ph].

[272] M. A. Sanchez-Conde, F. Prada, E. L. Lokas, M. E. Gomez, R. Wojtak, and M. Moles, "Dark Matter annihilation in Draco: New considerations of the expected gamma flux," *Phys. Rev.* **D76** (2007) 123509, arXiv:astro-ph/0701426 [astro-ph].

[273] J. Knödlseder *et al.*, "GammaLib and ctools: A software framework for the analysis of astronomical gamma-ray data," *Astron. Astrophys.* **593** (2016) A1, arXiv:1606.00393 [astro-ph.IM].

[274] **CTA Consortium** Collaboration, P. Cumani, T. Hassan, L. Arrabito, K. Bernlöhr, J. Bregeon, G. Maier, and A. Moralejo, "Baseline telescope layouts of the Cherenkov Telescope Array," *PoS* **ICRC2017** (2018) 811, arXiv:1709.00206 [astro-ph.IM].

[275] D. Heck, J. Knapp, J. N. Capdevielle, G. Schatz, and T. Thouw, "CORSIKA: A Monte Carlo code to simulate extensive air showers,".

[276] A. D. Panov *et al.*, "Elemental Energy Spectra of Cosmic Rays from the Data of the ATIC-2 Experiment," *Bull. Russ. Acad. Sci. Phys.* **71** (2007) 494–497, arXiv:astro-ph/0612377 [astro-ph]. [Izv. Ross. Akad. Nauk Ser. Fiz.71,512(2007)].

[277] **H.E.S.S.** Collaboration, F. Aharonian *et al.*, "Probing the ATIC peak in the cosmic-ray electron spectrum with H.E.S.S," *Astron. Astrophys.* **508** (2009) 561, arXiv:0905.0105 [astro-ph.HE].

[278] **Fermi-LAT** Collaboration, A. A. Abdo *et al.*, "Measurement of the Cosmic Ray e+ plus e- spectrum from 20 GeV to 1 TeV with the Fermi Large Area Telescope," *Phys. Rev. Lett.* **102** (2009) 181101, arXiv:0905.0025 [astro-ph.HE].

[279] L. Hernquist, "An Analytical Model for Spherical Galaxies and Bulges," *Astrophys. J.* **356** (1990) 359.

[280] H. Zhao, "Analytical models for galactic nuclei," *Mon. Not. Roy. Astron. Soc.* **278** (1996) 488–496, arXiv:astro-ph/9509122 [astro-ph].

[281] J. F. Navarro, C. S. Frenk, and S. D. M. White, "A Universal density profile from hierarchical clustering," *Astrophys. J.* **490** (1997) 493–508, arXiv:astro-ph/9611107 [astro-ph].

[282] A. Burkert, "The Structure of dark matter halos in dwarf galaxies," *IAU Symp.* **171** (1996) 175, arXiv:astro-ph/9504041 [astro-ph]. [Astrophys. J.447,L25(1995)].

[283] V. Bonnivard, C. Combet, D. Maurin, and M. G. Walker, "Spherical Jeans analysis for dark matter indirect detection in dwarf spheroidal galaxies - Impact of physical parameters and triaxiality," *Mon. Not. Roy. Astron. Soc.* **446** (2015) 3002–3021, arXiv:1407.7822 [astro-ph.HE].

[284] V. Bonnivard, M. Hütten, E. Nezri, A. Charbonnier, C. Combet, and D. Maurin, "CLUMPY : Jeans analysis, γ-ray and ν fluxes from dark matter (sub-)structures," *Comput. Phys. Commun.* **200** (2016) 336–349, arXiv:1506.07628 [astro-ph.CO].

[285] M. Hütten, C. Combet, G. Maier, and D. Maurin, "Dark matter substructure modelling and sensitivity of the Cherenkov Telescope Array to Galactic dark halos," *JCAP* **1609** no. 09, (2016) 047, arXiv:1606.04898 [astro-ph.HE].

[286] K. Griest and M. Kamionkowski, "Unitarity Limits on the Mass and Radius of Dark Matter Particles," *Phys. Rev. Lett.* **64** (1990) 615.

[287] T. Sjöstrand, S. Ask, J. R. Christiansen, R. Corke, N. Desai, P. Ilten, S. Mrenna, S. Prestel, C. O. Rasmussen, and P. Z. Skands, "An Introduction to PYTHIA 8.2," *Comput. Phys. Commun.* **191** (2015) 159–177, arXiv:1410.3012 [hep-ph].

[288] T. Sjostrand, S. Mrenna, and P. Z. Skands, "PYTHIA 6.4 Physics and Manual," *JHEP* **05** (2006) 026, arXiv:hep-ph/0603175 [hep-ph].

[289] T. Sjostrand, S. Mrenna, and P. Z. Skands, "A Brief Introduction to PYTHIA 8.1," *Comput. Phys. Commun.* **178** (2008) 852–867, arXiv:0710.3820 [hep-ph].

[290] A. V. Belikov and D. Hooper, "The Contribution Of Inverse Compton Scattering To The Diffuse Extragalactic Gamma-Ray Background From Annihilating Dark Matter," *Phys. Rev.* **D81** (2010) 043505, arXiv:0906.2251 [astro-ph.CO].

[291] M. Cirelli and P. Panci, "Inverse Compton constraints on the Dark Matter e+e- excesses," *Nucl. Phys.* **B821** (2009) 399–416, arXiv:0904.3830 [astro-ph.CO].

[292] S. Profumo and T. E. Jeltema, "Extragalactic Inverse Compton Light from Dark Matter Annihilation and the Pamela Positron Excess," *JCAP* **0907** (2009) 020, arXiv:0906.0001 [astro-ph.CO].

[293] C. Blanco, J. P. Harding, and D. Hooper, "Novel Gamma-Ray Signatures of PeV-Scale Dark Matter," *JCAP* **1804** no. 04, (2018) 060, arXiv:1712.02805 [hep-ph].

[294] R. Bartels, D. Gaggero, and C. Weniger, "Prospects for indirect dark matter searches with MeV photons," *JCAP* **1705** no. 05, (2017) 001, arXiv:1703.02546 [astro-ph.HE].

[295] N. Hiroshima, S. Ando, and T. Ishiyama, "Modeling evolution of dark matter substructure and annihilation boost," *Phys. Rev.* **D97** no. 12, (2018) 123002, arXiv:1803.07691 [astro-ph.CO].

[296] N. Yoshida, V. Springel, S. D. M. White, and G. Tormen, "Weakly self-interacting dark matter and the structure of dark halos," *Astrophys. J.* **544** (2000) L87–L90, arXiv:astro-ph/0006134 [astro-ph].

[297] F. C. van den Bosch, G. Tormen, and C. Giocoli, "The Mass function and average mass loss rate of dark matter subhaloes," *Mon. Not. Roy. Astron. Soc.* **359** (2005) 1029–1040, arXiv:astro-ph/0409201 [astro-ph].

[298] C. Giocoli, L. Pieri, and G. Tormen, "Analytical Approach to Subhaloes Population in Dark Matter Haloes," *Mon. Not. Roy. Astron. Soc.* **387** (2008) 689–697, arXiv:0712.1476 [astro-ph].

[299] F. Jiang and F. C. van den Bosch, "Statistics of dark matter substructure - I. Model and universal fitting functions," *Mon. Not. Roy. Astron. Soc.* **458** no. 3, (2016) 2848–2869, arXiv:1403.6827 [astro-ph.CO].

[300] J. Penarrubia and A. J. Benson, "Effects of dynamical evolution on the distribution of substructures," *Mon. Not. Roy. Astron. Soc.* **364** (2005) 977–989, arXiv:astro-ph/0412370 [astro-ph].

[301] L. Gao, S. D. M. White, A. Jenkins, F. Stoehr, and V. Springel, "The Subhalo populations of lambda-CDM dark halos," *Mon. Not. Roy. Astron. Soc.* **355** (2004) 819, arXiv:astro-ph/0404589 [astro-ph].

[302] J. Diemand, M. Kuhlen, and P. Madau, "Formation and evolution of galaxy dark matter halos and their substructure," *Astrophys. J.* **667** (2007) 859–877, arXiv:astro-ph/0703337 [astro-ph].

[303] C. Giocoli, G. Tormen, and F. C. v. d. Bosch, "The Population of Dark Matter Subhaloes: Mass Functions and Average Mass Loss Rates," *Mon. Not. Roy. Astron. Soc.* **386** (2008) 2135–2144, arXiv:0712.1563 [astro-ph].

[304] K. Dolag, S. Borgani, G. Murante, and V. Springel, "Substructures in hydrodynamical cluster simulations," *Mon. Not. Roy. Astron. Soc.* **399** (2009) 497, arXiv:0808.3401 [astro-ph].

[305] V. Springel, J. Wang, M. Vogelsberger, A. Ludlow, A. Jenkins, A. Helmi, J. F. Navarro, C. S. Frenk, and S. D. M. White, "The Aquarius Project: the subhalos of galactic halos," *Mon. Not. Roy. Astron. Soc.* **391** (2008) 1685–1711, arXiv:0809.0898 [astro-ph].

[306] F. C. van den Bosch, G. Ogiya, O. Hahn, and A. Burkert, "Disruption of Dark Matter Substructure: Fact or Fiction?," *Mon. Not. Roy. Astron. Soc.* **474** no. 3, (2018) 3043–3066, arXiv:1711.05276 [astro-ph.GA].

[307] J. Diemand, M. Kuhlen, and P. Madau, "Dark matter substructure and gamma-ray annihilation in the Milky Way halo," *Astrophys. J.* **657** (2007) 262–270, arXiv:astro-ph/0611370 [astro-ph].

[308] L. Pieri, G. Bertone, and E. Branchini, "Dark Matter Annihilation in Substructures Revised," *Mon. Not. Roy. Astron. Soc.* **384** (2008) 1627, arXiv:0706.2101 [astro-ph].

[309] T. E. Jeltema and S. Profumo, "Searching for Dark Matter with X-ray Observations of Local Dwarf Galaxies," *Astrophys. J.* **686** (2008) 1045, arXiv:0805.1054 [astro-ph].

[310] T. Ishiyama, "Hierarchical Formation of Dark Matter Halos and the Free Streaming Scale," *Astrophys. J.* **788** (2014) 27, arXiv:1404.1650 [astro-ph.CO].

[311] R. Bartels and S. Ando, "Boosting the annihilation boost: Tidal effects on dark matter subhalos and consistent luminosity modeling," *Phys. Rev.* **D92** no. 12, (2015) 123508, arXiv:1507.08656 [astro-ph.CO].

[312] M. A. Sánchez-Conde and F. Prada, "The flattening of the concentration - mass relation towards low halo masses and its implications for the annihilation signal boost," *Mon. Not. Roy. Astron. Soc.* **442** no. 3, (2014) 2271–2277, arXiv:1312.1729 [astro-ph.CO].

[313] C. A. Correa, J. S. B. Wyithe, J. Schaye, and A. R. Duffy, "The accretion history of dark matter haloes - I. The physical origin of the universal function," *Mon. Not. Roy. Astron. Soc.* **450** no. 2, (2015) 1514–1520, arXiv:1409.5228 [astro-ph.GA].

[314] X. Yang, H. J. Mo, Y. Zhang, and F. C. v. d. Bosch, "An analytical model for the accretion of dark matter subhalos," *Astrophys. J.* **741** (2011) 13, arXiv:1104.1757 [astro-ph.CO].

[315] G. L. Bryan and M. L. Norman, "Statistical properties of x-ray clusters: Analytic and numerical comparisons," *Astrophys. J.* **495** (1998) 80, arXiv:astro-ph/9710107 [astro-ph].

[316] C. A. Correa, J. S. B. Wyithe, J. Schaye, and A. R. Duffy, "The accretion history of dark matter haloes - III. A physical model for the concentration - mass relation," *Mon. Not. Roy. Astron. Soc.* **452** no. 2, (2015) 1217–1232, arXiv:1502.00391 [astro-ph.CO].

[317] W. Hu and A. V. Kravtsov, "Sample variance considerations for cluster surveys," *Astrophys. J.* **584** (2003) 702–715, arXiv:astro-ph/0203169 [astro-ph].

[318] T. Ishiyama, J. Makino, S. Portegies Zwart, D. Groen, K. Nitadori, S. Rieder, C. de Laat, S. McMillan, K. Hiraki, and S. Harfst, "The Cosmogrid Simulation: Statistical Properties of Small Dark Matter Halos," *Astrophys. J.* **767** (2013) 146, arXiv:1101.2020 [astro-ph.CO].

[319] J. Penarrubia, A. J. Benson, M. G. Walker, G. Gilmore, A. McConnachie, and L. Mayer, "The impact of dark matter cusps and cores on the satellite galaxy population around spiral galaxies," *Mon. Not. Roy. Astron. Soc.* **406** (2010) 1290, arXiv:1002.3376 [astro-ph.GA].

[320] E. Hayashi, J. F. Navarro, J. E. Taylor, J. Stadel, and T. R. Quinn, "The Structural evolution of substructure," *Astrophys. J.* **584** (2003) 541–558, arXiv:astro-ph/0203004 [astro-ph].

[321] A. D. Ludlow, S. Bose, R. E. Angulo, L. Wang, W. A. Hellwing, J. F. Navarro, S. Cole, and C. S. Frenk, "The mass - concentration - redshift relation of cold and warm dark matter haloes," *Mon. Not. Roy. Astron. Soc.* **460** no. 2, (2016) 1214–1232, arXiv:1601.02624 [astro-ph.CO].

[322] **Planck** Collaboration, P. A. R. Ade *et al.*, "Planck 2013 results. XVI. Cosmological parameters," *Astron. Astrophys.* **571** (2014) A16, arXiv:1303.5076 [astro-ph.CO].

[323] A. R. Wetzel, "On the Orbits of Infalling Satellite Halos," *Mon. Not. Roy. Astron. Soc.* **412** (2011) 49, arXiv:1001.4792 [astro-ph.CO].

[324] T. Ishiyama, M. Enoki, M. A. R. Kobayashi, R. Makiya, M. Nagashima, and T. Oogi, "The ν^2GC simulations: Quantifying the dark side of the universe in the Planck cosmology," *Publ. Astron. Soc. Jap.* **67** no. 4, (2015) 61, arXiv:1412.2860 [astro-ph.CO].

[325] T. Ishiyama *et al.*, "*in preparation*,".

[326] T. Ishiyama, T. Fukushige, and J. Makino, "GreeM : Massively Parallel TreePM Code for Large Cosmological N-body Simulations," *Publ. Astron. Soc. Jap.* **61** (2009) 1319–1330, arXiv:0910.0121 [astro-ph.IM].

[327] T. Ishiyama, K. Nitadori, and J. Makino, "4.45 Pflops Astrophysical N-Body Simulation on K computer – The Gravitational Trillion-Body Problem," arXiv:1211.4406 [astro-ph.CO].

[328] P. S. Behroozi, R. H. Wechsler, and H.-Y. Wu, "The Rockstar Phase-Space Temporal Halo Finder and the Velocity Offsets of Cluster Cores," *Astrophys. J.* **762** (2013) 109, arXiv:1110.4372 [astro-ph.CO].

[329] P. S. Behroozi, R. H. Wechsler, H.-Y. Wu, M. T. Busha, A. A. Klypin, and J. R. Primack, "Gravitationally Consistent Halo Catalogs and Merger Trees for Precision Cosmology," *Astrophys. J.* **763** (2013) 18, arXiv:1110.4370 [astro-ph.CO].

[330] R. Makiya, M. Enoki, T. Ishiyama, M. A. R. Kobayashi, M. Nagashima, T. Okamoto, K. Okoshi, T. Oogi, and H. Shirakata, "The New Numerical Galaxy Catalog (ν^2GC): An updated semi-analytic model of galaxy and active galactic nucleus formation with large cosmological N-body simulations," *Publ. Astron. Soc. Jap.* **68** no. 2, (2016) 25, arXiv:1508.07215 [astro-ph.GA].

[331] J. Diemand, M. Kuhlen, and P. Madau, "Early supersymmetric cold dark matter substructure," *Astrophys. J.* **649** (2006) 1–13, arXiv:astro-ph/0603250 [astro-ph].

[332] C. Giocoli, G. Tormen, R. K. Sheth, and F. C. van den Bosch, "The Substructure Hierarchy in Dark Matter Haloes," *Mon. Not. Roy. Astron. Soc.* **404** (2010) 502–517, arXiv:0911.0436 [astro-ph.CO].

[333] M. Stref and J. Lavalle, "Modeling dark matter subhalos in a constrained galaxy: Global mass and boosted annihilation profiles," *Phys. Rev.* **D95** no. 6, (2017) 063003, arXiv:1610.02233 [astro-ph.CO].

[334] C. Okoli and N. Afshordi, "Concentration, Ellipsoidal Collapse, and the Densest Dark Matter haloes," *Mon. Not. Roy. Astron. Soc.* **456** no. 3, (2016) 3068–3078, arXiv:1510.03868 [astro-ph.CO].

[335] M. Gosenca, J. Adamek, C. T. Byrnes, and S. Hotchkiss, "3D simulations with boosted primordial power spectra and ultracompact minihalos," *Phys. Rev.* **D96** no. 12, (2017) 123519, arXiv:1710.02055 [astro-ph.CO].

[336] T. Nakama, T. Suyama, K. Kohri, and N. Hiroshima, "Constraints on small-scale primordial power by annihilation signals from extragalactic dark matter minihalos," *Phys. Rev.* **D97** no. 2, (2018) 023539, arXiv:1712.08820 [astro-ph.CO].

[337] M. S. Delos, A. L. Erickcek, A. P. Bailey, and M. A. Alvarez, "Are ultracompact minihalos really ultracompact?," *Phys. Rev.* **D97** no. 4, (2018) 041303, arXiv:1712.05421 [astro-ph.CO].

[338] M. Kamionkowski and S. M. Koushiappas, "Galactic substructure and direct detection of dark matter," *Phys. Rev.* **D77** (2008) 103509, arXiv:0801.3269 [astro-ph].

[339] M. Kamionkowski, S. M. Koushiappas, and M. Kuhlen, "Galactic Substructure and Dark Matter Annihilation in the Milky Way Halo," *Phys. Rev.* **D81** (2010) 043532, arXiv:1001.3144 [astro-ph.GA].

[340] I. Cholis and D. Hooper, "Constraining the origin of the rising cosmic ray positron fraction with the boron-to-carbon ratio," *Phys. Rev.* **D89** no. 4, (2014) 043013, arXiv:1312.2952 [astro-ph.HE].

[341] M. Di Mauro and F. Donato, "Composition of the Fermi-LAT isotropic gamma-ray background intensity: Emission from extragalactic point sources and dark matter annihilations," *Phys. Rev.* **D91** no. 12, (2015) 123001, arXiv:1501.05316 [astro-ph.HE].

[342] S. Ando, "Gamma-ray background anisotropy from galactic dark matter substructure," *Phys. Rev.* **D80** (2009) 023520, arXiv:0903.4685 [astro-ph.CO].

[343] S. Ando and E. Komatsu, "Anisotropy of the cosmic gamma-ray background from dark matter annihilation," *Phys. Rev.* **D73** (2006) 023521, arXiv:astro-ph/0512217 [astro-ph].

[344] S. Ando, E. Komatsu, T. Narumoto, and T. Totani, "Dark matter annihilation or unresolved astrophysical sources? Anisotropy probe of the origin of cosmic gamma-ray background," *Phys. Rev.* **D75** (2007) 063519, arXiv:astro-ph/0612467 [astro-ph].

[345] S. Ando, M. Fornasa, N. Fornengo, M. Regis, and H.-S. Zechlin, "Astrophysical interpretation of the anisotropies in the unresolved gamma-ray background," *Phys. Rev.* **D95** no. 12, (2017) 123006, arXiv:1701.06988 [astro-ph.HE].

[346] S. Ando, "Power spectrum tomography of dark matter annihilation with local galaxy distribution," *JCAP* **1410** no. 10, (2014) 061, arXiv:1407.8502 [astro-ph.CO].

[347] N. Fornengo and M. Regis, "Particle dark matter searches in the anisotropic sky," *Front. Physics* **2** (2014) 6, arXiv:1312.4835 [astro-ph.CO].

[348] M. Lisanti, S. Mishra-Sharma, N. L. Rodd, and B. R. Safdi, "A Search for Dark Matter Annihilation in Galaxy Groups," arXiv:1708.09385 [astro-ph.CO].

[349] 松原隆彦, 現代宇宙論ー時空と物質の共進化. 東京大学出版会, 2010.

[350] E. W. Kolb and M. S. Turner, "The Early Universe," *Nature* **294** (1981) 521.

[351] J. Abdallah *et al.*, "Simplified Models for Dark Matter Searches at the LHC," *Phys. Dark Univ.* **9-10** (2015) 8–23, arXiv:1506.03116 [hep-ph].

[352] A. Nelson, L. M. Carpenter, R. Cotta, A. Johnstone, and D. Whiteson, "Confronting the Fermi Line with LHC data: an Effective Theory of Dark Matter Interaction with Photons," *Phys. Rev.* **D89** no. 5, (2014) 056011, arXiv:1307.5064 [hep-ph].

[353] **CMS** Collaboration, A. M. Sirunyan *et al.*, "Search for new physics in final states with a single photon and missing transverse momentum in proton-proton collisions at $\sqrt{s}$ = 13 TeV," *Submitted to: JHEP* (2018) , arXiv:1810.00196 [hep-ex].

[354] **ATLAS** Collaboration, M. Aaboud *et al.*, "Search for dark matter at $\sqrt{s}$ = 13 TeV in final states containing an energetic photon and large missing transverse momentum with the ATLAS detector," *Eur. Phys. J.* **C77** no. 6, (2017) 393, arXiv:1704.03848 [hep-ex].

[355] G. Busoni *et al.*, "Recommendations on presenting LHC searches for missing transverse energy signals using simplified *s*-channel models of dark matter," arXiv:1603.04156 [hep-ex].

[356] G. B. Gelmini, "The Hunt for Dark Matter," in *Proceedings, Theoretical Advanced Study Institute in Elementary Particle Physics: Journeys Through the Precision Frontier: Amplitudes for Colliders (TASI 2014): Boulder, Colorado, June 2-27, 2014*, pp. 559–616. 2015. arXiv:1502.01320 [hep-ph].

[357] **ATLAS** Collaboration, M. Aaboud *et al.*, "Search for chargino-neutralino production using recursive jigsaw reconstruction in final states with two or three charged leptons in proton-proton collisions at $\sqrt{s}$ = 13 TeV with the ATLAS detector," *Phys. Rev.* **D98** no. 9, (2018) 092012, arXiv:1806.02293 [hep-ex].

[358] **CMS** Collaboration, A. M. Sirunyan *et al.*, "Combined search for electroweak production of charginos and neutralinos in proton-proton collisions at $\sqrt{s}$ = 13 TeV," *JHEP* **03** (2018) 160, arXiv:1801.03957 [hep-ex].

[359] **GAMBIT** Collaboration, P. Athron *et al.*, "Combined collider constraints on neutralinos and charginos," arXiv:1809.02097 [hep-ph].

[360] J. D. Lewin and P. F. Smith, "Review of mathematics, numerical factors, and corrections for dark matter experiments based on elastic nuclear recoil," *Astropart. Phys.* **6** (1996) 87–112.

[361] **PandaX-II** Collaboration, X. Cui *et al.*, "Dark Matter Results From 54-Ton-Day Exposure of PandaX-II Experiment," *Phys. Rev. Lett.* **119** no. 18, (2017) 181302, arXiv:1708.06917 [astro-ph.CO].

[362] **XMASS** Collaboration, M. Kobayashi *et al.*, "Search for sub-GeV dark matter by annual modulation using XMASS-I detector," arXiv:1808.06177 [astro-ph.CO].

[363] **XMASS** Collaboration, T. Suzuki *et al.*, "Search for WIMP-^{129}Xe inelastic scattering with particle identification in XMASS-I," arXiv:1809.05358 [astro-ph.CO].

[364] **DarkSide** Collaboration, P. Agnes *et al.*, "Low-Mass Dark Matter Search with the DarkSide-50 Experiment," *Phys. Rev. Lett.* **121** no. 8, (2018) 081307, arXiv:1802.06994 [astro-ph.HE].

[365] **SuperCDMS** Collaboration, R. Agnese *et al.*, "New Results from the Search for Low-Mass Weakly Interacting Massive Particles with the CDMS Low Ionization Threshold Experiment," *Phys. Rev. Lett.* **116** no. 7, (2016) 071301, arXiv:1509.02448 [astro-ph.CO].

[366] **CRESST** Collaboration, F. Petricca *et al.*, "First results on low-mass dark matter from the CRESST-III experiment," in *15th International Conference on Topics in Astroparticle and Underground Physics (TAUP 2017) Sudbury, Ontario, Canada, July 24-28, 2017*. 2017. arXiv:1711.07692 [astro-ph.CO].

[367] **DAMA** Collaboration, R. Bernabei *et al.*, "First results from DAMA/LIBRA and the combined results with DAMA/NaI," *Eur. Phys. J.* **C56** (2008) 333–355, arXiv:0804.2741 [astro-ph].

[368] **DAMA, LIBRA** Collaboration, R. Bernabei *et al.*, "New results from DAMA/LIBRA," *Eur. Phys. J.* **C67** (2010) 39–49, arXiv:1002.1028 [astro-ph.GA].

[369] R. Bernabei *et al.*, "First Model Independent Results from DAMA/LIBRA - Phase2," *Universe* **4** no. 11, (2018) 116, arXiv:1805.10486 [hep-ex].

[370] J. Amare *et al.*, "The ANAIS-112 experiment at the Canfranc Underground Laboratory," in *15th International Conference on Topics in Astroparticle and Underground Physics (TAUP 2017) Sudbury, Ontario, Canada, July 24-28, 2017*. 2017. arXiv:1710.03837 [physics.ins-det].

[371] P. Adhikari *et al.*, "Understanding internal backgrounds in NaI(Tl) crystals toward a 200 kg array for the KIMS-NaI experiment," *Eur. Phys. J.* **C76** no. 4, (2016) 185, arXiv:1510.04519 [physics.ins-det].

[372] G. Adhikari *et al.*, "Initial Performance of the COSINE-100 Experiment," *Eur. Phys. J.* **C78** no. 2, (2018) 107, arXiv:1710.05299 [physics.ins-det].

[373] **COSINE-100** Collaboration, C. Ha *et al.*, "The First Direct Search for Inelastic Boosted Dark Matter with COSINE-100," arXiv:1811.09344 [astro-ph.IM].

[374] **DM-Ice** Collaboration, E. Barbosa de Souza *et al.*, "First search for a dark matter annual modulation signal with NaI(Tl) in the Southern Hemisphere by DM-Ice17," *Phys. Rev.* **D95** no. 3, (2017) 032006, arXiv:1602.05939 [physics.ins-det].

[375] **SABRE** Collaboration, C. Tomei, "SABRE: Dark matter annual modulation detection in the northern and southern hemispheres," *Nucl. Instrum. Meth.* **A845** (2017) 418–420.

[376] **LUX** Collaboration, D. S. Akerib *et al.*, "Results on the Spin-Dependent Scattering of Weakly Interacting Massive Particles on Nucleons from the Run 3 Data of the LUX Experiment," *Phys. Rev. Lett.* **116** no. 16, (2016) 161302, arXiv:1602.03489 [hep-ex].

[377] R. Essig, M. Sholapurkar, and T.-T. Yu, "Solar Neutrinos as a Signal and Background in Direct-Detection Experiments Searching for Sub-GeV Dark Matter With Electron Recoils," *Phys. Rev.* **D97** no. 9, (2018) 095029, arXiv:1801.10159 [hep-ph].

[378] **SENSEI** Collaboration, M. Crisler, R. Essig, J. Estrada, G. Fernandez, J. Tiffenberg, M. Sofo haro, T. Volansky, and T.-T. Yu, "SENSEI: First Direct-Detection Constraints on sub-GeV Dark Matter from a Surface Run," *Phys. Rev. Lett.* **121** no. 6, (2018) 061803, arXiv:1804.00088 [hep-ex].

[379] C. V. Cappiello, K. C. Y. Ng, and J. F. Beacom, "Reverse Direct Detection: Cosmic Ray Scattering With Light Dark Matter," arXiv:1810.07705 [hep-ph].

[380] T. Bringmann and M. Pospelov, "Novel direct detection constraints on light dark matter," arXiv:1810.10543 [hep-ph].

[381] Y. Ema, F. Sala, and R. Sato, "Light Dark Matter at Neutrino Experiments," arXiv:1811.00520 [hep-ph].

[382] A. K. Drukier, S. Baum, K. Freese, M. G ó rski, and P. Stengel, "Paleo-detectors: Searching for Dark Matter with Ancient Minerals," arXiv:1811.06844 [astro-ph.CO].

[383] T. D. P. Edwards, B. J. Kavanagh, C. Weniger, S. Baum, A. K. Drukier, K. Freese, M. G ó rski, and P. Stengel, "Digging for Dark Matter: Spectral Analysis and Discovery Potential of Paleo-Detectors," arXiv:1811.10549 [hep-ph].

[384] 井上一, 小山勝二, 高橋忠幸, 水本好彦, 宇宙の観測 *III* ー高エネルギー天文学, シリーズ現代の天文学 第 *17* 巻. 日本評論社, 2008.

[385] R. Engel, D. Heck, and T. Pierog, "Extensive air showers and hadronic interactions at high energy," *Ann. Rev. Nucl. Part. Sci.* **61** (2011) 467–489.

[386] R. L ó pez-Coto, *Very-high-energy gamma-ray observations of pulsar wind nebulae and cataclysmic variable stars with MAGIC and development of trigger systems for IACTs*. PhD thesis, Barcelona, Autonoma U., 2015. https://magic.mpp.mpg.de/backend/publication/show/332.

[387] **Particle Data Group** Collaboration, M. Tanabashi *et al.*, "Review of Particle Physics," *Phys. Rev.* **D98** no. 3, (2018) 030001.

[388] F. Aharonian, W. Hofmann, A. Konopelko, and H. V ö lk, "The potential of ground based arrays of imaging atmospheric cherenkov telescopes. i. determination of shower parameters," *Astroparticle Physics* **6** no. 3, (1997) 343 – 368. http://www.sciencedirect.com/science/article/pii/S0927650596000692.

[389] K. Bernlohr, "Simulation of Imaging Atmospheric Cherenkov Telescopes with CORSIKA and sim_telarray," *Astropart. Phys.* **30** (2008) 149–158, arXiv:0808.2253 [astro-ph].

[390] J. D. Jackson, *Classical Electrodynamics, 3rd Edition*. July, 1998.

[391] W. B. Atwood *et al.*, "Design and Initial Tests of the Tracker-Converter of the Gamma-ray Large Area Space Telescope," *Astropart. Phys.* **28** (2007) 422–434.

[392] V. Bonnivard, D. Maurin, and M. G. Walker, "Contamination of stellar-kinematic samples and uncertainty about dark matter annihilation profiles in ultrafaint dwarf galaxies: the example of Segue I," *Mon. Not. Roy. Astron. Soc.* **462** no. 1, (2016) 223–234, arXiv:1506.08209 [astro-ph.GA].

[393] M. G. Coleman, K. Jordi, H.-W. Rix, E. K. Grebel, and A. Koch, "A Wide-Field View of Leo II – A Structural Analysis Using the SDSS," *Astron. J.* **134** (2007) 1938–1951, arXiv:0708.1853 [astro-ph].

[394] V. Smolcic, D. Zucker, E. F. Bell, M. G. Coleman, H. W. Rix, E. Schinnerer, Z. Ivezic, and A. Kniazev, "Improved photometry of SDSS crowded field images: Structure and dark matter content in the dwarf spheroidal galaxy Leo I," *Astron. J.* **134** (2007) 1901–1915, arXiv:0708.2661 [astro-ph].

[395] J. D. Simon and M. Geha, "The Kinematics of the Ultra-Faint Milky Way Satellites: Solving the Missing Satellite Problem," *Astrophys. J.* **670** (2007) 313–331, arXiv:0706.0516 [astro-ph].

[396] N. F. Martin, J. T. A. de Jong, and H.-W. Rix, "A comprehensive Maximum Likelihood analysis of the structural properties of faint Milky Way satellites," *Astrophys. J.* **684** (2008) 1075–1092, arXiv:0805.2945 [astro-ph].

[397] N. F. Bate, B. McMonigal, G. F. Lewis, M. J. Irwin, E. Gonzalez-Solares, T. Shanks, and N. Metcalfe, "The shell game: a panoramic view of Fornax," *Mon. Not. Roy. Astron. Soc.* (2015) .

[398] **DES** Collaboration, A. Drlica-Wagner *et al.*, "Eight Ultra-faint Galaxy Candidates Discovered in Year Two of the Dark Energy Survey," *Astrophys. J.* **813** no. 2, (2015) 109, arXiv:1508.03622 [astro-ph.GA].

[399] R. A. Ibata, G. F. Gilmore, and M. J. Irwin, "Sagittarius: The Nearest dwarf galaxy," *Mon. Not. Roy. Astron. Soc.* **277** (1995) 781, arXiv:astro-ph/9506071 [astro-ph].

[400] S. R. Majewski, M. F. Skrutskie, M. D. Weinberg, and J. C. Ostheimer, "A 2mass all-sky view of the Sagittarius dwarf galaxy: I. Morphology of the Sagittarius core and tidal arms," *Astrophys. J.* **599** (2003) 1082–1115, arXiv:astro-ph/0304198 [astro-ph].

[401] A. Koch, M. I. Wilkinson, J. T. Kleyna, M. Irwin, D. B. Zucker, V. Belokurov, G. F. Gilmore, M. Fellhauer, and N. W. Evans, "A spectroscopic confirmation of the Bootes II dwarf spheroidal," *Astrophys. J.* **690** (2009) 453–462, arXiv:0809.0700 [astro-ph].

[402] F. Fraternali, E. Tolstoy, M. Irwin, and A. Cole, "Life at the Periphery of the Local Group: the kinematics of the Tucana Dwarf Galaxy," *Astron. Astrophys.* **499** (2009) 121, arXiv:0903.4635 [astro-ph.CO].

[403] B. P. M. Laevens *et al.*, "A new distant Milky Way globular cluster in the Pan-STARRS1 3π survey," *Astrophys. J.* **786** (2014) L3, arXiv:1403.6593 [astro-ph.GA].

[404] E. N. Kirby, J. D. Simon, and J. G. Cohen, "Spectroscopic Confirmation of the Dwarf Galaxies Hydra II and Pisces II and the Globular Cluster Laevens 1," *Astrophys. J.* **810** no. 1, (2015) 56, arXiv:1506.01021 [astro-ph.GA].

[405] **DES** Collaboration, J. D. Simon *et al.*, "Stellar Kinematics and Metallicities in the Ultra-Faint Dwarf Galaxy Reticulum II," *Astrophys. J.* **808** no. 1, (2015) 95, arXiv:1504.02889 [astro-ph.GA].

[406] D. Kim, H. Jerjen, M. Geha, A. Chiti, A. P. Milone, D. Mackey, G. Da Costa, A. Frebel, and B. Conn, "Portrait of a Dark Horse: a Photometric and Spectroscopic Study of the Ultra-faint Milky way Satellite Pegasus iii," *Astrophys. J.* **833** no. 1, (2016) 16, arXiv:1608.04934 [astro-ph.GA].

[407] M. G. Walker *et al.*, "Magellan/M2FS spectroscopy of Tucana 2 and Grus 1," *Astrophys. J.* **819** no. 1, (2016) 53, arXiv:1511.06296 [astro-ph.GA].

[408] G. Torrealba *et al.*, "At the survey limits: discovery of the Aquarius 2 dwarf galaxy in the VST ATLAS and the SDSS data," *Mon. Not. Roy. Astron. Soc.* .

[409] G. Torrealba *et al.*, "Discovery of two neighbouring satellites in the Carina constellation with MagLiteS," *Mon. Not. Roy. Astron. Soc.* **475** no. 4, (2018) 5085–5097, arXiv:1801.07279 [astro-ph.GA].

[410] A. B. Pace and T. S. Li, "Proper motions of Milky Way Ultra-Faint satellites with *Gaia* DR2 × DES DR1,".

[411] J. S. Kalirai, R. L. Beaton, M. C. Geha, K. M. Gilbert, P. Guhathakurta, E. N. Kirby, S. R. Majewski, J. C. Ostheimer, R. J. Patterson, and J. Wolf, "The SPLASH Survey: Internal Kinematics, Chemical Abundances, and Masses of the Andromeda I, II, III, VII, X, and XIV dSphs," *Astrophys. J.* **711** (2010) 671–692, arXiv:0911.1998 [astro-ph.GA].

[412] M. L. M. Collins *et al.*, "A Keck/DEIMOS spectroscopic survey of the faint M31 satellites And IX, And XI, And XII, and And XIII," *Mon. Not. Roy. Astron. Soc.* **407** (2010) 2411, arXiv:0911.1365 [astro-ph.CO].

[413] E. F. Bell, C. T. Slater, and N. F. Martin, "Andromeda XXIX: A New Dwarf Spheroidal Galaxy 200kpc from Andromeda," *Astrophys. J.* **742** (2011) L15, arXiv:1110.5906 [astro-ph.CO].

[414] N. F. Martin *et al.*, "Lacerta I and Cassiopeia III: Two luminous and distant Andromeda satellite dwarf galaxies found in the 3π Pan-STARRS1 survey," *Astrophys. J.* **772** (2013) 15, arXiv:1305.5301 [astro-ph.CO].

[415] M. L. M. Collins *et al.*, "A kinematic study of the Andromeda dwarf spheroidal system," *Astrophys. J.* **768** (2013) 172, arXiv:1302.6590 [astro-ph.CO].

[416] N. F. Martin *et al.*, "The PAndAS View of the Andromeda Satellite System. II. Detailed Properties of 23 M31 Dwarf Spheroidal Galaxies," *Astrophys. J.* (2016) .

[417] J. T. A. de Jong *et al.*, "The structural properties and star formation history of Leo T from deep LBT photometry," *Astrophys. J.* **680** (2008) 1112, arXiv:0801.4027 [astro-ph].

[418] **DES** Collaboration, T. S. Li *et al.*, "Farthest Neighbor: The Distant Milky Way Satellite Eridanus II," *Astrophys. J.* **838** no. 1, (2017) 8, arXiv:1611.05052 [astro-ph.GA].